

Sivert Olsvik Sæther

Hydrodynamic Investigation of Central Hauling Pools for Longline Vessels

Master's thesis in Ship Design
Supervisor: Karl Henning Halse
June 2019

Sivert Olsvik Sæther

Hydrodynamic Investigation of Central Hauling Pools for Longline Vessels

Master's thesis in Ship Design
Supervisor: Karl Henning Halse
June 2019

Norwegian University of Science and Technology
Faculty of Engineering
Department of Ocean Operations and Civil Engineering



Norwegian University of
Science and Technology

Preface

This thesis is the final delivery of a master's degree in ship design at the Norwegian University of Science and Technology, department of Ocean Operations and Civil Engineering in Ålesund. The work load is equivalent to 30 ECTS. With its approval comes the title Master of Science in Ship Design.

The intention of this thesis is to find the ideal position and shape of the moonpool applicable to longline fishing vessels, known as the central hauling pool. It is written in cooperation with Marin Teknikk AS, where the idea behind the problem was brought up by Richard K. Gjerde.

It is assumed that the reader has some prior knowledge to naval architecture.



Sivert Olsvik Sæther
Stud. Tech - Ship Design



Date: Thursday 6th June, 2019

Department: Department of Ocean Operations and Civil Engineering

Hydrodynamic Investigation of Central Hauling Pools for Longline Vessels

Background and motivation

A moonpool is an opening right through the bottom of the ship, allowing for equipment to be launched and retrieved at locations where the ship motions are at a lower magnitude. The moonpool was first applied to a longline vessel in 1995 and has since then proven its benefits. The main advantages are better working environment for the fishermen and reduced loss of fish during the hauling process compared to the traditional hauling process at the side of the vessel.

There has not been done much research and development of the longline moonpool since 1998 when Norsk Marinteknisk Forskningsinstitutt and Fiskerstrand Verft patented their idea. The patent has now expired, and the moonpool has now become an industry standard for the longline vessels. A large part of the longline fleet is now ready for renewal, and ship owners and designers have found room for improvements which this thesis is going to address.

Objectives

The objective of this thesis is to investigate and analyze two different hydrodynamic aspects of the moonpool applied to longline vessels.

1. Investigate what the ideal position of the moonpool with respect to vessel motion.
2. Investigate three different shapes of the moonpool: round, elliptical and rectangular, and determine which one results in more circulation of the water, to avoid an accumulation of dirty water.

Research Questions

The thesis is going to address the following research questions:

1. Based on vessel motion prediction, what is the best position of the moonpool?
2. Based on numerical flow simulations, what of the shapes mentioned above for the moonpool pipe is ideal with regards to avoidance of accumulation of dirty water?



Guidelines

The work scope may prove to be different than initially anticipated. Subject to approval from the supervisor, topics may be added or deleted from the list above or reduce in extent.

The thesis shall be written as a research report, following the template given in Inspira. During preparation of the text, the candidate should make efforts to create a well-arranged and well-written report. To ease the evaluation of the thesis, it is important to cross-reference text, tables and figures. For evaluation of the work a thorough discussion of results is needed. Discussion of research method, validation and generalization of results is also appreciated.

The thesis shall be submitted in electronic version according to standard procedures (.PDF or .ZIP files). Instructions are found on the NTNU website (Inspira) and on Blackboard. In addition to the specified tasks, an A3 poster should be prepared and delivered together with this proposal, and a conference paper will be handled at the end of the research.

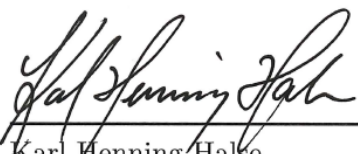
After finalizing and delivering the thesis, it must be sent a copy to the supervisor(s).

Deliveries:

- Presentation(6th June, 2019)
- Final Thesis(11th June, 2019)



Sivert Olsvik Sæther
Stud. Tech - Ship Design



Karl Henning Halse
Supervisor



Henry Peter Piehl
Co-Supervisor

Abstract

The central hauling pool has now become an industry standard for the longline fishing vessels. On the other hand, there has not been done much research on the purpose-built moonpool for longline fishing since the first vessel was launched in 1998. Ship owners and ship designers have now found room for improvements, which this thesis addresses.

Two different aspects of the moonpool for the longline vessel were investigated in this thesis. The first aspect looked at the longitudinal placement of the moonpool and rail-roll, to find the location where the rail-roll has the lowest vertical acceleration to avoid tearing the fish of the hooks during hauling, and at the same time limiting the strain on the longline. This aspect was investigated with the use of a numerical vessel response estimation software, which utilized 2D strip theory.

The results show that the positioning of the rail-roll moonpool is especially sensitive for head seas wave conditions and that the ideal placement of the rail-roll is aft of the longitudinal center of buoyancy. There was however some limitations for the results obtained, and this is further elaborated within the body of this document.

The second aspect that was investigated in this thesis was the shape of the moonpool pipe. The first longline moonpools had an elliptical shape, but this shifted towards a circular shape to save space and that the maneuvering over the longline proved to be easier than first anticipated. Furthermore, some desired effects were at the same time lost in the transition, which was the ability to clean the water inside the moonpool at low speeds. The intention was to evaluate three different shapes to determine which form that was resulting in more circulation of the water to avoid an accumulation of the dirty water inside the moonpool.

Circular, elliptical and rectangular shaped moonpool pipes were subjects for investigation, and this was carried out using computational fluid dynamics simulations. A method with the use of passive scalar transport was developed to be able to differentiate between the different shapes by tracking the ability to clean the water in the moonpool. The results show that the elliptical and rectangular moonpool shapes provide a better behavior of cleaning out dirty water, but there was at the same time some shortcomings with the method developed.

Sammendrag

Tittel: Hydrodynamisk undersøkelse av dragerbrønn for linefartøy

Dragerbrønnen har nå blitt en industristandard for linefartøy, men der har ikke vært mye forskning og utvikling på dragerbrønnen siden det første fartøyet ble sjøsatt i 1998. Skipsredere og designere har nå funnet rom for forbedringer. Denne hovedoppgaven vil ta for seg to forskjellige aspekter ved dragerbrønnen.

Det første aspektet ser på langskips plasseringen av dragerbrønnen og linerullen, for å finne posisjonen hvor linerullen opplever minst vertikal akselerasjon. Denne posisjonen er ønsket for å minske tapet av fisk under haling og begrense strekket på lina. Dette var undersøkt ved hjelp av programvarer som numerisk estimer fartøysrespons, ved hjelp av 2D stripeteori.

Resultatene viser at posisjonen til linerullen og dragerbrønnen er spesielt sensitive i møtende sjø, og den ideal plasseringen av linerullen og dragerbrønnen er aktenfor fartøyets oppdriftssenter. Der var på den andre siden noen begrensingene med resultatene, og disse er videre utdypet i dokumentet.

Det andre aspektet ved oppgaven så på utformingen av dragerbrønn røret. De første linebåtene bygget med dragerbrønn hadde et elliptisk rør, men dette ble endret til et sirkulært rør for å spare plass og at manøvreringen over linen visste seg å være enklere enn først antatt. Men noen ønskede effekter vart samtidig tapt i overgangen, som var egenskapet til å skifte ut vannet inne i dragerbrønnen i lave hastigheter. Intensjonen var å undersøke forskjellige utforminger og fastslå hvilken utforming som ville bidra til mer sirkulasjon av vannet for å unngå en oppsamling av skitten vann inne i dragerbrønnen.

Sirkuler, elliptisk og rektangulær utformede dragerbrønn rør var undersøkt, ved hjelp av numerisk fluiddynamikk simuleringer. En metode for å undersøke hvilken form som bidro til mest utskifting av vann ble utviklet, ved hjelp av passiv skalar transport. Den elliptiske og rektangulære dragerbrønn røret visste potensiale, men der var på samme tid noen begrensinger ved den utvikla metoden.

Acknowledgment

I would like to use this opportunity to show my gratitude towards everyone which have contributed to not only this thesis but also my five years at the university. I would like to express my appreciation towards all the lecturers and fellow students for helping me develop solid knowledge and friendships.

A special thanks to my supervisor and co-supervisor, Karl Henning Halse and Henry Peter Piehl for guidance throughout the thesis, with both methodology and analysis of the results. And a thanks to Marin Teknikk with Richard K. Gjerde and Erling J. Rovde for providing me with an appealing problem, and input for the thesis.

At last but not least, I could have never done this without the support and encouragement from my family and friends. It is also worth mentioning my mom, Evy Olsvik(Figure 2.1 and 5.2), and my friend, Johan G. Helgesen(Figure 2.3), which have helped me make illustrations for the thesis. For this I'm grateful, thank you!

Contents

Preface	I
Master Agreement	III
Abstract	V
Sammendrag	VII
Acknowledgement	IX
List of Figures	XVI
List of Tables	XVII
Nomenclature	XIX
1 Introduction	1
1.1 Background	1
1.2 Motivation	1
1.3 Scope	2
1.4 Objective	2
1.5 Research questions	2
1.6 Report structure	3
2 Longline Fishing	5
2.1 What is longline fishing?	5
2.2 Moonpool	7
2.3 Dragerbrønn	9
3 Theory	11
3.1 Vessel response theory	11
3.1.1 Forces and moments	12
3.1.2 Motion	14
3.1.3 Potential theory	15
3.1.4 Moonpool effects	20
3.1.5 Short term statistics	21
3.2 Fluid flow theory	23

3.2.1	Computational fluid dynamics theory	23
3.2.2	Turbulence modeling	24
3.2.3	Finite volume method	24
3.2.4	Multi-phase flow	25
3.2.5	Boundary layer	25
3.2.6	Time step and inner iterations	27
3.2.7	Implicit unsteady	27
3.2.8	Boundary conditions and initial conditions	28
3.2.9	Mesh	29
3.2.10	Passive Scalar	30
4	Moonpool Position Study	31
4.1	Method	31
4.1.1	ShipX and VERES	32
4.2	Setup	32
4.2.1	Wave periods and headings	32
4.2.2	Vertical force estimator	32
4.2.3	Short term statistics	32
4.2.4	Vessel	33
4.2.5	Moonpool	33
4.2.6	Moonpool positions	34
4.3	Results	35
5	Moonpool Shape Study	41
5.1	Method	41
5.1.1	Star-CCM+	42
5.1.2	Computational setup	42
5.2	Full domain simulation	42
5.2.1	Domain	43
5.2.2	Boundaries	43
5.2.3	Mesh	44
5.2.4	Convergence study	45
5.2.5	Result	47
5.3	Limited domain simulation	48
5.3.1	Domain	48
5.3.2	Geometry	49
5.3.3	Boundaries	51
5.3.4	Mesh	51
5.3.5	Initial conditions and solver settings	53
5.3.6	Results	54
6	Discussion and Future Work	57
6.1	Discussion	57
6.1.1	Moonpool position study	57
6.1.2	Moonpool shape study	58
6.2	Future Work	61

7 Conclusive Summary	63
Bibliography	63
Appendices	66
A Moonpool position study results	67
B Volumetric refinements - Full domain	71
C Full domain results	75
D Volumetric refinements - Limited domain	77
E Limited domain results	81
F Passive scalar mass flux	85
G Moonpool shape study - Passive scalar results	87
H Moonpool shape study - Velocity vector field results	93

List of Figures

2.1	The principle of the longline fishing method(Evy Olsvik)	5
2.2	The principle of the Autoline system (Bjordal & Lokkeborg 1996)	6
2.3	The principle of the central hauling pool(Johan G. Helgesen)	8
2.4	Comparison of the loss of fish between hauling methods(Larsen 2010)	8
2.5	Longline hauling direction(Karlsen 1997)	10
3.1	2D strip theory principle(Journée & Massie 2002)	12
3.2	Superposition of wave excitation, added mass, dampening and restoring forces (Faltinsen 1990)	14
3.3	Rigid body motions and wave propagation(Faltinsen 1990)	14
3.4	2D fluid domain and control surface	20
3.5	Schematic side view of rectangular moonpool(Fathi 2018)	21
3.6	JONSWAP spectra for $\gamma = 1 - 7$ (Fathi & Hoff 2017)	22
3.7	Low y^+ wall approach (Star-CCM+ 2018)	26
3.8	High y^+ wall approach (Star-CCM+ 2018)	26
3.9	y^+ value regions (Star-CCM+ 2018)	26
3.10	Courant Friedrichs Lewy Condition principle	27
4.1	Longitudinal moonpool positions	34
4.2	Response at rail-roll on conventional vessel at LCB[g]	35
4.3	Response at rail-roll on vessel with moonpool at LCB[g]	36
4.4	Response at rail-roll on vessel with moonpool placed 5 m forward of LCB[g]	36
4.5	Response at rail-roll on vessel with moonpool placed 5 m aft of LCB[g]	37
4.6	Response at rail-roll for for all moonpool positions at $T_P = 10.0 s$	37
4.7	Response at rail-roll for moonpool positions at LCB and LCB $\pm 5.0 m$ in beam seas	38
4.8	Response at rail-roll for moonpool positions at LCB and LCB $\pm 5.0 m$ in head seas	38
4.9	Response at rail-roll for for moonpool positions aft of LCB in head seas	39
4.10	Comparison between conventional ship and ship with moonpool for positions aft of LCB	39
4.11	Longitudinal position comparisons at different peak periods	40
5.1	Moonpool shape study flowchart	41
5.2	Double body domain dimensions(Evy Olsvik)	43
5.3	Full domain mesh convergence study	46
5.4	Top view of full domain mesh with base cell size of 1.25 m	46
5.5	Side view of full domain mesh with base cell size of 1.25 m	47
5.6	Bottom view of hull with streamlines	47

5.7	Side view of hull with streamlines	47
5.8	Limited domain with rectangular moonpool	49
5.9	Moonpool side view and cross-sectional shapes	50
5.10	Limited domain mesh with base cell size of $0.75m$	53
5.11	Moonpool pipe refinement with base cell size of $0.75m$	53
5.12	Volume flow of dirty water($0.0 - 40.0 s$)	54
5.13	Volume flow of dirty water($39.0 - 40.0 s$)	54
5.14	Passive scalar field for circular shaped moonpool pipe, at time step $40.0 s$	55
5.15	Passive scalar field for elliptical shaped moonpool pipe, at time step $40.0 s$)	55
5.16	Passive scalar field for rectangular shaped moonpool pipe, at time step $40.0 s$	55
5.17	Passive scalar blend in moonpool pipe cross section, at time step $40.0 s$	56
6.1	Longitudinal position comparisons at different peak periods($H_s = 3.5 m$)	57
6.2	Volume flow of dirty water($30.0 - 40.0 s$)	59

List of Tables

3.1	Moonpool parameters in VERES	21
4.1	Hull dimensions of MT1114	33
4.2	Moonpool dimensions	34
5.1	Virtual client specifications	42
5.2	Full domain boundary condition specifications	44
5.3	Full domain base mesh settings	44
5.4	Full domain refinement zones	45
5.5	Full domain mesh convergence study	46
5.6	Limited domain boundary condition specifications	51
5.7	Full domain base mesh settings	51
5.8	Limited domain refinement zones	52

Nomenclature

The next list describes abbreviations, symbols and constants that will be used within the body of this document

Abbreviations

AP Aft perpendicular

CDF Computational fluid dynamics

CFL Courant–Friedrichs–Lewy condition

ITTC International Towing Tank Conference

LCB Longitudinal center of buoyancy

LCF Longitudinal center of flotation

NS Navier Stokes

NTNU Norwegian University of Science and Technology

RANS Reynolds Average Navier Stokes

VOF Volume of fluid

Physics Constants

g Gravitational Constant 9.81 m/s^2

Other Symbols

$\ddot{\eta}$ Acceleration

$\dot{\eta}$ Velocity

η Displacement

μ Dynamic viscosity

ω Wave frequency

Φ	Total velocity potential
ϕ	Velocity potential
ρ	Density
H_s	Significant wave height
R_e	Reynolds number
T	Wave period
T_p	Wave peak period
y^+	Dimensionless wall distance

Chapter 1

Introduction

1.1 Background

The traditional longline vessels have the hauling equipment on the starboard side of the vessel, but there has been a shift towards hauling through moonpools in the center of the vessels. The benefits of hauling through moonpools are claimed to be safety, operability, and less loss of fish in the hauling process. It is favorable to place the rail-roll and the moonpool at the position of the vessel where the motion is at the lowest magnitude. There has not been established such guidelines for the placement.

The moonpools constructed for longline hauling purposes generally have a circular moonpool pipe but have earlier had a more elliptical shape. The elliptical shape allowed for more circulation of the water inside the moonpool at low speeds but was not as space efficient as the circular. This circulation is preferred to avoid an accumulation of dirty water inside the moonpool, but is not achieved at low speeds with the circular shape.

1.2 Motivation

There has not been done much research and development of the longlining moonpool since 1998 when Norsk Marinteknisk Forskningsinstitutt and Fiskerstrand Verft patented their idea. The patent has now expired and a large part the longline fleet is ready for renewal. The central hauling pool has now become an industry standard for the longline vessels, and ship owners and designers have found room for improvements which this thesis is going to address.

It is commonly known that the world has a growing food demand due to population growth. More than 70% of the earth surface is covered by ocean, but we only harvest 10% of our food from the ocean according to National Geographic (2018). Some of the reasoning behind this is that not all fishing is profitable, but can be made profitable by increasing the efficiency, which the solving of these problems could contribute to.

There is also a personal aspect of the motivation behind the topic of this thesis. The author have more or less grown up on a longline vessel until his dad, and uncle sold the family business

back in 2007. This has led the author wanting to work with the design of fishing vessels , and he has a belief that fishing vessels can be one of the stronger segments in future for the North West region. Especially, in a less oil and gas oriented market.

1.3 Scope

The scope of this study was to investigate and analyze two different hydrodynamical aspects of the moonpool applied to large longline vessels. The first aspect was addressing the longitudinal position of the central hauling pool, carried out using vessel motion predictions software. The other aspect was the form of the moonpool pipe, and how different shapes could contribute to less accumulation of dirty water inside the moonpool. This was investigated with the use of computational fluid dynamics software.

These analyses was carried out on a hull geometry provided by Marin Teknisk AS(MT1114).

1.4 Objective

The objective of this thesis are based on the problems described earlier in this chapter, and two different aspects of the moonpool was investigated:

1. Investigate what the ideal position of the central hauling pool is with respect to vessel motion.
2. Investigate three different shapes of the moonpool pipe: circular, elliptical and rectangular, and determine which one results in more circulation of the water, to avoid an accumulation of dirty water inside the moonpool.

1.5 Research questions

The thesis addressed the following two research question(RQ):

RQ. 1 Based on vessel motion prediction, what is the best position of the moonpool with regards to vertical motion?

RQ. 2 Based on numerical flow simulations, what of the shapes mentioned above for the moonpool pipe is ideal with regards to avoidance of accumulation of dirty water?

These research questions was composed in cooperation between the author, the supervisors and the industrial partner involved. Each research question was treated separately, and was investigated with two different approaches.

1.6 Report structure

This thesis has the following framework:

Chapter 2 describes the principle of longline fishing and the history behind the fishing method. The idea and application of the moonpool is at the same time described, and relevant work to the central hauling pool is presented.

Chapter 3 outlines the theory applicable for both the moonpool position study and the moonpool shape study. This includes 2D strip theory, linear potential flow theory and viscous flow theory.

Chapter 4 presents the method and results related to the moonpool position study.

Chapter 5 presents the method and results related the moonpool shape study.

Chapter 6 discuss the findings in chapter 4 and 5, and presents recommendations for future research.

Chapter 7 summarizes the thesis, and concludes based on the available results from the previous chapters.

The appendices contains supplementary data and results which is not an essential for the thesis itself, but which may be helpful in providing a more comprehensive understanding of the results.

Chapter 2

Longline Fishing

2.1 What is longline fishing?

Longline fishing is defined as a passive fishing method, where the gear is stationary, and the fish is attracted to the gear. This principle is the same as with pots and traps. The longline consists of a mainline, where the baited hooks are attached by thin ropes called snoods. The longline is divided into skates, which often have as many as 1000 hooks, where the distance between each hook often is around 1.2-1.5 meters. Several skates can be coupled together to make a fleet, which can be up to 50 kilometers long (Bjordal & Lokkeborg 1996) and consist of up to 40.000 hooks. This is illustrated in Figure 2.1.

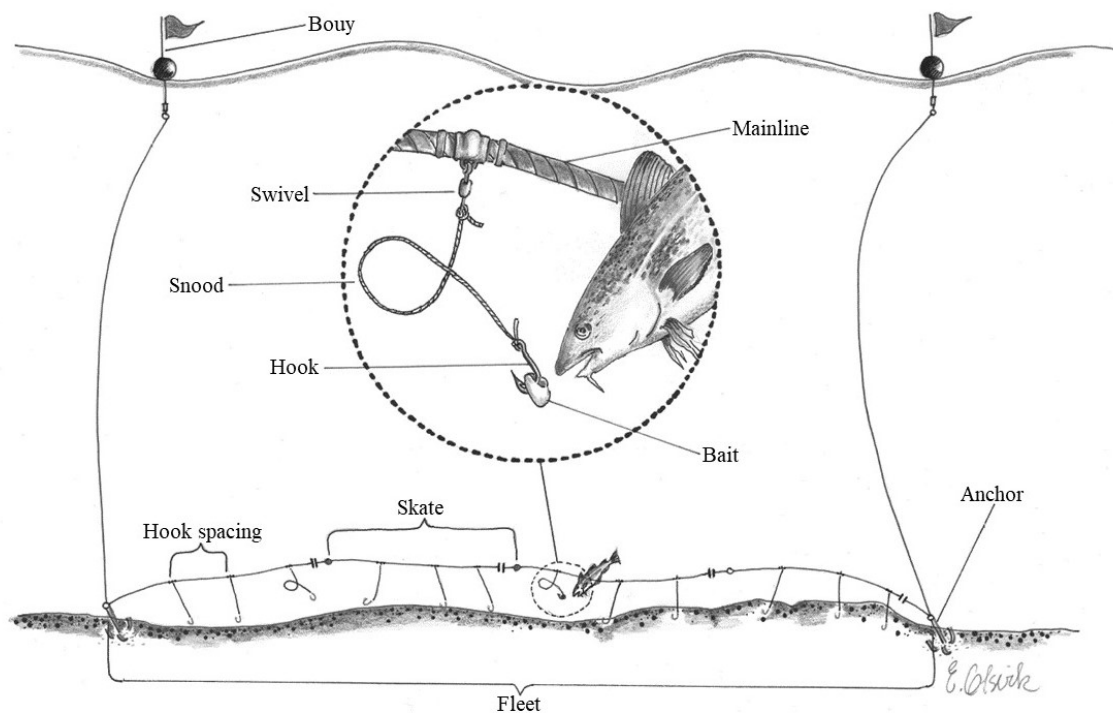


Figure 2.1: The principle of the longline fishing method (Evy Olsvik)

In Norway, longline fishing is mainly done on the sea bottom, called groundfishing. The depth for the water can be up to 1200 meters. The main fish types, in particular are cod and haddock, but halibut, catfish, common ling and cusk is also common to catch during groundfishing.

History

Fishing with the help of hooks with bait dates back to the stone age, but the large scale longlining dates back to the industrial revolution when mass production of hooks was made possible by machines (Karlsen 1997).

The modern form of fishing with longline as seen today started its evolution in the early 70s, where the so-called autoline was introduced by O. Mustad & Son Ltd in Gjøvik, Norway (Bjordal & Lokkeborg 1996), now called Mustad Autoline AS. The traditional longline fishing method was mechanically automated to increase efficiency and improve working conditions, and keeping up the high quality at the same time.

The invention of the autoline has made Mustad Autoline the world leading manufacturer of commercial longline technology. The following figure can explain the process on board the ship, where each component is allocated a number and explain in the description following on the following page.

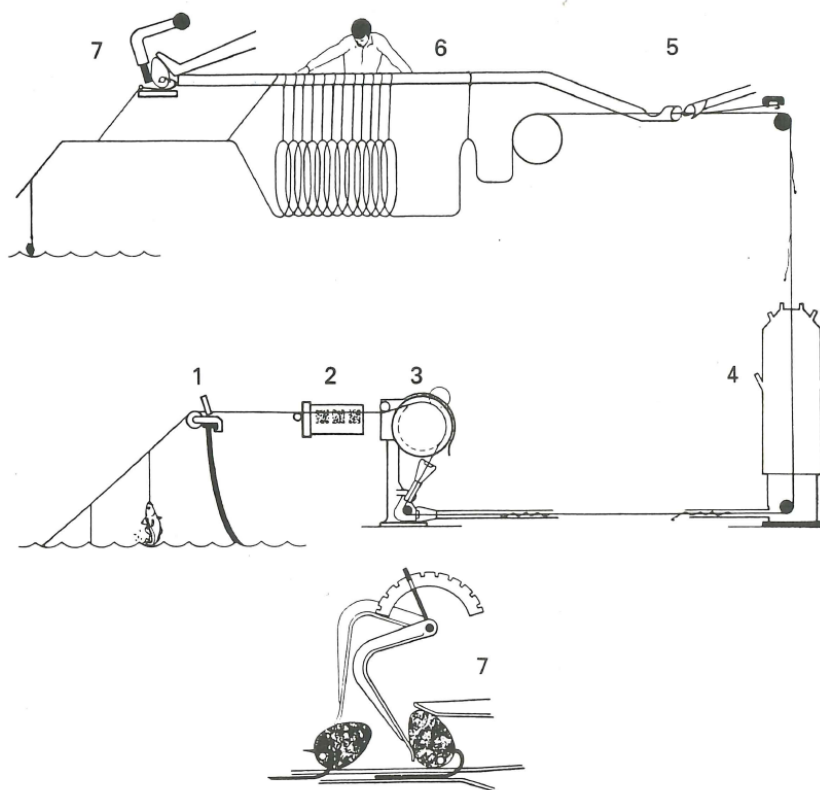


Figure 2.2: The principle of the Autoline system (Bjordal & Lokkeborg 1996)

1. Rail-roll, guides the longline over the rail of the ship.
2. De-hooker and hook cleaner, takes the fish and unused bait of the hook.
3. Line hauler, hauls the line from the seabed.
4. Twist remover, take out the twist in the line.
5. Hook separator, guides the hook into the storage rack.
6. Storage rack, hold all the hooks in magazines.
7. Baiting machine , baits the hook before the longline goes over the railing at the stern of the ship and into the sea.

This is normally not a continuous operation as illustrated in the figure. A whole fleet of hooks is deployed with an anchor in each end. The vessel returns then to the end of the fleet and hauls it on board, and the longline is stored in large magazines.

Quality

Quality is one of the key features of fishing with this technique, and there are several reasons behind this. The fish experience less stress during the hauling process, than with other conventional fishing methods like trawling. When the fish is hauled on board the vessel, it is constant cut open to bleed out and then prepared to frozen. The short time duration of this process is very important to obtain good quality.

2.2 Moonpool

Moonpools are openings right through the bottom of the ship, allowing for equipment to be lifted into the water at a location where the ship motions are at a lower magnitude. Often seen on offshore construction vessels and drill ships(Ponnappan & Sankunny 2018).

The moonpool on a longline vessel is used to haul the longline on board the vessel, as illustrated in Figure 2.3. The central hauling pool consists of to main components: The moonpool pipe is a canted circular pipe which goes from the keel of the vessel to the bottom of the moonpool basin which has a rectangular shape. This solution was developed in cooperation between several companies, H.P Holmeseth AS(Ship owner of "M/S Geir"), Fiskerstrand Verft AS(Shipyard, builder of "M/S Geir"), and Norsk Marinteknisk Forskningsinstitut, now known as Sintef Ocean(Research establishment in Trondheim, Norway)(Sintef 2004).

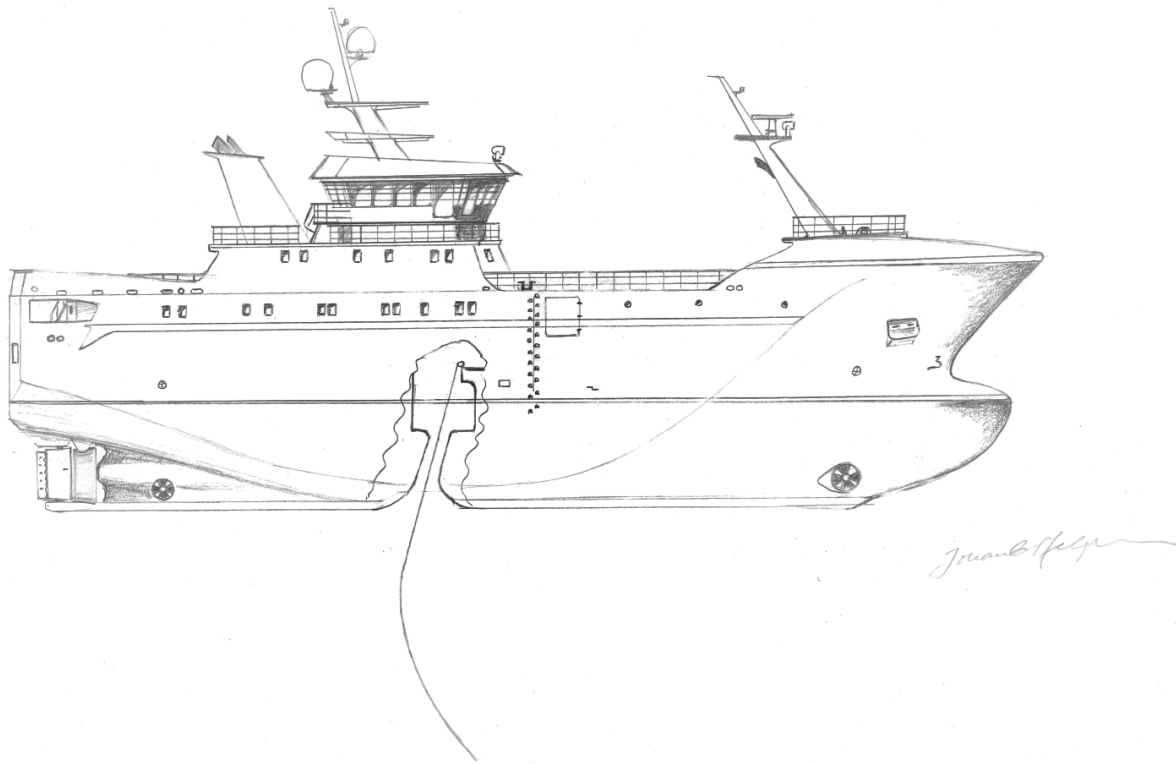


Figure 2.3: The principle of the central hauling pool(Johan G. Helgesen)

Before the moonpool for longline proposes was introduced, the hauling happened through a hatch on the starboard side of the vessels, known as the "dragerluke" in Norwegian, and directly translated into hauling hatch. The safety for the fishermen and the loss of fish was improved by moving the hauling from the open hatch on the side of the vessel inside a moonpool at midship. The safety of the crew is higher due to they are not exposed to the environment the same way as before, when waves could hit the fishermen through the open hatch. The loss of fish has also been reduced due to less violent motions in the process when the fish is coming out off the water. A study between the conventional hauling method and the moonpool has been conducted at the University of Tromsø in 2008, and the findings are represented in figure 2.4. The study shows a 84% reduction in loss of cod and a 73% reduction in loss of haddock compared with the conventional hauling method.

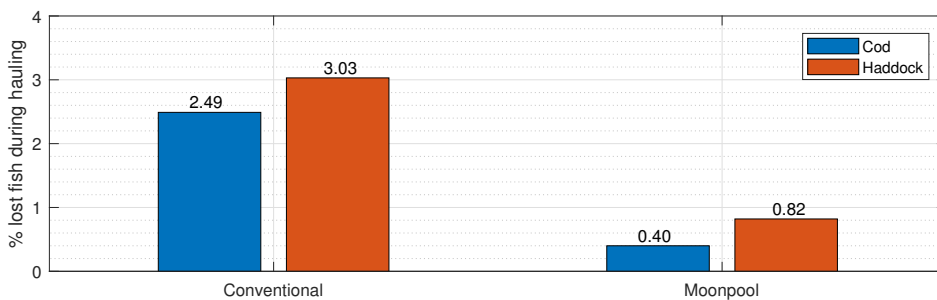


Figure 2.4: Comparison of the loss of fish between hauling methods(Larsen 2010)

There are on the other hand, some adverse effects by applying the moonpool like the utilization of space, which can lead to increased vessel size. It can also contribute to increased resistance, and higher building costs to name a few. Despite these drawbacks, it can be argued that the positive effects of the central hauling pool outweigh the adverse effects.

Since the break through of the moonpool for longline applications, there have been built several vessels. Here is a list of some of vessels with moonpool (Name, Building year, Address, Shipyard):

M/S Geir I 1998, Vatne, Fiskerstrand Verft AS

M/S Carisma Viking 2001, Raudeberg, Umoe Sterkoder

M/S Geir II 2010, Vatne, Fiskerstrand Verft AS

M/S Frøyanes 2011, Måløy, Tersan Shipyard

M/S Leinebris 2015, Raudeberg, Tersan Shipyard

M/S Veidar 2016, Godøy, Simek

FV Argos Georgia 2018, Måløy, Tersan Shipyard

FV Nordic Prince 2018, Måløy, Tersan Shipyard

M/S Seir 2018, Grytestrand, Vaagland Båtbyggeri AS

FV Argos Georgia and FV Nordic Prince are purpose built for fishing of tooth fish in the Southern Ocean, and is based on a smaller version of the hull used in this thesis (MT 1112).

2.3 Dragerbrønn

As mentioned before, moonpool on fishing vessels as we see them today were developed in an cooperation between Norsk Marinteknisk Forskningsinstitutt and Fiskerstrand Verft AS in the late 90s. Birger Enerhaug and Geir Løland were acknowledged as inventors, but Norsk Marinteknisk Forskningsinstitutt and Fiskerstrand Verft AS is stated as proprietors in the patent that was filed (Enerhaug & Løland 1998). The idea was given the name "dragerbrønn" in Norwegian, but it is known as the central hauling pool in English.

There have been done attempts get access to the research on the patent which have no expired, without any luck. The reason behind this can be many, but most likely on the background of the expired patent and they want to keep the knowledge "in-house". But there has on the other hand been some personal communication with the inventor, Birger Enerhaug and the project leader involved from Fiskerstrand Verft, Per Asle Fiskerstrand.

The first constructed moonpool on the longline vessel "M/S Geir I" had an elliptical shaped moonpool pipe, this has now changed towards a circular shape on new builds. Enerhaug (2018) claimed that the reasoning behind this was to save space inside the vessel, and that the maneuvering of the vessel over the longline was easier than first anticipated. Fiskerstrand (2019) explain the same as Enerhaug, but had in addition some remarks regarding the circulation/change of the water in the moonpool. The elliptical shape started an surge that changed the water in the moonpool at a speed of 6-7 knots, but they were no able to get the same

results with an completely circular shape. The circular shape on the other hand contributed to a calmer sea level inside the moonpool.

The moonpool should have an inclination of approximately 17° , because of the way the longline is hauled up from the sea bottom according to Fiskerstrand. The vessel has normally a forward speed towards the longline, and hauled from an astern direction so the longline has a long curve up towards the vessel, as illustrated in Figure 2.5, where the dashed line is the preferable path of the longline. This path of the line is preferable due to the longline experience less strain during hauling compared to the other hauling paths, but this is also dependant on wind, wave and current conditions (Karlsen 1997).

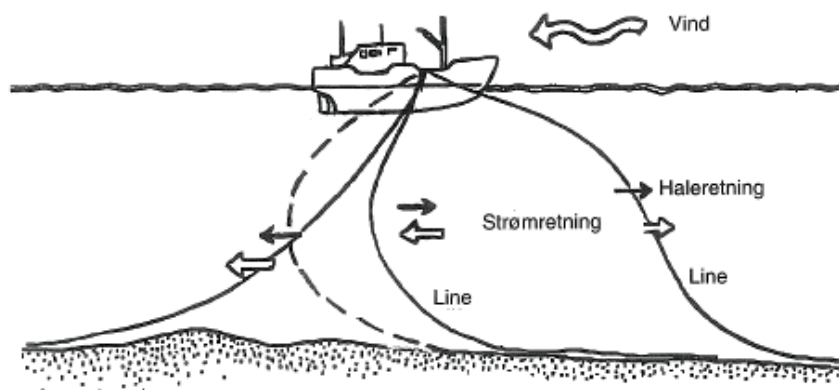


Figure 2.5: Longline hauling direction (Karlsen 1997)

Chapter 3

Theory

This chapter describes the applicable theory of the research conducted. The theory is separated into two parts, where the first part is related to the moonpool position study, where linear potential theory is used to calculate the response for the vessel in waves. The second part introduced the theory used in the moonpool shape study, where viscous fluid flow theory has been used.

It has been used two different commercially available software for this thesis. ShipX was used for the moonpool position study, and Star-CCM+ was used for the moonpool shape study. Some of the theory presented is generic, and some are directly related to the software used.

3.1 Vessel response theory

The theory used in the ShipX and the VERES plugin is based on theories developed by Salvesen et al. (1970). The theory presented in this section is an outline of the main aspects of the strip theory, based on the VERES theory manual (Fathi & Hoff 2017) and the book "Sea load in ships and offshore structures" by Faltinsen (1990).

Strip theory is a numerical method to calculate forces on and motions of a three-dimensional floating body. This is done by applying two-dimensional potential theory on the body, and this means that the viscous effects are neglected. The viscous roll dampening can, on the other hand, be accounted for using empirical data (Salvesen et al. 1970). The strip theory is carried out by slicing the vessel into a finite number of transverse sections, which are rigidly connected to one another. Each strip has a form that resembles the form of the vessel, and each strip is treated as the and infinitely long floating cylinders, as see in Figure 3.1.

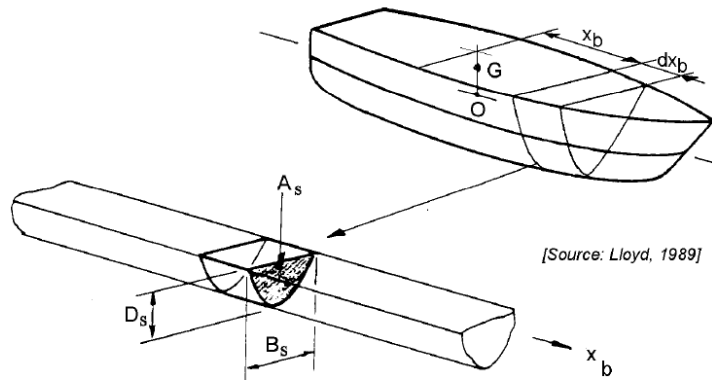


Figure 3.1: 2D strip theory principle(Journée & Massie 2002)

The idea behind this is that all the waves generated by the oscillating body and the diffraction waves are assumed to travel perpendicular to the middle line of the floating body. The load on the body is then found by integrating the 2D loads over the whole length of the body. Fundamentally, strip theory is only valid for long and slender bodies($L/B > 3$)(Journée 1992).

VERES is based on linear strip theory, and some basic underlying assumptions are made:

- Wave amplitudes are small compared to the characterizes dimensions of the vessel, and the resulting motions will then be proportionally small.
- Wave steepness is small, with other words far from breaking.

3.1.1 Forces and moments

Under the assumption that the vessel responses are linear and harmonic, the resulting six linear differential equation can be expressed as follows:

$$\sum_{k=1}^6 (M_{jk} + A_{jk})\ddot{\eta}_k + B_{jk}\dot{\eta}_k + C_{jk}\eta_k = F_{jk}e^{-i\omega t} \quad (j = 1, \dots, 6) \quad (3.1)$$

in which:

M_{jk} = Generalized components of the mass matrix

A_{jk} = Added mass matrix

B_{jk} = Linear damping matrix

C_{jk} = Stiffness matrix

F_j = are the complex amplitudes of wave exiting forces and moments

Mass forces

Mass forces are forces due to the mass of the vessel and follow Newton's laws. By assuming that the vessel is symmetric along the x-axis and that the center of gravity is located at $(0, 0, z_g)$, the generalized mass matrix can be written as:

$$M = \begin{bmatrix} M & 0 & 0 & 0 & M_{z_G} & 0 \\ 0 & M & 0 & -M_{z_G} & 0 & 0 \\ 0 & 0 & M & 0 & 0 & 0 \\ 0 & -M_{z_G} & 0 & I_4 & 0 & I_{64} \\ M_{z_G} & 0 & 0 & 0 & I_5 & 0 \\ 0 & 0 & 0 & I_{64} & 0 & I_6 \end{bmatrix}$$

where M is the displaced mass of the vessel, I_j is the inertia in the j th mode and I_{64} is the product of the yaw and roll inertia.

Added mass and dampening forces and moments

The added mass and dampening forces on the hull are steady-state hydrodynamic forces acting on the body when it is forced to oscillate in still water harmonically, also called the radiation forces (Figure 3.2). The forced motion of the vessel generates radiation waves and oscillating fluid pressure on the hull surface. By integrating these pressures over the wetted surface of the vessel, we get the forces on the body, and it is written as:

$$F_k = -A_{jk}\ddot{\eta}_k - B_{jk}\dot{\eta}_k \quad (3.2)$$

Restoring forces and moment

The restoring forces arise due to change in buoyancy and location of the center of gravity (COG) relative to the center of buoyancy (COB) when the vessel is freely floating. The restoring force is independent of the velocity potential and wave frequency and is only dependant on the geometry of the vessel and mass distribution.

$$F_j = -C_{jk}\eta_k \quad (3.3)$$

Wave excitation forces and moments

The wave excitation forces are the forces acting on the fixed body, in incoming waves, illustrated in figure 3.2. This is composed of the Froude-Krylov force which is the force on the hull due to the undisturbed pressure field from the incident waves, and the additional diffraction force due to the disturbed pressure field by the hull.

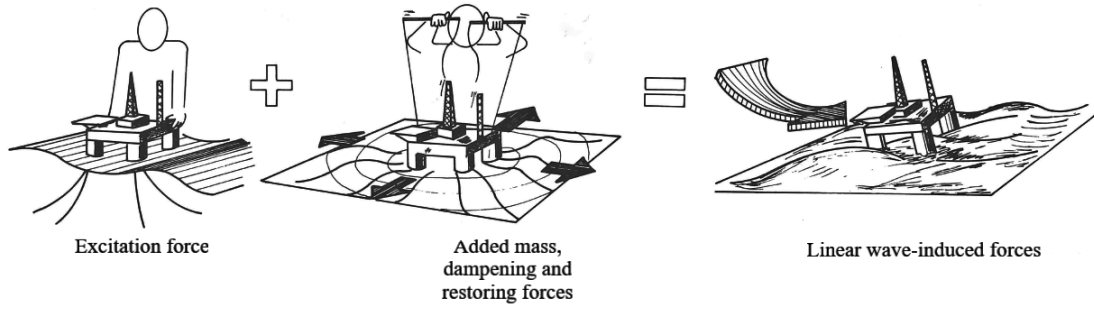


Figure 3.2: Superposition of wave excitation, added mass, damping and restoring forces (Faltinsen 1990)

3.1.2 Motion

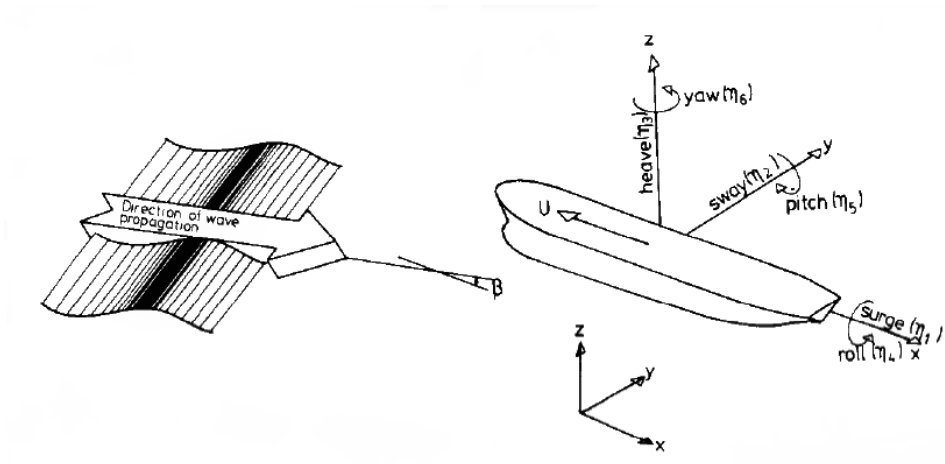


Figure 3.3: Rigid body motions and wave propagation(Faltinsen 1990)

As seen in Figure 3.3, a ship has six degrees of freedom. The motion on an vessel is described by three translations and three rotations:

$$\text{Surge: } \eta_1 = \eta_{1a} \cos(\omega_e t + \epsilon_{1\zeta}) \quad (3.4)$$

$$\text{Sway: } \eta_2 = \eta_{2a} \cos(\omega_e t + \epsilon_{2\zeta}) \quad (3.5)$$

$$\text{Heave: } \eta_3 = \eta_{3a} \cos(\omega_e t + \epsilon_{3\zeta}) \quad (3.6)$$

$$\text{Roll: } \eta_4 = \eta_{4a} \cos(\omega_e t + \epsilon_{4\zeta}) \quad (3.7)$$

$$\text{Pitch: } \eta_5 = \eta_{5a} \cos(\omega_e t + \epsilon_{5\zeta}) \quad (3.8)$$

$$\text{Yaw: } \eta_6 = \eta_{6a} \cos(\omega_e t + \epsilon_{6\zeta}) \quad (3.9)$$

where:

$$\begin{aligned}\omega_e &= \text{Wave frequency [rad/s]} \\ \epsilon_j &= \text{Phase angle in } j^{\text{th}} \text{ mode [rad]} \\ t &= \text{Time [s]}\end{aligned}$$

η_{1a} , η_{2a} , η_{3a} , η_{4a} , η_{5a} and η_{6a} are response amplitude operators(RAO), which are values that describe how a vessel react to wave height and wave period in the specific degree of freedom. By knowing the motion of the center of gravity(COG), the super positioning principle can be used to calculate the motion of any given point on the vessel. In a steadily translating case with small angles, the absolute motion can be linearized, and the coupled motions become:

$$\eta_{1p} = \eta_1 - y_p\eta_6 + z_b\eta_5 \quad (3.10)$$

$$\eta_{2p} = \eta_2 + x_p\eta_6 + z_b\eta_4 \quad (3.11)$$

$$\eta_{3p} = \eta_3 - x_p\eta_5 + y_b\eta_4 \quad (3.12)$$

in which:

$$\begin{aligned}\eta_{1p} &= \text{Longitudinal displacement of the point in questioning} \\ \eta_{2p} &= \text{Lateral displacement of the point in questioning} \\ \eta_{3p} &= \text{Vertical displacement of the point in questioning} \\ x_p &= \text{Longitudinal distance from COG to point in questioning} \\ y_p &= \text{Transverse distance from COG to point in questioning} \\ z_p &= \text{Vertical distance from COG to point in questioning}\end{aligned}$$

The derivative of the displacement with respect to time is the velocity and its second derivative with respect to time is acceleration, expressed as follows:

$$\underbrace{(\eta_{1p}, \eta_{2p}, \eta_{3p})}_{\text{Displacement}} \rightarrow \underbrace{\frac{\partial(\eta_{1p}, \eta_{2p}, \eta_{3p})}{\partial t}}_{\text{Velocity}} \rightarrow \underbrace{\frac{\partial^2(\eta_{1p}, \eta_{2p}, \eta_{3p})}{\partial t^2}}_{\text{Acceleration}}$$

3.1.3 Potential theory

Linear potential theory is applied in VERES to calculate the hydrodynamic coefficients. This implies that the viscous effects of the fluid are neglected and the fluid flow is assumed to be irrotational. The velocity potential $\Phi(x, y, z)$ must fulfill the Laplace equation(Equation 3.13) in the fluid domain.

$$\nabla^2\Phi = 0 \quad (3.13)$$

To solve this partial differential equation, boundary conditions have to be established at the hull, the free surface, and the sea bottom to replicate the physical properties at each location. This means no fluid transport over the hull surface, as stated in Equation 3.14 is equal zero.

$$\frac{DF}{Dt} = 0 \quad (3.14)$$

To replicate the physics on the free surface is more complicated, where the surface is free and is changing over time. The governing physical requirement for the free surface is equal pressure at the surface and in the surrounding air. The mathematical expression for the free surface boundary condition is expressed in the following equation.

$$\frac{Dp}{Dt} = -\rho \left(\frac{\partial \Phi}{\partial t} + \frac{1}{2} |\nabla \Phi|^2 + gz \right) = 0 \quad (3.15)$$

VERES separates the velocity potential into two parts, where one is time-independent steady(ϕ_S) contributed due to the forward motion of the vessel, and the other one is time-dependent part(ϕ_T) associated with the incident wave system and the unsteady vessel motion. These two parts are named perturbations potential(ϕ_S) and the unsteady potential(ϕ_T), respectively.

$$\Phi(x, y, z, t) = [Ux + \phi_s(x, y, z)] + \phi_T(x, y, z)e^{i\omega t} \quad (3.16)$$

Here $[Ux + \phi_s(x, y, z)]$ is the steady contribution, where U is the forward speed of the vessel. $\phi_T(x, y, z)$ is the complex amplitude of the unsteady part, and the only only the real part of ϕ_T has a physical meaning.

The geometry of the hull is assumed to have such a shape that the perturbation potential ϕ_S and its derivatives are small. The unsteady potential is linearized by assuming only small oscillatory motions, which results in that the unsteady potential and its derivatives are small. These assumptions makes is possible to linearize the boundary conditions 3.15 and 3.16, and neglect the higher order terms in both ϕ_S and ϕ_T . By linearizing the unsteady potential, it can be further decomposed:

$$\phi_T = \phi_I + \phi_D + \sum_{j=1}^6 \phi_j \eta_j \quad (3.17)$$

Where ϕ_I is the incident wave potential , ϕ_D in the diffraction potential and ϕ_j is the contribution to the potential for the j th mode of motion. The incident wave potential is written as follows:

$$\phi_I = \frac{g\zeta_a}{\omega_0} e^{kz} e^{-ik(x \cos \beta + y \sin \beta)} \quad (3.18)$$

where β is the angle of the wave heading and $\omega_0 = \sqrt{gk}$ is the wave frequency which is related to the frequency of encounter, as follows:

$$\omega_e = \omega_0 + kU \cos \beta \quad (3.19)$$

By including only linearized components about the mean hull position in the hull boundary condition, These simplifications allow for the three following linear expressions of the boundary conditions 3.14 and 3.14:

1.

The perturbation potential must satisfy the boundary conditions on the the mean hull position(Equation 3.20) and the on the undisturbed free surface(Equation 3.21)

$$\frac{\partial}{\partial n}[U x + \phi_S] = 0 \quad (3.20)$$

$$U^2 \frac{\partial^2 \phi_S}{\partial x^2} + g \frac{\partial \phi_S}{\partial z} = 0 \quad (3.21)$$

2.

The incident wave potential and the diffraction potential must stratify the following condition on the mean hull position and at the free surface.

$$\frac{\partial \phi_I}{\partial n} + \frac{\partial \phi_D}{\partial n} \quad (3.22)$$

$$\left[\left(i\omega + U \frac{\partial}{\partial x} \right) + g \frac{\partial}{\partial z} \right] (\phi_I, \phi_D) = 0 \quad (3.23)$$

3.

The potentials related to oscillatory motions must satisfy equation 3.24 on the mean hull position and equation 3.25 on the free surface $z = 0$.

$$\frac{\partial \phi_j}{\partial n} = i\omega n_j - U m_j \quad (3.24)$$

$$\left(i\omega + U \frac{\partial}{\partial x} \right)^2 \phi_j + g \frac{\partial \phi_j}{\partial z} = 0 \quad (3.25)$$

The generalized normal n_j is defined by:

$$(n_1, n_2, n_3) = \vec{n} \quad (3.26)$$

$$(n_1, n_2, n_3) = \vec{r} \times \vec{n} \quad (3.27)$$

where $\vec{r} = (x, y, z)$ is the position of the vector with respect to the origin of the coordinate system and \vec{n} is the normal vector pointing into the fluid.

$$(m_1, m_2, m_3) = \vec{m} = (\vec{n} \cdot \nabla) \nabla \left(x + \frac{1}{U} \phi_s \right) \quad (3.28)$$

$$(m_4, m_5, m_6) = \vec{r} \times \vec{m} - \nabla \left(x + \frac{1}{U} \phi_s \right) \quad (3.29)$$

$$m_j = 0 \quad j = 1, 2, 3, 4 \quad (3.30)$$

$$m_5 = n_3 \quad (3.31)$$

$$m_6 = -n_2 \quad (3.32)$$

In addition to these boundary conditions, the potentials ϕ_S , ϕ_I , ϕ_D , and ϕ_j must each satisfy the Laplace equation(3.13) and the radiation condition at infinity.

Hydrodynamic forces and coefficients

Hydrodynamic forces will act on the floating vessel due to static and time-dependent pressure in the surrounding fluid domain. The hydrostatic pressure is the origin of the restoring forces and can be calculated by analysis the submerged vessel geometry in calm water. Added mass, dampening, and the dynamic pressure field causes excitation forces due to the vessel motion and incoming waves(Sandvik 2016).

The pressure in the fluid is determined based on Bernoulli's equation and the velocity potential.

$$p = -\rho \left(\frac{\partial \Phi}{\partial t} + \frac{1}{2} |\nabla \Phi|^2 + gz \right) \quad (3.33)$$

The pressure is linearized by only including the first order components from ϕ_S and ϕ_T , and the dynamic pressure(p_d) is therefore expressed as follows:

$$p_d = -\rho \frac{\partial \Phi}{\partial t} = -\rho \left(i\omega + U \frac{\partial}{\partial x} \right) \phi_T e^{i\omega t} \quad (3.34)$$

The hydrodynamic forces and moments on the vessel is calculated by integrating the dynamic pressure over the surface of the hull

$$H_j = - \iint_S p_d n_j dS, \quad j = 1, \dots, 6 \quad (3.35)$$

Where H_1, H_2 and H_3 are the force components in x, y and z direction, and where H_4, H_5 and H_6 are the hydrodynamic moments around the x, y and z axes. H_j can further be decomposed into two parts.

$$H_j = F_j + G_j \quad (3.36)$$

where F_j is the exiting forces and moments, and G_j is the forces and moments due to vessel motion as expressed in the two following equations.

$$F_j = \rho \iint_S n_j \left(i\omega + U \frac{\partial}{\partial x} \right) (\phi_I + \phi_D) dS \quad (3.37)$$

$$G_j = \rho \iint_S n_j \left(i\omega + U \frac{\partial}{\partial x} \right) \sum_{k=1}^6 \phi_k \eta_k dS = \sum_{k=1}^6 T_j \eta_k \quad (3.38)$$

T_j represents the hydrodynamic forces and moments in the j th direction due to unit displacement in the k th mode, and can be split up into a real and an imaginary parts as follows:

$$T_{jk} = \omega^2 A_{jk} - i\omega B_{jk} \quad (3.39)$$

where A_{jk} is the frequency dependant added mass coefficient and B_{jk} is the dampening coefficient.

Local analysis of each strip

The diffraction and radiation problems are solved by matching the near and far field solutions. A boundary element formulation is applied to find the near field solutions, and the far field solutions are found by asymptotic analysis. Green's 2nd identity(3.40) is used to represent the velocity potential. This is done by distributing fundamental 2D sources and dipoles over the boundaries of the control surface. Figure 3.4 illustrates the fluid domain and the control surface.

$$-2\pi\phi = \int_S \left(\phi \frac{\partial \log(r)}{\partial n} - \log(r) \frac{\partial \phi}{\partial n} \right) ds \quad (3.40)$$

The hull is represented by straight line elements, and each element is assumed to have a constant value for the velocity potential and its normal derivative.

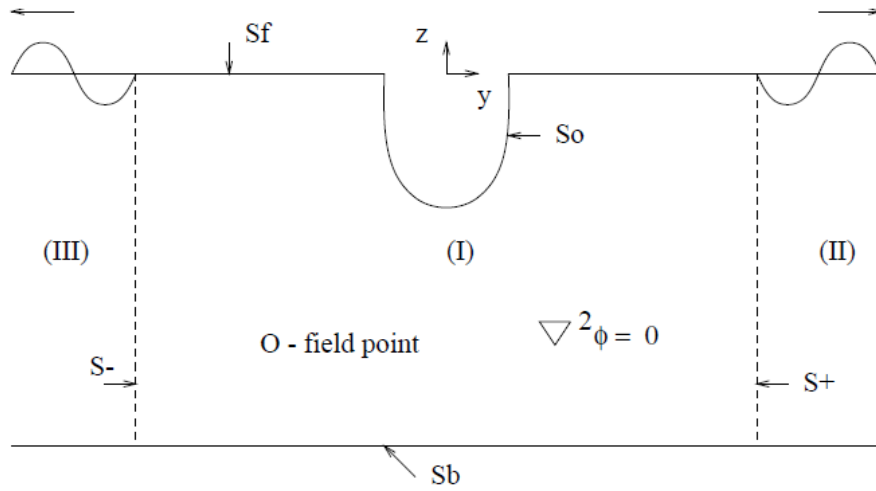


Figure 3.4: 2D fluid domain and control surface

VERES calculates the magnitude of each potential by setting up a $n \times n$ linear equation system, where n is the number of unknowns. The velocity potential (ϕ) at the hull surface (S_0) is unknown, and the normal derivative of the velocity potential ($\frac{\partial \phi}{\partial n}$) at the free surface (S_f) is unknown. The velocity potential magnitude is on the other hand known at the free surface through the free surface condition (Equation 3.15).

This method is applied for both low-speed and high-speed strip theory, but VERES applies different theories dependant on the speed and shape of the object to be analyzed. Some changes are made in the boundary conditions on the free surface and the integration over the body for the two different methods. The thesis concerns a vessel, and a speed where the low-speed strip theory is applicable. The theory behind both low-speed and high-speed strip theory can be found in the VERES theory manual (Fathi & Hoff 2017), or from its origin; "Ship Motions and Sea Loads" by Salvesen et al. (1970).

3.1.4 Moonpool effects

VERES includes the effects of the moonpool in a simplified manner, where the intention is to correct the displacement and restoring forces. The following effects are included in the moonpool module (Fathi 2018):

- The displacement of the vessel is corrected by subtraction of the volume of the moonpool.
- The center of buoyancy is corrected.
- The longitudinal and transverse metacentric height is corrected.
- The mass and restoring matrices are corrected.
- The Froude-Krylov forces in the area of the moonpool is subtracted from the wave exciting forces.
- Added mass in surge, sway and yaw including the additional mass of the water in the moonpool

The following illustration and table describes the required input dimensions for the moonpool module. The module is developed for rectangular moonpools, and this follows that it is the most common type for offshore applications.

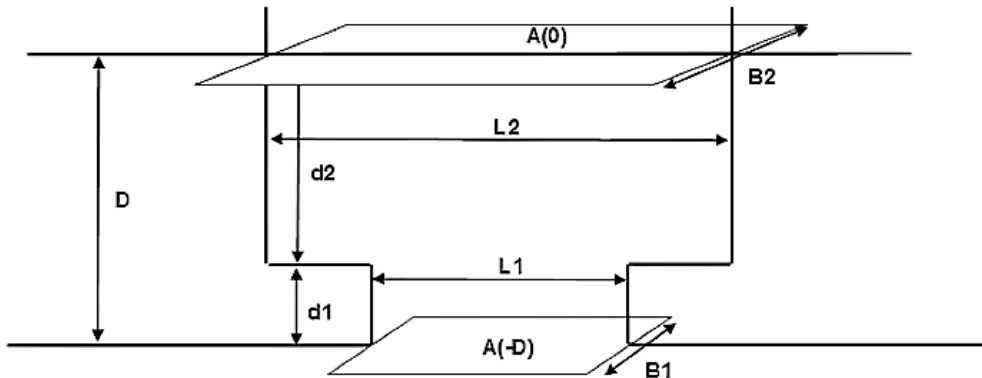


Figure 3.5: Schematic side view of rectangular moonpool(Fathi 2018)

Table 3.1: Moonpool parameters in VERES

Parameter	Description
$A(0)$	Water plane area
$A(-D)$	Area of moonpool opening
$B1$	Width of moonpool opening
$B2$	Width of moonpool
D	Depth of moonpool
$d1$	Height of moonpool opening
$d2$	Height between open restriction and waterline
$L1$	Length of moonpool opening
$L2$	Length of moonpool

3.1.5 Short term statistics

Calculating short term statistics are done by by combining the RAO of the vessel with a wave spectra, which results in a response spectra:

$$S_{\zeta\zeta}(\omega) = |H_{\eta\eta}(\omega)|^2 \cdot S_{\zeta\zeta}(\omega) \quad (3.41)$$

where $S_{\zeta\zeta}(\omega)$ is the resulting response spectra, $H_{\eta\eta}(\omega)$ is the RAO, and $S_{\zeta\zeta}(\omega)$ is the applied wave spectra.

A wave spectrum is a mathematical representation of a sea state, typical over a period of 3 hours. The wave spectra describe how the energy in a sea state is distributed for different wave frequencies. This gives the opportunity to give the results for actual sea states that actual can accrue, and it easier to relate to results given in commonly known measurement units like

displacement in m , velocity in m/s , and acceleration in m/s^2 , rather than RAOs which can be harder to interpreted and relate to.

The selection of wave spectra is important for the results, and it is essential that the right physical properties are represented. The different wave spectra are available in VERES: Pierson-Moskowitz, Torsethaugen, and JONSWAP spectra. The one utilized in this thesis is the JONSWAP spectra, describes in the following section.

Long term statistics could have been used in addition to calculate the operability and probability of exceedance of criterion, but this requires that there are operability criterion and limiting sea state data available for the longline operation. Such criterion are not established.

Joint North Sea Wave Project Spectra

The Joint North Sea Wave Project Spectra known as JONSWAP is developed using data collected from the North Sea. Research done by Orimolade & Gudmestad (2016) shows that the JONSWAP spectrum can also be used in the Barents Sea. However, the wave environment in the Barents Sea is, on the other hand, composed of both wind sea and swell, and a double-peaked wave spectrum like Torsethaugen it therefore preferred. For simplicity in this thesis, only a one peaked JONSWAP spectrum is implemented.

For a given sea state, the total energy is constant regardless of choice of wave spectra. The JONSWAP spectrum uses a peakness parameter γ , which determines the concentration of the spectrum about the peak frequency illustrated in figure 3.6.

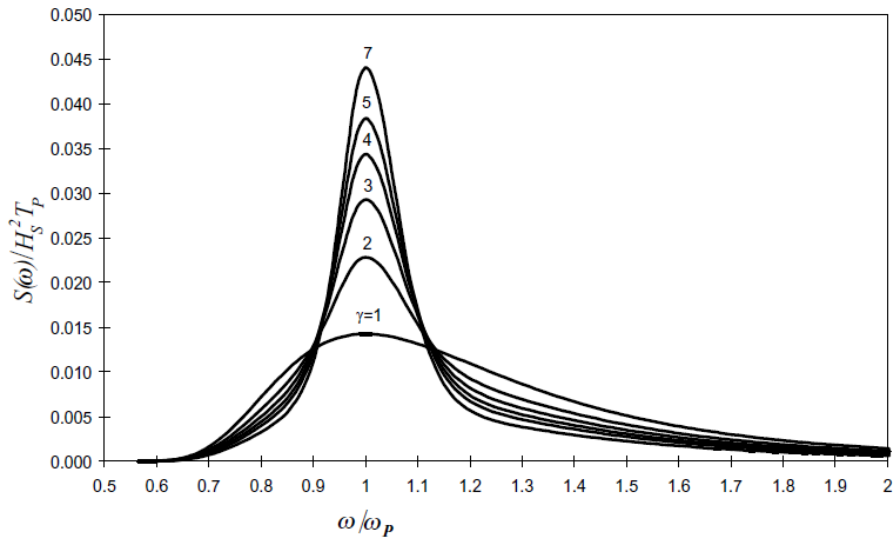


Figure 3.6: JONSWAP spectra for $\gamma = 1 - 7$ (Fathi & Hoff 2017)

3.2 Fluid flow theory

The viscous, incompressible fluid flow around the ship can be determined by solving the Navier-Stokes(NS) equations. This section is devoted to explaining some of the fundamentals of computational fluid dynamics and some of the philosophy behind the simulations that will be described in the chapter related to the moonpool shape study.

3.2.1 Computational fluid dynamics theory

CFD are a branch in fluid dynamics and is used to solve fluid flow problems by applying numerical integration methods and algorithms. This is done by making an mathematical formulation of the problem, by choosing governing equations and boundary conditions. The next step is to develop an numerical formulation of the equations and the boundary conditions. The problem is then solved in spatial coordinates as the fluid flow evolves over time.

The type of governing equation applied to the model depends on what type of problem that is going to be solved. The different governing equations have different features and simplification, and it is essential to choose the right equations to get a result which captures the real physics of the problem. The different equations can solve compressible and incompressible fluid, viscous and inviscid fluid, laminar and turbulent viscous flow conditions, rotational or irrotational flow, single or multi-phase(Faltinsen 2009).

There are many different methods, and they are normally divided into two categories; Navier-Stokes methods and potential flow methods, as used for the moonpool position study in chapter 4. Simulation of viscous flows around a ship hull is done by approximating the Navier-Stokes equation numerically.

Governing equation

The continuity equation 3.42 and the conservation of momentum 3.43 are the NS equations for a incompressible fluid flow:

$$\nabla \cdot \mathbf{u} = 0 \quad (3.42)$$

$$\underbrace{\frac{\partial \mathbf{u}}{\partial t}}_{\text{Time derivative}} + \underbrace{(\mathbf{u} \cdot \nabla) \mathbf{u}}_{\text{Convection}} = \underbrace{-\frac{1}{\rho} \nabla p}_{\text{Pressure gradient}} + \underbrace{\nu \Delta \mathbf{u}}_{\text{Diffusion}} + \underbrace{\frac{1}{\rho} \mathbf{f}}_{\text{Volume force}} \quad (3.43)$$

in which:

- \mathbf{u} = Velocity vector
- \mathbf{f} = Volume force
- p = Scalar pressure
- ρ = Constant density, which makes the flow incompressible

3.2.2 Turbulence modeling

A ship has a large Reynolds number ($R_e \approx 10^8$) which means that it is in the turbulent regime. The Reynolds Average Navier-Stokes (RANS) is therefore used to compute the turbulent flow. The RANS equations 3.46 and 3.47 is derived from the NS by splitting the field variables for velocity u_i and pressure p into mean values ($\overline{u_i}, \overline{p_i}$) and a fluctuation part (u'_i, p'_i).

$$u_i = \overline{u_i} + u'_i \quad (3.44)$$

$$p = \overline{p_i} + p'_i \quad (3.45)$$

The RANS variables is inserted into the NS equation, and a additional term called the Reynolds stress tensor is generated ($\overline{u'_i u'_j}$). This tensor contains additional unknowns which are determined with the use of a turbulence model, with is explained in the following subsection.

$$\overline{u_j} \frac{\partial \overline{u_i}}{\partial x_j} = 0 \quad (3.46)$$

$$\frac{\partial \overline{u_i}}{\partial t} + \frac{\partial}{\partial x_j} \left[\overline{u_i u_j} + \overline{u'_i u'_j} \right] = -\frac{1}{\rho} \frac{\partial \overline{p}}{\partial x_j} + \nu \frac{\partial}{\partial x_j} \left[\frac{\partial \overline{u_i}}{\partial x_j} + \frac{\partial \overline{u_i}}{\partial x_i} \right] \quad (3.47)$$

The turbulence model should resolve the large vortex structures within the computational mesh, and represent the high frequent turbulent part with a turbulence model.

k - ϵ turbulence model

The k - ϵ turbulence model is a two-equation turbulence model that solves the transport equations for the kinetic energy k and the turbulent dissipation rate ϵ in order to determine the turbulent eddy viscosity. There are different k - ϵ models available in Star-CCM+, but the one that was used in these simulations was the realizable k - ϵ two-layer model. The realizable k - ϵ model adds an additional transport equation for the dissipation rate ϵ , rather than assuming that it is constant as with the standard model.

The two-layer approach divided the computation into two layers. The turbulent dissipation rate (ϵ) and the turbulent viscosity (μ_t) are specified as a function of the wall distance on the layer next to the wall. The equation for turbulent kinetic energy is solved for the entire domain and the values for ϵ is blended smoothly with the computed values for the transport equation far from the wall.

The k - ϵ have proven able to give accurate predictions in ship hydrodynamics (ITTC - Recommended Procedures and Guidelines 2011), and was therefor applied to these simulations.

3.2.3 Finite volume method

There are several discretization methods available for CFD, and the one used in this research is the Finite Volume Method (FVM). The finite volume method is a numerical technique to

transform the partial differential equations representing the governing equations over differential volumes into discrete algebraic equations over finite volumes(Moukalled et al. 2016). The FVM process follows these steps:

1. Divide the domain into a number of finite sized sub-domains, known as cells. Each cell is represented by a finite number of grid points.
2. Integrate the governing differential equations over the cells to transform them into algebraic equations.
3. The algebraic equations are then solved to compute the values of the dependant variables for each element.

3.2.4 Multi-phase flow

The vessel is operating in two fluids(water and air), and the free surface between the fluid has to be simulated. This is done by the use of the Eulerian multiphase and the volume of fluid(VOF) method. The Eulerian multi-phase model allows for several fluids of different densities and viscosities to exist within the same boundary and is necessary when using the VOF model. The VOF uses a scalar value $\alpha \in [0, 1]$ to define the amount on the water within the control volume of a cell. The dynamic behaviour of α is defined by the transport equation(Equation 3.48).

$$\frac{\partial \alpha}{\partial t} + \nabla \cdot (\mathbf{u}\alpha) = 0 \quad (3.48)$$

Equation 3.49 and 3.50 handle the mixed properties of the fluids at the free surface, where the dynamic viscosity μ and the density ρ is change dependant the mix. μ_1 and μ_2 are the dynamic viscosities of the two different fluids and ρ_1 and ρ_2 are the densities of the respective fluids.

$$\mu = \alpha\mu_0 + (1 - \alpha)\mu_1 \quad (3.49)$$

$$\rho = \alpha\rho_0 + (1 - \alpha)\rho_1 \quad (3.50)$$

3.2.5 Boundary layer

Resolving the near wall boundary layer usually is an essential aspect of obtaining a good simulation result. There are two main approaches to resolve the boundary layer near the surface. One of the approaches is to have a very fine mesh resolution near the surface, so-called fine near wall treatment. The other approach is to apply a wall function, which allows for a much coarser mesh. The wall function approach is applied in these simulations, and the near wall cell height is determined by the dimensionless wall distance y^+ defined in equation 3.51, found in the recommended procedures by ITTC - Recommended Procedures and Guidelines (2011).

$$y = \frac{y^+}{Re\sqrt{\frac{C_f}{2}}} L_{PP} \quad (3.51)$$

where y is the absolute distance from the wall and C_f is the skin friction coefficient given by equation 3.52

$$C_f = \frac{0.075}{(\log_{10}(Re - 2))^2} \quad (3.52)$$

Star-CCM+ offers three different wall treatment functions: Low y^+ wall treatment, High y^+ wall treatment, and All y^+ wall treatment. The All y^+ wall treatment is applied to these simulations, and it is a hybrid between the two other functions. This model can resemble the behavior of the two other models for both fine and coarse mesh..

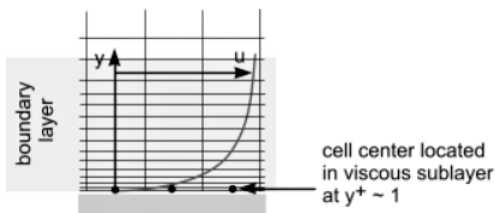


Figure 3.7: Low y^+ wall approach (Star-CCM+ 2018)

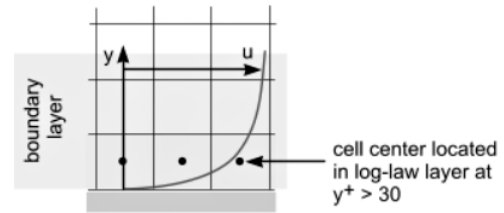


Figure 3.8: High y^+ wall approach (Star-CCM+ 2018)

The Low y^+ wall treatment is consistent with a low Re simulation, and this model assumed that the viscous sublayer is fully resolved. The y^+ should be kept between 1 and 5 for this function. The High y^+ wall treatment is a wall function approach which uses equilibrium turbulent boundary layer theory to derive the wall shear stress. The desirable value for this approach is $30 < y^+ < 50$, and the recommended value for the All y^+ is according to this functions mentioned above, and is illustrated in figure 3.9 were the desirable values are outside of the buffer layer region. A more extensive outline of the available wall functions and theory can be found in the Star-CCM+ user manual(Star-CCM+ 2018).

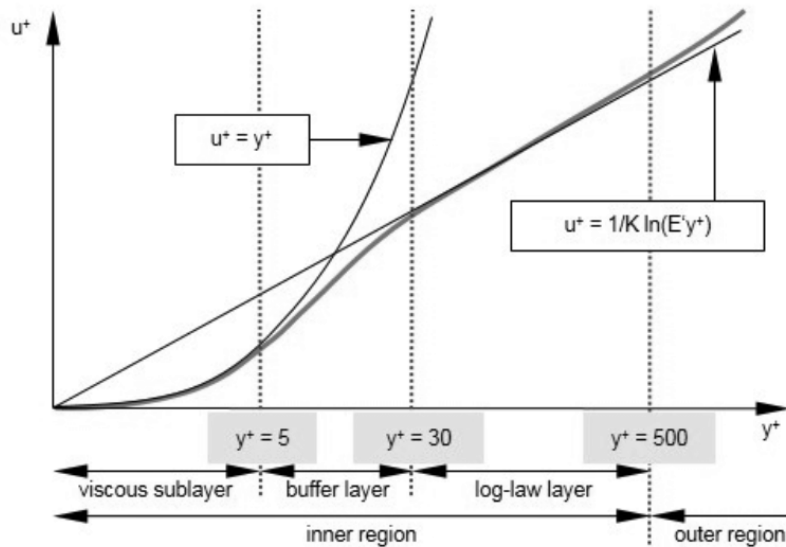


Figure 3.9: y^+ value regions (Star-CCM+ 2018)

3.2.6 Time step and inner iterations

The time step is normally set according to the Courant Friedrichs Lewy condition(CFL) in CFD. The CFL number is a dimensionless number used to find a suitable ratio between the mesh, flow, and time step. The CFL number tells how the fluid moves through the computational cells and is formulated as follows:

$$CFL = \frac{u \Delta t}{\Delta x} \quad (3.53)$$

where u is the velocity magnitude of the fluid, Δt is the time step and Δx is the characteristic cell length and is illustrated in figure 3.10.

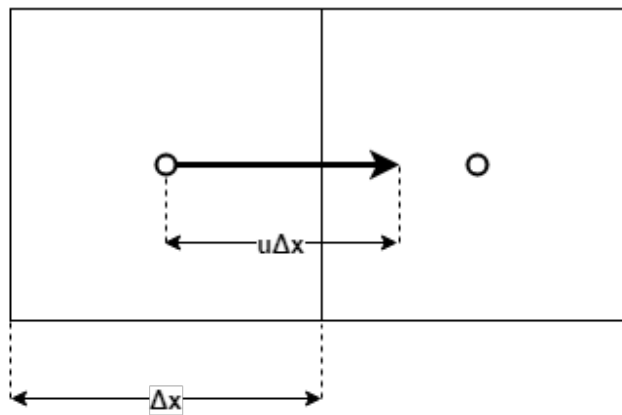


Figure 3.10: Courant Friedrichs Lewy Condition principle

The different numerical schemes have different sensitivity to the CFL number, explained in the next subsection. The recommend CFL number for a transient simulation with the use of the VOF method is between 0.4 – 0.5 at the free surface.

For every time step, a number of inner iterations are solved. The number of inner iterations needed is dependant on how much the flow changes from one time step to another in a transient case. Correspondingly, a steady state simulation is solved by the use of inner iterations only.

3.2.7 Implicit unsteady

The implicit unsteady integration scheme calculates the solution by solving the equations involving both the current state and the following state. It was chosen due to its features regarding unsteady, incompressible flows with turbulence. Implicit unsteady is proven to have a wide stability range, where the CFL number can exceed 1, but does however, require more memory compared to other methods(Star-CCM+ 2018).

3.2.8 Boundary conditions and initial conditions

The boundaries are surfaces that define the boundaries of the mathematical model of the domain. The following four boundary conditions were applied to the simulations carried out in this thesis, and the application of the different condition are further explained in the relevant cases.

Wall

The wall condition represents a surface where there is no fluid transport over the surface. By default, the wall boundary has a no-slip condition, which means that the fluid sticks to the wall and travels in the same velocity as the wall. These simulations are in the turbulent regime, and a near wall treatment is therefore applied to resolve the shear in the fluid close to the wall. This is described in subsection 3.2.5.

Symmetry plane

The symmetry plane boundary condition represents an imaginary plane of symmetry in the simulation and is used to reduce the extent of the computational domain. The symmetry plane condition has the same properties as a wall boundary with a slip condition, which means that the shear stress in the fluid is zero. The face values of the velocity and pressures are calculated by extrapolating the parallel components of velocity and pressure from the neighboring cells by the use of reconstruction gradients(Svoren 2015).

Velocity inlet

The velocity inlet is used as an inflow condition where the velocity and fluid properties are known. The pressure is not specified because this would lead to mathematical over-specification.

Pressure outlet

The pressure outlet is an outlet condition where fluid flows out the computational domain. The pressure in these simulations is specified according to the hydrostatic pressure of the water.

Initial conditions

Initial conditions are specified for the simulations and are essential for the path to a converged solution and especially to save computational time. However, a converged solution should be independent of the initial conditions. Examples of initial conditions are velocity, pressure, volume fractions, and turbulence quantities.

The initiation of a new simulation is like a pulse going through the domain, and it can take a long time to stabilize the simulation, especially with a free surface. There are different ways

to dampen this effect. One approach is to gradually increase the velocity of the fluid from zero, and in this way eliminate the big pulse at the start, completely. But this method does, however, require extensive coding. Another solution is to ramp up the time step at the start of the simulation, to flush out the transients. This method is easiest to apply to the simulations and was utilized in the simulations carried out.

3.2.9 Mesh

The mesh is defined as the discretized representation of the computational domain, which the physics solvers use to provide a numerical solution. The quality of simulation is highly dependant on the mesh quality, and Star-CCM+ offers a wide range of integrated meshing options, which is capable of generating a wide variety of topologies. The four following meshing tools have been utilized in generating the volume mesh in this thesis.

Trimmed cell mesher

The trimmed cell mesher presents an efficient way to create high-quality grids for simple as well as complex geometries. It combines several desirable meshing attributes into one meshing scheme. It uses mainly hexahedral cells with minimal skewness and does also allow for local refinements.

Surface remesher and Automatic surface repair

The surface remesher is used to re-triangulate the surface to improve the overall quality of existing surfaces and is governed by curvature and surface proximity. The automatic surface repair was used in addition to the preliminary repair of the surface done after the import of the geometry files.

Prism layer mesher

The prism layer mesher produces a prismatic volume mesh orthogonal to the wall surface, and is related to the resolving of the boundary layer explained in subsection 3.2.5. The prism layer mesh is built up by scaling down the starting surface for internal flows or scaling up for external flows.

3.2.10 Passive Scalar

Passive scalar is used to simulate the transport of a scalar quantity within the incompressible fluid and is in this case used to visualize how the interaction between the fluid flow underneath the ship and the fluid inside the moonpool. The transport equation for the passive scalar is expressed as follows(Star-CCM+ 2018):

$$\frac{\partial}{\partial t} \int_V \rho \phi_i \alpha_i \chi dV + \oint_A \rho \phi_i V \alpha_i \chi dA = \oint_A j_i \alpha_i \chi dA + \int_V S_{\phi_i} dV \quad (3.54)$$

where:

- i = Component indexes, which in this case is 0 and 1 for dirty and clean fluid, respectively.
- α_i = Volume fraction of phase i
- χ = Void fraction
- j_i = Diffusion flux
- S_{ϕ_i} = Source term for passive scalar i
- ϕ_i = Assumed to be positive-definite

There are some limitations to the use of passive scalars. The passive scalar function in Star-CCM+ cannot distinguish between water and air, and this will be further discussed later on.

Chapter 4

Moonpool Position Study

This chapter describes the moonpool position study with applicable methodology and results. The intention with this chapter is to solve research question 1. described in the introduction, where the goal is to find the ideal longitudinal position of the moonpool and rail-roll with respect to vertical motions.

Typical forward speed for a longline vessel during the hauling process is 3 knots, which relates to the speed of the longline hauler. The vessel speed is kept constant for the position study.

4.1 Method

The position of the moonpool and rail-roll is ideal at the position where the longline experience the lowest magnitude of vertical acceleration to limit the strain on the longline and to avoid that the fish is torn off the hook. This can be justified by Newton's 2nd law: $F = m \cdot \ddot{\eta}$. Where F is the force on the object, $\ddot{\eta}$ is acceleration at the object in question, and m is the mass of the object which in this case can be the fish or the longline. Higher accelerations will inevitably lead to higher forces on the fish and longline gear.

The moonpool position study followed these steps:

1.

A vessel response analysis on the hull without moonpool was carried out to have data to compare with the other analysis, and to define a reference point for the moonpool locations. The longitudinal center of buoyancy found from this analysis was used as a reference point for the study of the ideal position.

2.

The next step was to shift the longitudinal position of the moonpool and rail-roll both forward and aft of LCB and calculate the response at every given point. The setup and findings from these analyses are presented in the succeeding sections.

4.1.1 ShipX and VERES

ShipX is a workbench for hydrodynamic analysis of floating structures, mainly ships. ShipX is developed by Marintek, now known as Sintef Ocean. The workbench consists of many plugins like resistance calculations, station keeping, maneuvering, and the vessel response calculation plugin VERES, which is used in this study.

VERES offers the possibility to calculate ship motions and global loads, with including both long and short time statistics, and operability.

4.2 Setup

4.2.1 Wave periods and headings

The environmental condition was set up according to the default values for wave period in ShipX, and the wave directions were set to a 30° increment around half the vessel.

- **Wave period(T):** $4.0s, 4.5s, 5.0s, 5.5s, 6.0s, 6.5s, 7.0s, 7.5s, 8.0s, 8.5s, 9.0s, 10.0s, 11.0s, 12.0s, 13.0s, 14.0s, 15.0s, 16.0s, 17.0s, 18.0s, 19.0s, 20.0s, 25.0s$ and $30.0s$
- **Wave directions(β):** $0^\circ, 30^\circ, 60^\circ, 90^\circ, 120^\circ, 150^\circ$ and 180°

4.2.2 Vertical force estimator

VERES offers a Vertical Force Estimator(VFE) when dealing with the motion of body-fixed objects on the vessel, where the results for the response are given in g-force. This function is additionally available for the lateral and longitudinal directions and is often used to calculate the probability for motion sickness. It is in this case used to calculate the vertical acceleration($\ddot{\eta}_3$) at the rail-roll, and is expressed as follows:

$$VFE(x, y, z) = -\ddot{\eta}_3(x, y, z) \quad (4.1)$$

4.2.3 Short term statistics

The short term statistics setting in VERES was set according to the following specifications:

- **Spectra:** JONSWAP
- **Peakness(γ):** 2
- **Significant wave height(H_s):** $3.5 m$
- **Peak period:** $5 - 20s$, at steps of 1 second.

These settings were chosen to challenge the vessel and based on the wave scatter diagram for the Barents Sea C-block found in Barents East blocks Metocean Design Basis(Dezecot & Eik 2015). A sea state with a significant wave height over 3.5 m does only occur 19% of the time over a period of 100 years and 292 002 different sea states.

The sea states found in the Barents Sea scatter is not necessarily the worst which longline vessels are operating in since the location for fishing is dependant on season and fish species of interest. The Barents Sea scatter was on the other hand chosen on the basis of available data.

4.2.4 Vessel

The loading condition specified in VERES is according to a loading condition with 50% consumables and load on deck for the MT1114 hull, which results in a draft of 4.42 m , a aft trim of 0.97 m , and a volume displacement of 2251 m^3 without moonpool. The draft and trim is kept steady, and the subtracted volume of the moonpool is not taken into account for this load case. The main dimensions of the vessel are described in Table 4.1

Table 4.1: Hull dimensions of MT1114

Parameter	Value	Unit
Length o.a.	63.46	m^2
Length b.p.p.	56.40	m^2
Breath	14.60	m
Depth main deck	5.90	m

4.2.5 Moonpool

The moonpool module in ShipX is developed for rectangular moonpools, the dimensions for the initial circular moonpool was converted into the rectangular shape. The area of the cross-section of the moonpool pipe was $A_o = \pi r^2 = \pi(0.75)^2 = 1.77[m^2]$, and by taking the root of the area you get the length and width of the square moonpool ($L, B = \sqrt{A_o} = \sqrt{1.77} = 1.33[m]$). This can be done since the moonpool module of VERES is a simplification and does not take the dynamic effects in the moonpool into account, as described in subsection 3.1.4.

The other dimensions are set according to the general arrangement(GA) of the vessel in question and presented in the following table. These dimensions are related to the Figure 3.5.

Table 4.2: Moonpool dimensions

Parameter	Value	Unit
A(0)	15.12	m^2
A(-D)	1.77	m^2
B1	1.33	m
B2	3.6	m
L1	1.33	m
L2	4.2	m

The dimensions, $d1$ and $d2$ was varied dependant on the longitudinal position of the moonpool, due to varying lengths of the moonpool pipe because of the rise of the keel on the vessel.

4.2.6 Moonpool positions

The position of the moonpool has to correlate to the position of the rail-roll, where the longline goes over the railing on the vessel. The vertical position of the rail-roll is set as a fixed value of 1350mm above the main deck(7250mm above baseline) on the vessel, this is illustrated in Figure 5.9 This is according to the general arrangement of the vessel in questioning. The moonpool and the rail-roll are at the same time assumed to be at the center of the vessel in the transverse direction.

Several different longitudinal positions of the moonpool were investigated, where the longitudinal center of buoyancy(LCB) for the vessel without moonpool was used as a reference point. The moonpool was moved according to Figure 4.1, where all the investigated positions are displayed.

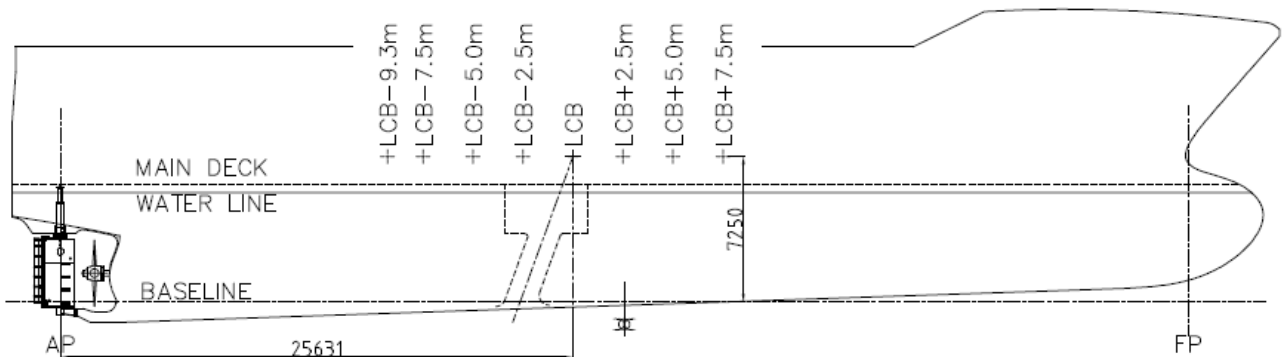


Figure 4.1: Longitudinal moonpool positions

The position 9.3 m aft of LCB is referred to as the longitudinal center of flotation(LCF).

4.3 Results

The four following plot presents the vertical acceleration at the rail-roll for four different cases expressed in g-force. The plots show the response for every wave heading, were 0° is head seas. This means that the vessel encounters the waves from ahead with other words. The peak period varying from 5 s to 20 s and the significant wave height was fixed to $H_s = 3.5\text{ m}$ according to the setup. The conventional vessel refereed to in the results is the vessel without moonpool.

Figure 4.2 shows the response for the rail-roll location on a conventional ship without moonpool at LCB(25.631 m forward of AP).

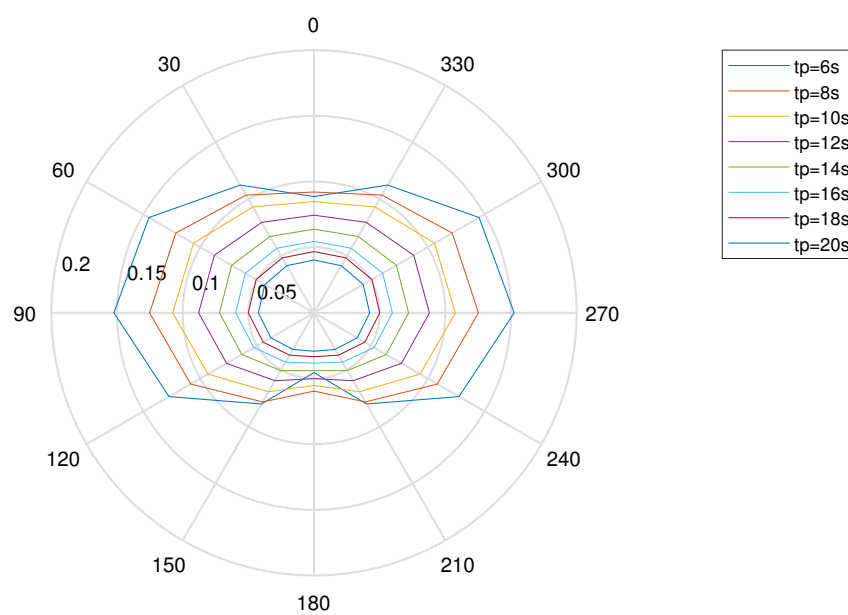


Figure 4.2: Response at rail-roll on conventional vessel at LCB[g]

Figure 4.3 shows the response for the rail-roll for a vessel with a moonpool at LCB(25.631 m forward of AP).

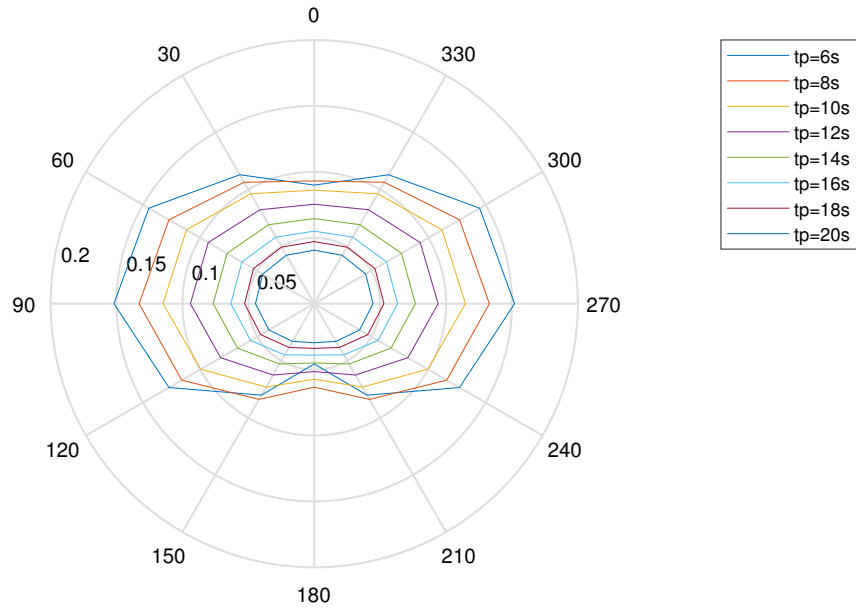


Figure 4.3: Response at rail-roll on vessel with moonpool at LCB[g]

Figure 4.4 presents the response of the rail-roll for a vessel with a moonpool 5 m forward of LCB(30.631 m forward of AP).

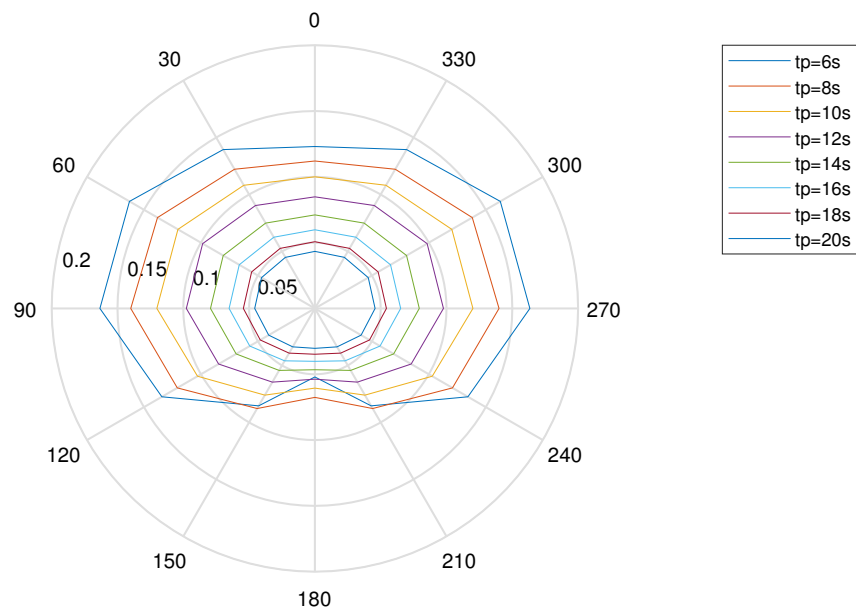


Figure 4.4: Response at rail-roll on vessel with moonpool placed 5 m forward of LCB[g]

Figure 4.5 shows the response at the rail-roll for a vessel with the moonpool 5 m aft of LCB(20.631 m forward of AP).

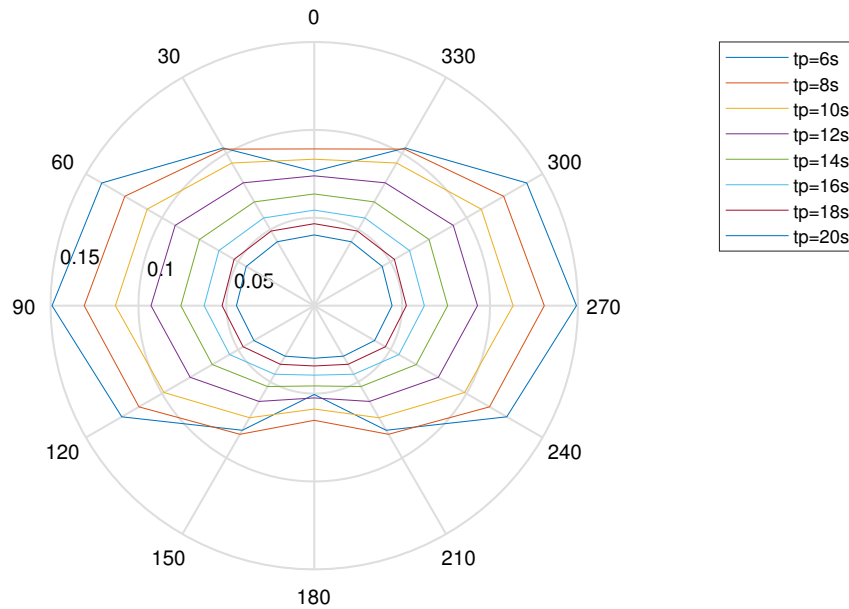


Figure 4.5: Response at rail-roll on vessel with moonpool placed 5 m aft of LCB[g]

Figure 4.6 present the response for the four previous cases for a peak period of 10.0 s. The peak period of 10.0 s was chosen because it is most likely to accrue at a significant wave height of 3.5 m according to the scatter diagram for the Barents sea C-block(Dezecot & Eik (2015)).

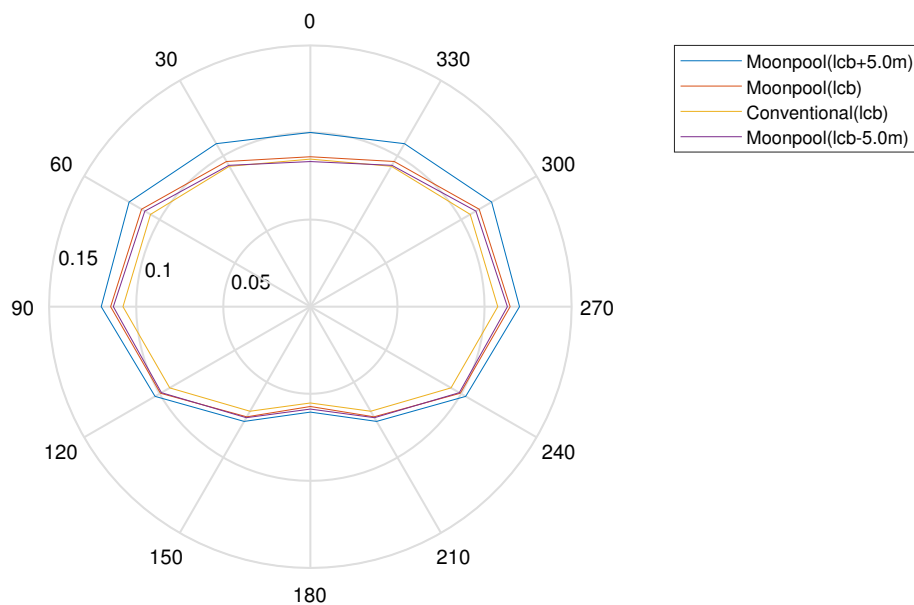


Figure 4.6: Response at rail-roll for for all moonpool positions at $T_P = 10.0$ s

The two following plots shows the vertical response of the rail-roll at moonpool positions at LCB and $LCB \pm 5.0 m$ for head and beam seas, Figure 4.7 and Figure 4.8, respectively.

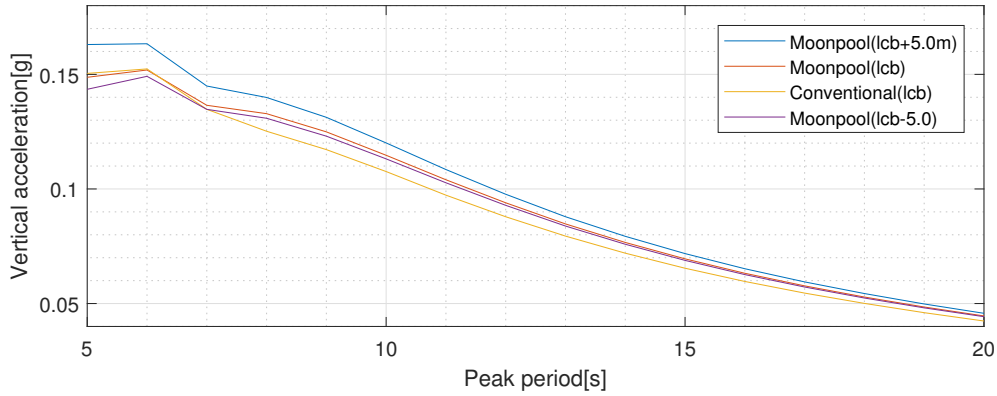


Figure 4.7: Response at rail-roll for moonpool positions at LCB and $LCB \pm 5.0 m$ in beam seas

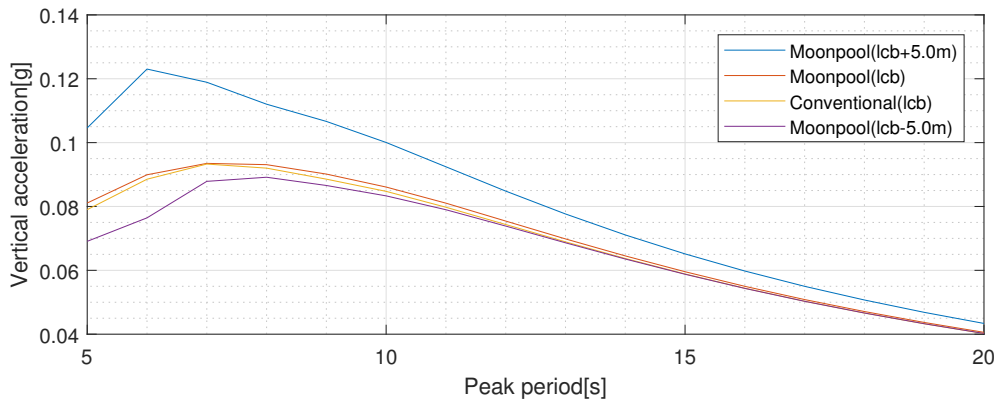


Figure 4.8: Response at rail-roll for moonpool positions at LCB and $LCB \pm 5.0 m$ in head seas

The interpretation of this result is that the longitudinal position of moonpool and rail-roll is not as sensitive for beams seas as with head seas. Only head seas are therefor assessed further.

Figure 4.9 shows the results for the positions of the rail-roll behind of LCB, and Figure 4.10 have the additional results for the same points for the conventional vessel without moonpool, to see the influence of the moonpool on vessel response by applying the moonpool.

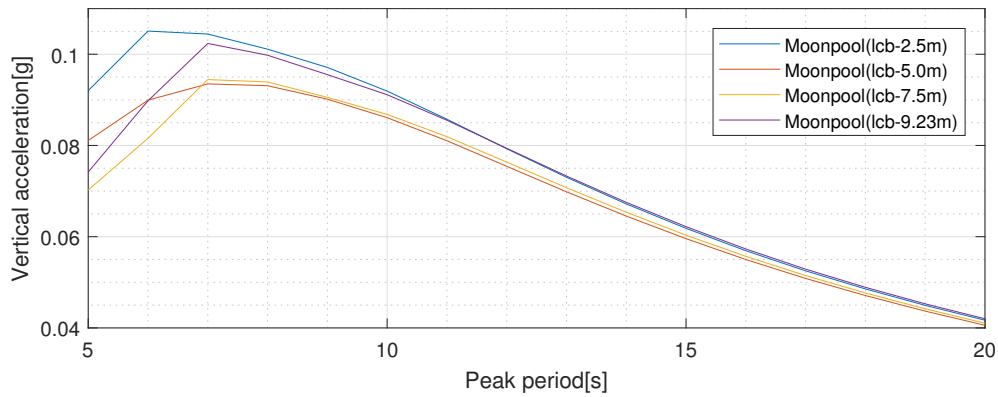


Figure 4.9: Response at rail-roll for for moonpool positions aft of LCB in head seas

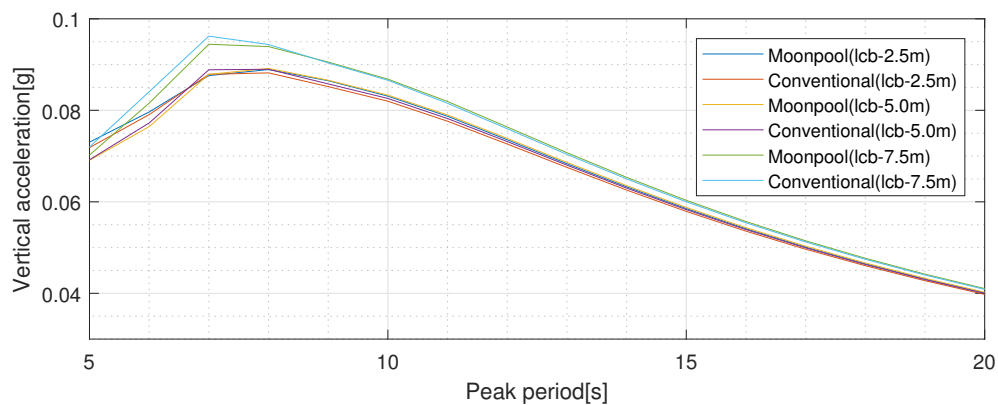


Figure 4.10: Comparison between conventional ship and ship with moonpool for positions aft of LCB

Figure 4.11 shows the comparison between the longitudinal positions for moonpool from 9.3 *m* aft of LCB to 7.5 *m* forward of LCB at different peak periods.

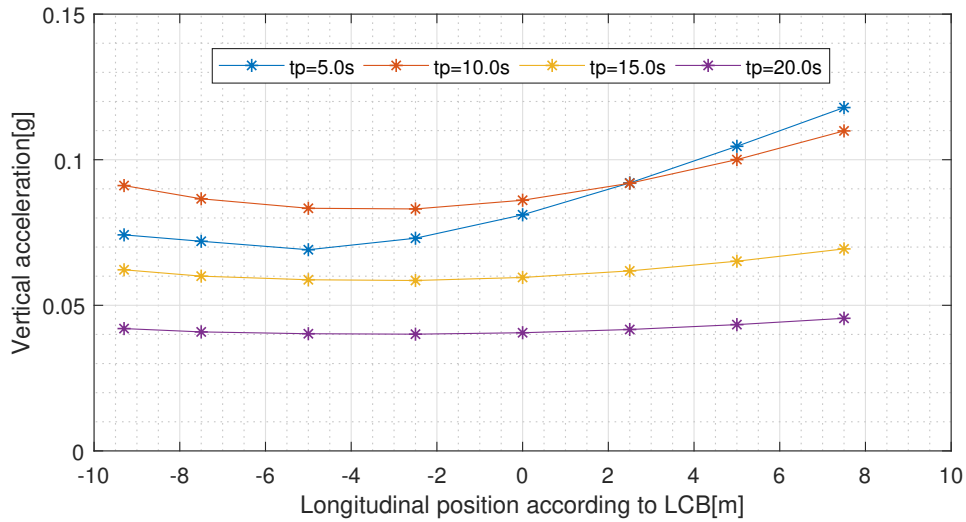


Figure 4.11: Longitudinal position comparisons at different peak periods

The same plot as above with all peak periods, can be found in Appendix A, together with the polar plots for each longitudinal position and wave heading which was not included earlier.

Chapter 5

Moonpool Shape Study

This chapter describes the moonpool shape study with applicable theory, methodology, and results. This chapter intends to solve research question 2. described in the introduction where the aim is to find a shape on moonpool which allows for more circulation of the water, to avoid an accumulation of dirty water inside the moonpool.

5.1 Method

The method of the moonpool shape study was divided into two parts. The first parts consider the whole ship without a moonpool, where the flow field underneath the vessel was in focus. The purpose behind this was to investigate and validate that the flow field underneath the vessel is uniform, which can allow for a reduction of the control volume to only consider the area around the moonpool.

The next part was to apply a variation of moonpool shapes in the limited control volume, and investigate what shape that leads to the least accumulation of dirty water inside the moonpool. These simulations were carried out using Star-CCM+, and the workflow is illustrated in the following flowchart where the method is outlined.

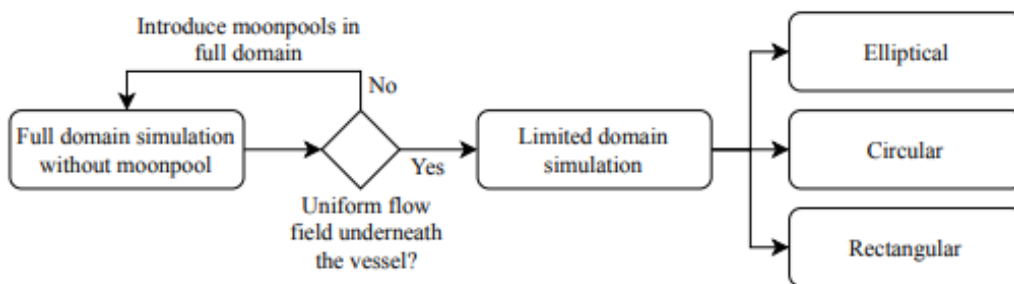


Figure 5.1: Moonpool shape study flowchart

The different shapes of the moonpools could possibly lead to more or less resistance on the hull, but this was not a subject of investigation in this thesis, but it was on the other hand,

used as a convergence criterion for the full domain simulation. It is also important to mention phenomena like sloshing and piston mode, which can occur in moonpools. These phenomena will most likely not occur, since these simulations are carried out at low speed in still water with a ship without any degree of freedom.

The loading condition for the vessel used for the vessel was the same as specified in the previous chapter(Section 4.2).

5.1.1 Star-CCM+

Star-CCM+ is a multidisciplinary simulation software developed by CD-Adapco, now owned by Siemens. Star-CCM+ provides an object-oriented platform for simulating physical problems like fluid dynamics, aero-acoustic, etc. The software provides an easy to use interface in order to make it easy to use for both experienced users, as well as newcomers to CFD.

5.1.2 Computational setup

The simulations are carried out on a virtual client provided by NTNU. The virtual client had the following specifications:

Table 5.1: Virtual client specifications

Component	Description
Processor	2x Intel Xeon(R) CPU E5-2690 v4 @ 2.60GHz, 8 Core(s)
Memory	3x 6 GB

5.2 Full domain simulation

A double body approach was used for the full domain simulation, were a symmetry boundary condition was applied on the free surface. This was done because the intention is not to analyze the resistance or the generated wave pattern, and this would just make the simulation very computational power demanding. To resolve the waves on the free surface, a minimum of 10 – 20 cells per wave height is recommended in Star-CCM+.

A very simplified way to estimate the bow wave height could be done by solving Bernoulli's equation for the incoming flow and the stagnation point at the bow of the vessel, to justify the simplification of the free surface.

$$\frac{1}{2}\rho V^2 = \rho g h \quad \rightarrow \quad h = \frac{\frac{1}{2}V^2}{g} \quad (5.1)$$

For a vessel speed(V) of 3 knots, the resulting pressure build-up is equal to a water column of 0.13 m. A free surface refinement to capture a small wave like the one above would have been

very computationally demanding, and would probably at the same time have a minimal effect for the flow field underneath the vessel.

5.2.1 Domain

The size of the domain determines how large the surrounding volume of the object is to be included in the simulation. This volume has to be sufficiently large, but at the same time as small as possible to limit the computational power and simulation time. If a domain is too small, it can cause fatal errors due to reflections, impact on flow, etc. For these full domain simulations, the domain size was set to the following dimensions, where the origin is set to the intersection point between the aft perpendicular and the waterline, illustrated in Figure 5.2.

$$\begin{bmatrix} x \\ y \\ x \end{bmatrix} \rightarrow \begin{bmatrix} -3.0 L_{PP} & 2.0 L_{PP} \\ 0.0 L_{PP} & 1.5 L_{PP} \\ 0.0 L_{PP} & -1.0 L_{PP} \end{bmatrix} \rightarrow \begin{bmatrix} -171.0 m & 114.0 m \\ -0.0 m & 85.5 m \\ 0.0 m & -57.0 m \end{bmatrix}$$

The full domain case without moonpool was cut in half due to symmetry along the x-axis. The different conditions applied to the boundaries are explained in the following section.

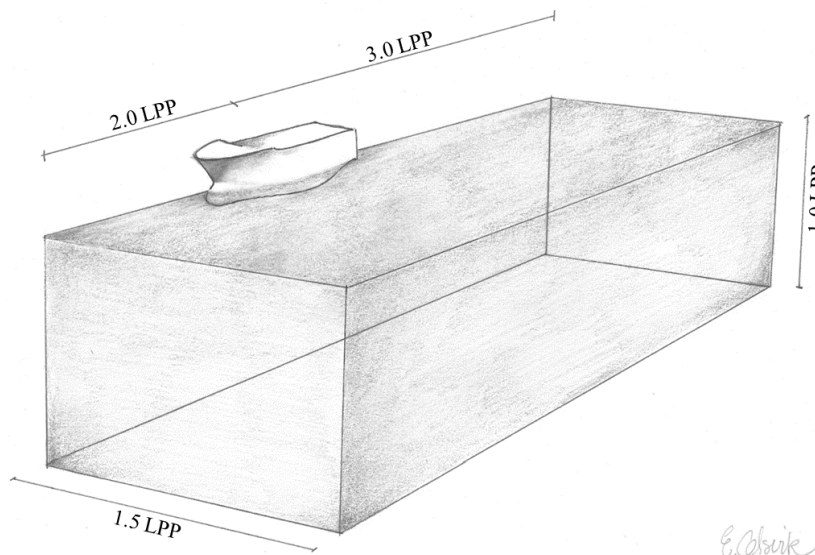


Figure 5.2: Double body domain dimensions(Evy Olsvik)

5.2.2 Boundaries

The boundary condition applied to the faces of the domain is specified in Table 5.2.

Table 5.2: Full domain boundary condition specifications

Face	Boundary Condition
Inlet	Velocity inlet
Outlet	Pressure outlet
Bottom	Symmetry plane
Water plane	Symmetry plane
Symmetry	Symmetry plane
Hull	Wall(no-slip)
Side	Symmetry plane

5.2.3 Mesh

Base mesh settings

The base mesh settings are the governing values for the mesh, unless otherwise specified in the regions. This involves base size, prism layer settings, surface grow rate and allowable maximum and minimum cell size. The base cell size can be found in the mesh convergence study in subsection 5.2.4.

Table 5.3: Full domain base mesh settings

Parameter	Value	Unit
Target surface size	6.25	%
Minimum surface size	3.125	%
Surface grow rate	130	%
Number of prism layers	6	<i>pcs</i>
Prism layer near wall thickness	0.0017	<i>m</i>
Prism layer total thickness	0.025	<i>m</i>
Volume grow rate	Slow	-
Maximum cell size	400	%

Surface control

Surface control enables you to control the mesh on a given surface, Target surface size, surface proximity and growth rate are only some of the parameter which can be specified to refine the mesh in areas of interest.

Two different surface controls were added to the full domain simulation of the hull. A surface control with the base mesh settings was added to the hull surface, to ensure that the prism layer setting was applied in a sufficient manner. This was done due to the observation of areas on the hull close to the symmetry free surface had very high y^+ values. The resulting boundary value of the dimensionless y^+ on the surface of the hull, can be found in Appendix C.

The second surface control was also applied to the boundaries of the domain, to make the mesh coarse in the areas in the far distance from the hull to make the simulation setup less computational demanding. This was done by disabling the prism layer on the surface and defining a target surface size of 400% of base size.

Volumetric control

Volumetric control gives the opportunity to customize the base mesh settings within a given volume, and is an efficient way to make refinements in areas of interest. Table 5.4 describes the anisotropic cell sizes for the volumetric refinement zones that was defined in the domain, The grow ratio between two refinement volumes can not be higher than a 2. Star-CCM+ will automatically generate new refinement zones if the grow ratio exceeds 2, and this could lead to unwanted refinements and a inefficient grid.

An aspect ratio of 2 is applied to the mesh in the flow direction of the fluid, to make the grid more computational efficient with regards to the cell count. The refinements zones for the limited domain simulation is illustrated in Appendix B.

Table 5.4: Full domain refinement zones

Refinement Zone	Appendix Figure	Percentage of base		
		X	Y	Z
Hull XXL	B.1	400%	200%	200%
Hull XL	B.2	200%	100%	100%
Hull L	B.3	100%	50%	50%
Hull M	B.4	50%	25%	25%
Hull S	B.5	25%	25%	25%
Hull XS	B.6	25%	12.5%	12.5%
Bow & Stern	B.7	12.5%	6.25%	6.25%

The *Hull XS* volume refinement zone was made by magnifying the hull geometry by 1.1, and proved sufficient to smooth out the grid size transition from the hull and to ensure a uniform mesh refinement over the hull surface.

5.2.4 Convergence study

There are several ways of conduction a mesh sensitivity analysis in CFD. One of the ways of performing a mesh convergence study is by changing both the mesh size and the time step simultaneously. Another way is to change one of the variables at a time. Since this is a steady case, no time step is needed, and the only variable is the mesh size.

The mesh convergence study done in this case was performed by approximately doubling the cell count for each step. This was done by varying the base mesh size, and the results are presented in the following table:

Table 5.5: Full domain mesh convergence study

Base Size	Cell Count	Resistance
m	pcs	N
2.00	458 489	3528
1.60	773 045	3460
1.25	1382 644	3390
1.00	2371 584	3390

The results are presented in Figure 5.3 to clearly show how the resistance curve decreases with the increasing cell count towards convergence.

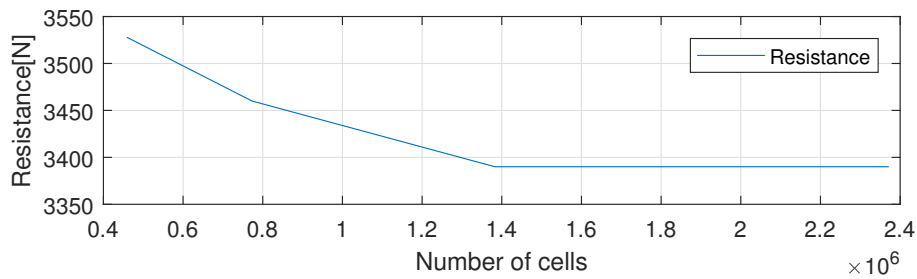


Figure 5.3: Full domain mesh convergence study

Both the residuals and the resistance were used as convergence criteria but there is not any available resistance data for the hull in questioning, and the speed of 3 knots is at the same time not representative with respect to experimental data. The resistance was however used to see if the full domain simulation converged. The residuals were interpreted as converged for the steady case when the residual had dropped by 3 – 4 orders of magnitude, according to ITTC - Recommended Procedures and Guidelines (2011). The resulting mesh for a base size of 1.25 m is illustrated in Figure 5.4 and 5.5.

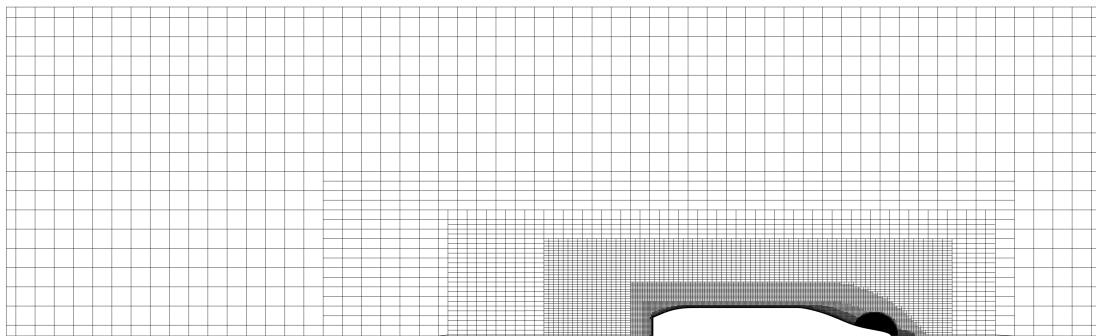


Figure 5.4: Top view of full domain mesh with base cell size of 1.25 m

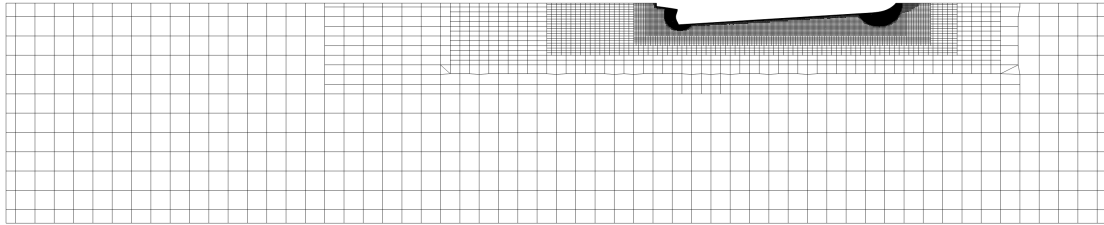


Figure 5.5: Side view of full domain mesh with base cell size of 1.25 m

5.2.5 Result

The fluid flow path and velocity are illustrated in Figure 5.6 and 5.7 with the use of streamlines. The streamlines show the varying flow velocity by the change of color, and the velocity scale is illustrated at the bottom of Figure 5.7.

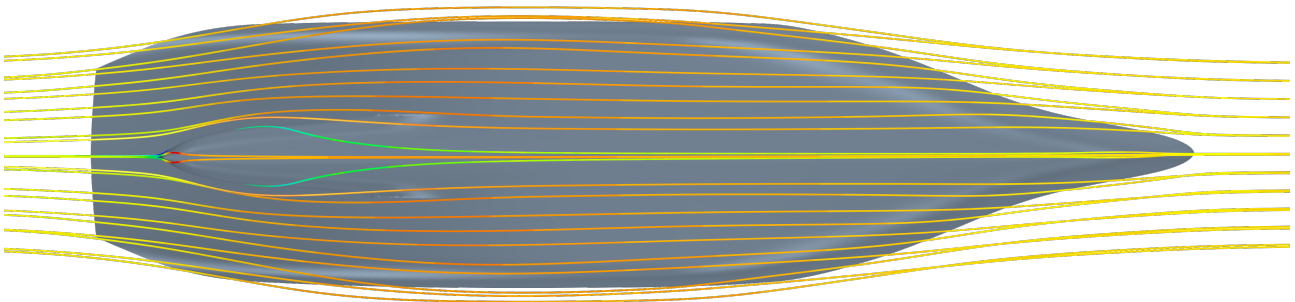


Figure 5.6: Bottom view of hull with streamlines

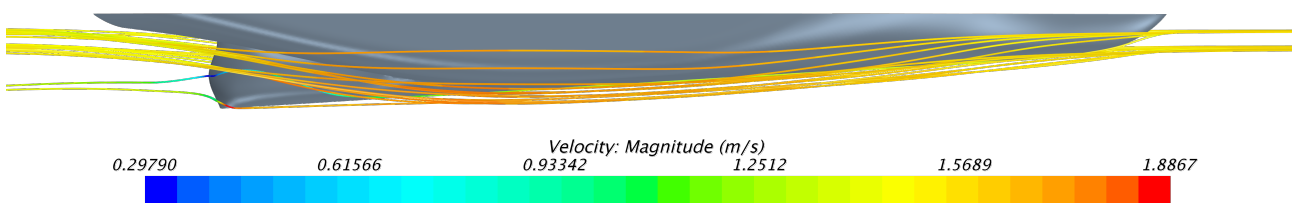


Figure 5.7: Side view of hull with streamlines

5.3 Limited domain simulation

The limited domain gave the possibility for further refinement of the areas of interest around the moonpool, and reduce the computational effort. This can be done based on the result found in the previous section, further elaborated in the discussion found in the succeeding chapter.

The cross-sectional shape of the moonpool pipe used today is normally circular. This shape was tested to compare it with the two other shapes, to investigate if there was a difference in an accumulation of dirty water inside the moonpool. The setup of the simulations was developed on the circular shape, and then applied to the elliptical and rectangular shape simulations.

To be able to differentiate between the three different shapes in questioning, the passive scalar function has been used. The passive scalar function gives the possibility to distinguish between "clean" and "dirty" fluid, where the clean fluid was given the value 1, and the dirty fluid was given the value 0. This was solved over the whole domain using the transport equation for passive scalar described in subsection 3.2.10.

The exchange rate of dirty water was found by filtering out the mass flux of the clean passive scalar at the outlet boundary. The exchange rate was then found by dividing the outlet mass flux with the inlet mass flux, expressed as follows:

$$\text{Exchange rate} = \frac{\text{Outlet passive scalar mass flux}}{\text{Inlet passive scalar mass flux}} \cdot 100 \quad (5.2)$$

This gave a percentage ratio of how much dirty water the flow underneath the vessel was able to clean out of the moonpool. This was again multiplied with the total mass flux, and divided by the density, to give the results in volumetric flow. The procedure of obtaining the passive scalar mass flux for Star-CCM+ is briefly described in Appendix F.

5.3.1 Domain

The size of the limited domain was set to simulate the flow within the moonpool and the wake of the moonpool. The domain had the following dimensions, where the reference point is set to the center of the moonpool at the free surface:

$$\begin{bmatrix} x \\ y \\ z \end{bmatrix} \rightarrow \begin{bmatrix} 5.0 \text{ m} & -16.0 \text{ m} \\ 6.0 \text{ m} & -6.0 \text{ m} \\ 12.0 \text{ m} & -25.0 \text{ m} \end{bmatrix}$$

The inlet was set approximately 5.0 m in front of the edge of the moonpool, to let the flow field develop. The outlet was at the same time set far behind the moonpool to capture the wake and avoid errors like the reverse flow at the outlet boundary. The width of the tank was set according to the bilge radius of the vessel.

A large volume on top of the moonpool was defined to not simulate the moonpool room as tight, to avoid a pressure build-up in the moonpool. A pressure build-up could have a significant impact on the free surface. Figure 5.8 is a screen capture of the limited domain with the rectangular moonpool and the free surface.

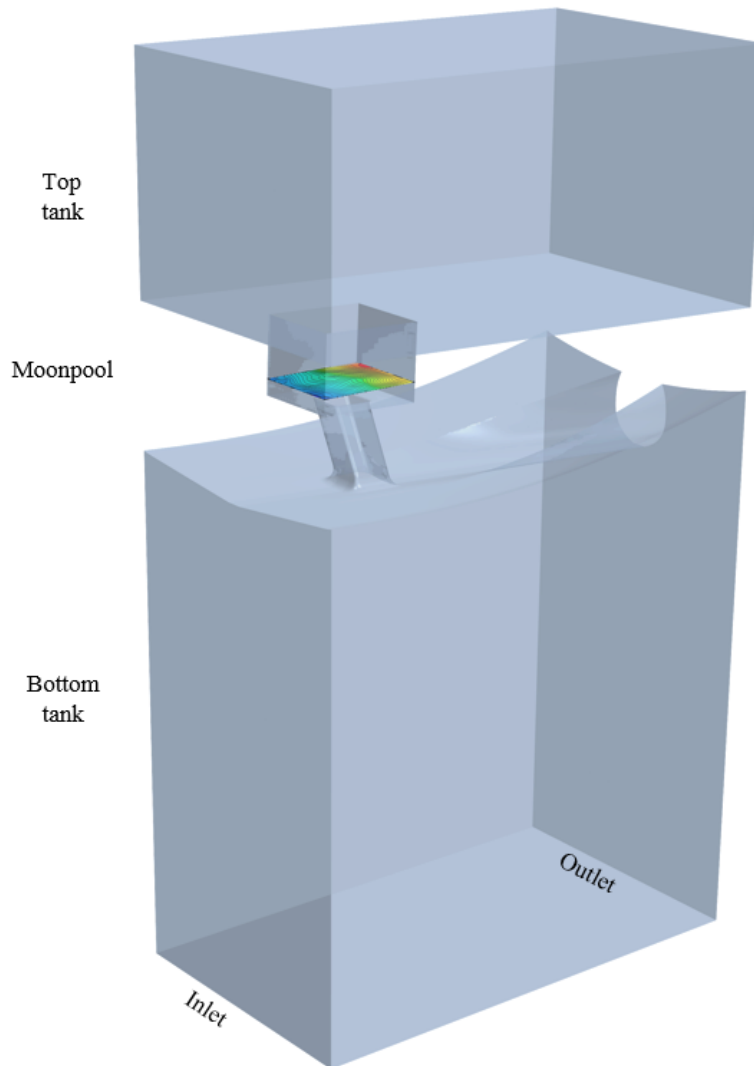


Figure 5.8: Limited domain with rectangular moonpool

5.3.2 Geometry

Three different shapes were subjects of testing: circular, elliptical, and rectangular. The width of the moonpool in the transverse direction was set at a fixed value of 1500 mm , for practical reasons. These practical reasons are related to maneuvering the vessel over the longline, and getting the fish and longline through the moonpool. The three shape variation is illustrated in Figure 5.9, with associated dimensions for both the width and the length. Keep in mind that the pipe has an inclination of 20° from the vertical line.

The entrance to the moonpool underneath the vessel has a fixed radius of 500 mm according to previous vessels designed by MT. It is important that this radius is not too sharp because this can apply unwanted wear and tear on the longline gear since the longline is guided into the moonpool on these radii. The radius between the moonpool pipe and the upper basin is set fixed to 150 mm for the same reasoning. The side view of the moonpool is illustrated in Figure 5.9, where the main deck and the rail-roll point is also illustrated.

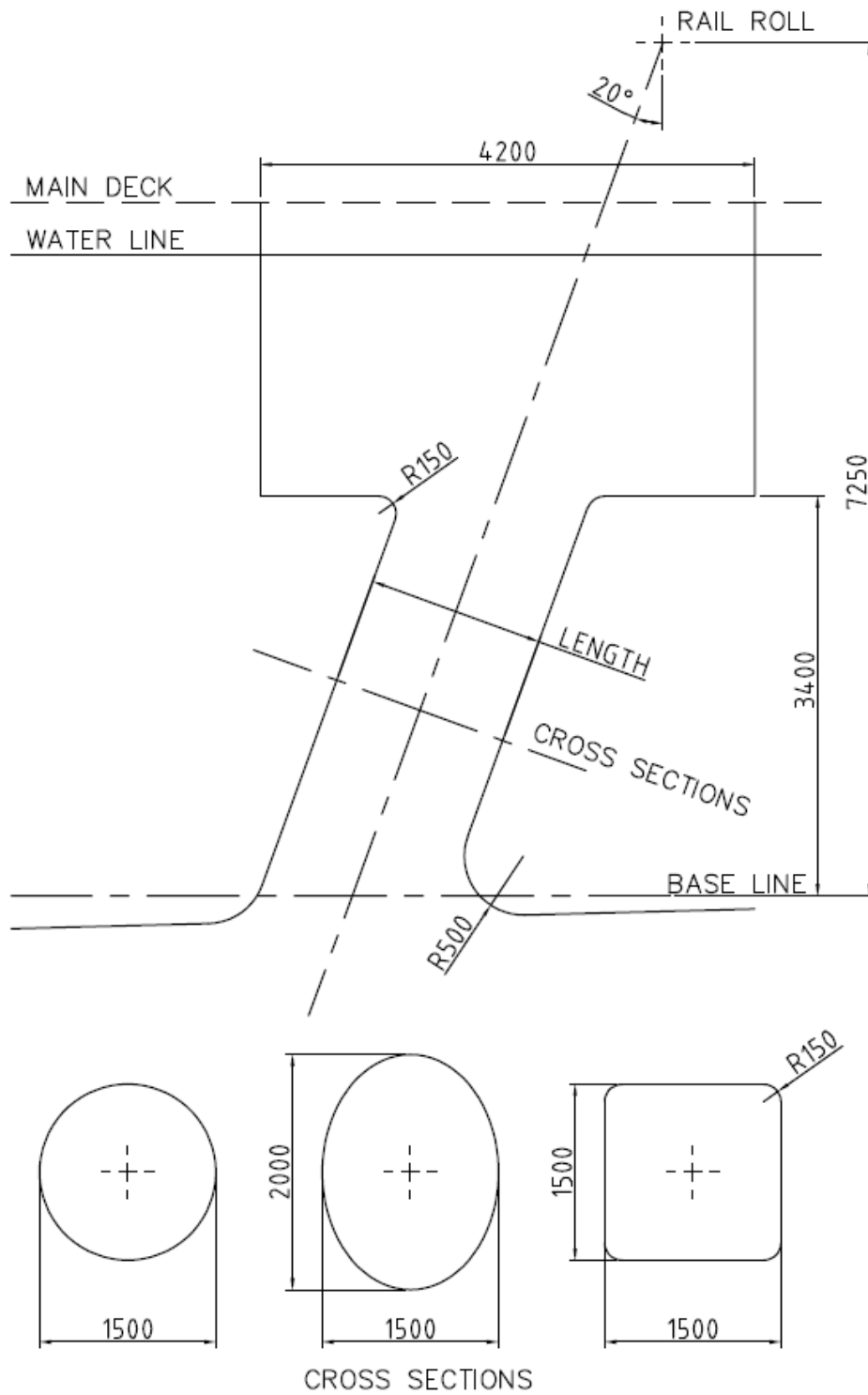


Figure 5.9: Moonpool side view and cross-sectional shapes

5.3.3 Boundaries

The boundary condition applied to the faces of the limited domain simulations is defined in Table 5.6. The symmetry plane condition was applied to the upper part of the limited domain, to resemble a large tank. The bottom boundary was assigned a velocity inlet condition, where the velocity was specified in the water current direction. The physical meaning of this is to be interpreted as the vessel is operating in water with infinite depth.

Table 5.6: Limited domain boundary condition specifications

Face	Boundary Condition
Inlet bottom	Velocity inlet
Inlet top	Symmetry plane
Outlet bottom	Pressure outlet
Outlet top	Symmetry plane
Bottom	Velocity inlet
Top	Symmetry plane
Hull	Wall(no-slip)
Side bottom	Symmetry plane
Side top	Symmetry plane

5.3.4 Mesh

The mesh for the limited domain simulating was set up according to the parameters specified in this section.

Base mesh settings

The base mesh setting was set as described in Table 5.7, and some of the values are discussed following the table.

Table 5.7: Full domain base mesh settings

Parameter	Value	Unit
Base cell size	0.75	<i>m</i>
Target surface size	12.5	%
Minimum surface size	3.125	%
Surface grow rate	130	%
Number of prism layers	6	<i>pcs</i>
Prism layer near wall thickness	0.0017	<i>m</i>
Prism layer total thickness	0.025	<i>m</i>
Volume grow rate	Slow	-
Maximum cell size	1000	%
Mesh alignment position	[23.5,0.0,0.0]	[<i>x, y, z</i>]

The trimmed cell mesher enables the function to carry out a mesh alignment. This was specified in the middle of the moonpool at the free surface, to make a symmetric mesh with a sharp transition between the two fluids at the free surface.

No mesh sensitivity study was carried out on the limited domain simulations due to the mesh size inside the moonpool pipe had to strongly correlate with the prism layer applied to the surface of the hull and moonpool, and a more trial and error approach was used. This was to get a smooth transition from the near wall mesh to the coarser volume mesh and obtain a reasonable amount of cells. The circular, elliptical and rectangular had an total cell count of: 1 424 051 cells, 1 439 781 cells, and 1 399 592 cells, respectively.

The resulting boundary values for the y^+ can be seen in Figure E.4, illustrated on the case with the circular moonpool pipe.

Surface control

Surface control was added to the tank boundaries the same way as in the full domain simulation, where the surface target size and the minimum surface size was specified to the same value of 500% of the base. The prism layer was also disabled.

Volumetric control

The volumetric control was set up to capture the flow around sharp gradients and to capturing the fine changes at the free surface, to ensure that the waves inside the moonpool were developed in a proper way. Special attention has to put in making a well refined free surface, as mentioned in section 5.2, This was done by making three volumetric refinements zone around the free surface with gradually decreasing cell height.

The different volume refinements zones are specified in Table 5.8, and is illustrated in Appendix D.

Table 5.8: Limited domain refinement zones

Refinement Zone	Appendix Figure	Percentage of base		
		X	Y	Z
Free surface L	D.1	50%	50%	25%
Free surface M	D.2	25%	25%	12.5%
Free surface S	D.3	12.5%	12.5%	6.25%
Pipe L	D.4	50%	50%	50%
Pipe M	D.5	25%	25%	25%
Pipe S	D.6	12.5%	12.5%	12.5%

The resulting mesh generated by Star-CCM+ is illustrated in Figure 5.10 and Figure 5.11.

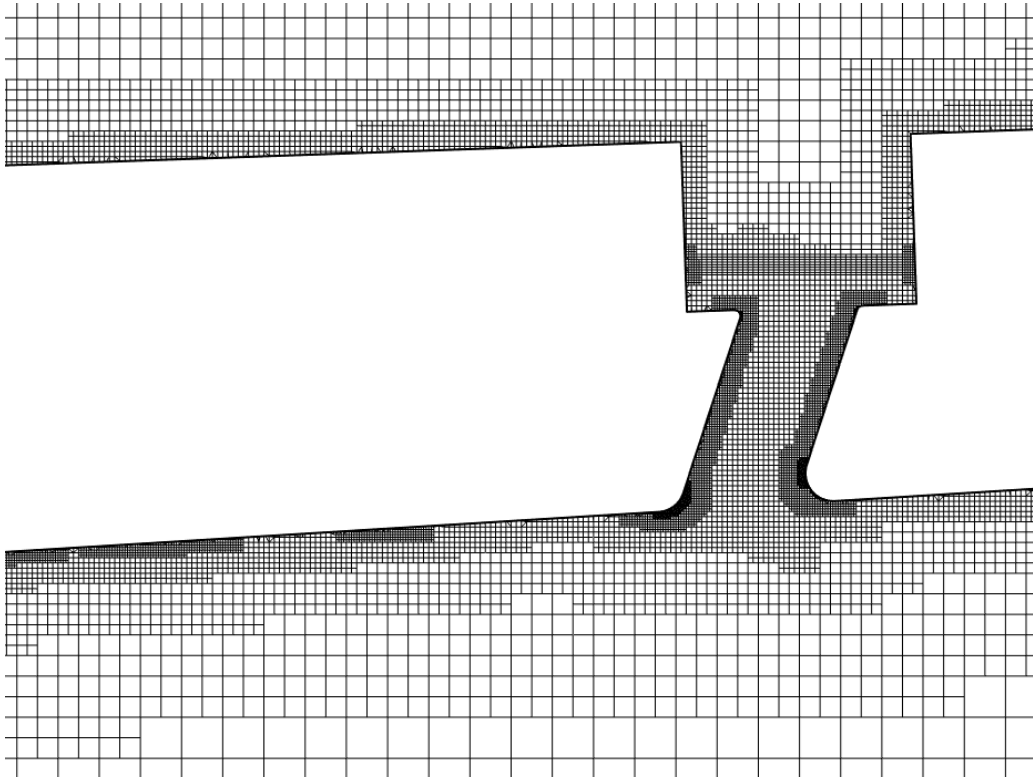


Figure 5.10: Limited domain mesh with base cell size of $0.75m$

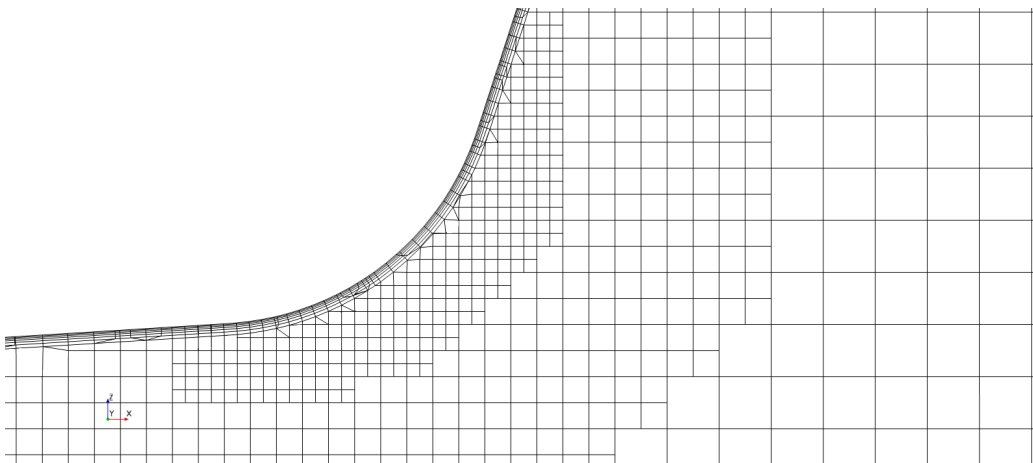


Figure 5.11: Moonpool pipe refinement with base cell size of $0.75m$

5.3.5 Initial conditions and solver settings

The fluid flow in the bottom part of the domain was initiated with the use of a flat VOF wave, where the water current was specified to $1.6 m/s$, equivalent to $3 knots$. This gave the opportunity to specify the velocity in the x-direction for both the inlet and the bottom of the domain which forms the basis for the assumption of infinite water depth mentioned in the boundary conditions for the limited domain simulations.

The initial turbulence setting for the $k - \epsilon$ -model was set to $0.0001 m^2/s^3$ for the turbulent dissipation rate, and the turbulent kinetic energy rate was set to $0.00001 J/kg$, based on recommended values found on the Steve portal for VOF simulations(Star-CCM+ 2018).

A time step of $0.1 s$ was used of the limited domain simulation and was proven to be sufficiently low together with a maximum number of 10 inner iterations. This high time step is further debated in the discussion.

5.3.6 Results

The two following graphs show the volume flow of dirty water calculated by the use of passive scalars for a simulation duration of $40.0 s$. Figure 5.12 shows the full simulation of $40.0 s$, and Figure 5.13 show the volume flow rate for a limited duration of $1.0 s$ at the end of the simulation.

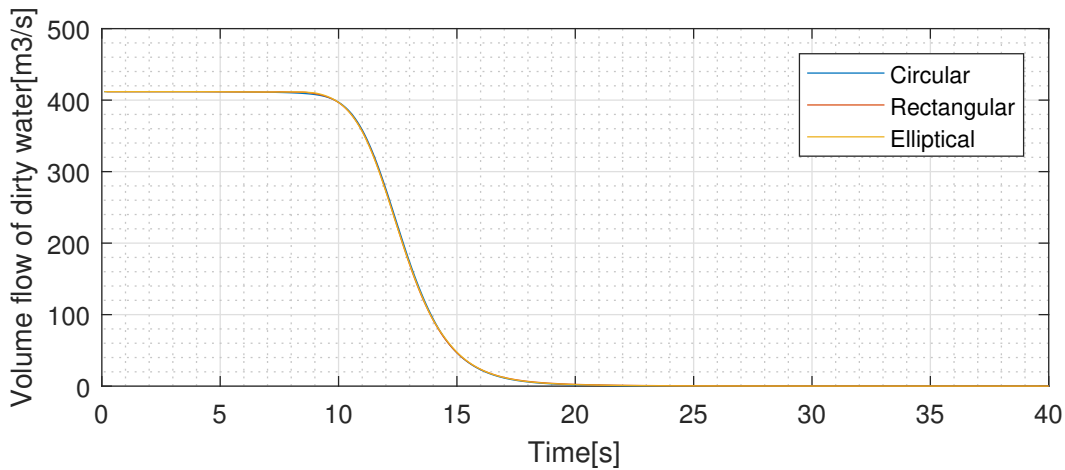


Figure 5.12: Volume flow of dirty water(0.0 – 40.0 s)

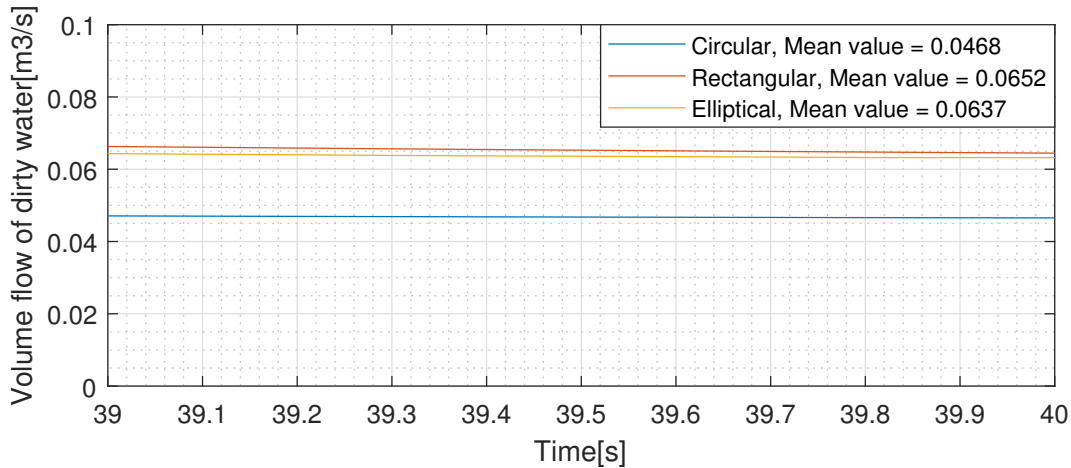


Figure 5.13: Volume flow of dirty water(39.0 – 40.0 s)

The three following figures show the 2-dimensional passive scalar distribution for the midplane of the limited domain, at the end of the 40.0 s simulations. The blue passive scalar presents the dirty water, and the red passive scalar represents the clean water. These simulations were only run for 40.0 s because the passive scalar function is not able to distinguish between multiple phases, and the simulation was therefore stopped before the passive scalar could enter the air. The full simulation of the passive scalar for the three different shapes is illustrated Appendix G.

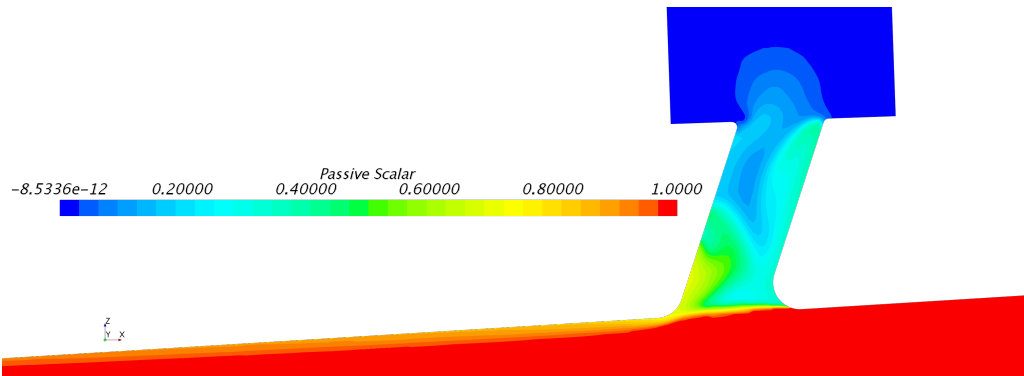


Figure 5.14: Passive scalar field for circular shaped moonpool pipe, at time step 40.0 s

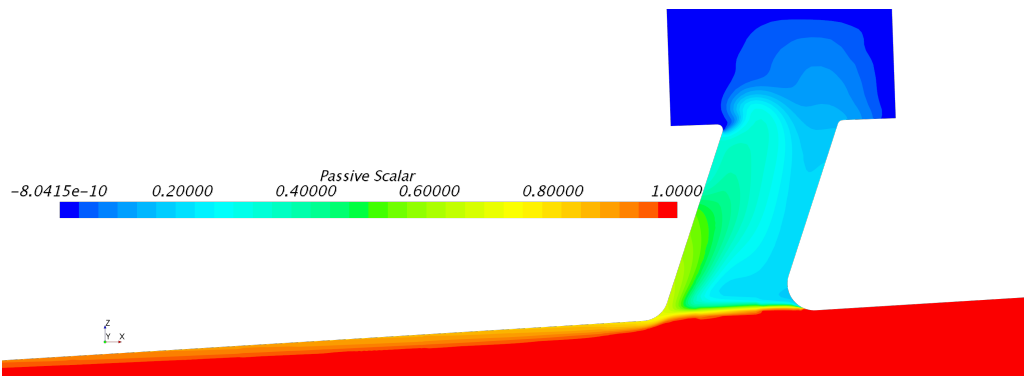


Figure 5.15: Passive scalar field for elliptical shaped moonpool pipe, at time step 40.0 s)

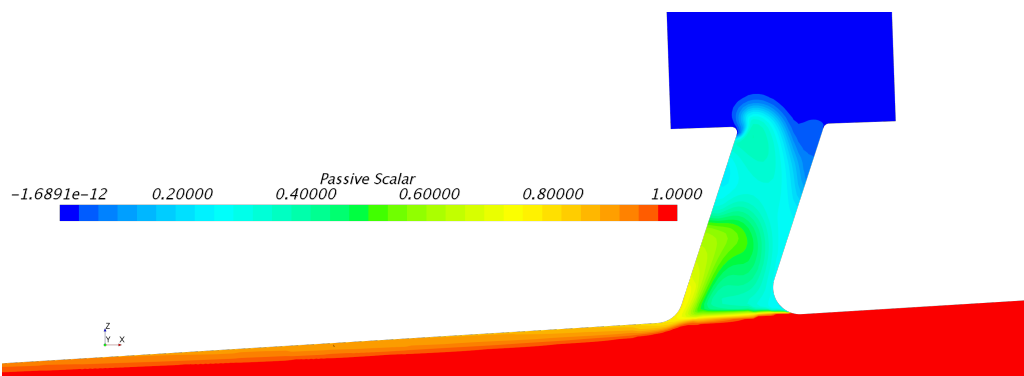


Figure 5.16: Passive scalar field for rectangular shaped moonpool pipe, at time step 40.0 s

Figure 5.17a, 5.17b, and 5.17c shows the passive scalar blend in a cross section of the pipe right above the entrance radius to the moonpool pipe, at the same time step as the illustrations above(40.0 s).

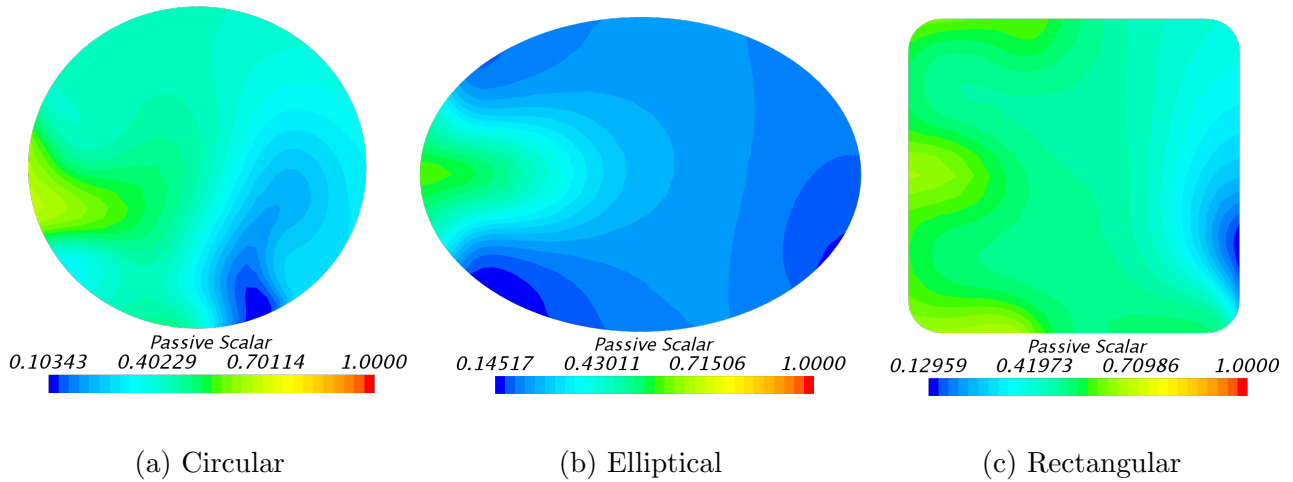


Figure 5.17: Passive scalar blend in moonpool pipe cross section, at time step 40.0 s

A vector plot showing the velocity and direction of the fluid for the same time step could be found in Appendix H, to illustrate how the fluid flows underneath the vessel and interact with the fluid in the moonpool pipe.

Chapter 6

Discussion and Future Work

6.1 Discussion

6.1.1 Moonpool position study

By looking at the polar plots presented in the moonpool positions study, it can be seen that the longitudinal positions of the moonpool and rail-roll is not that sensitive to beam and following seas. The longitudinal positions do on the other hand seem to be most sensitive to head seas, and this was therefore investigated further.

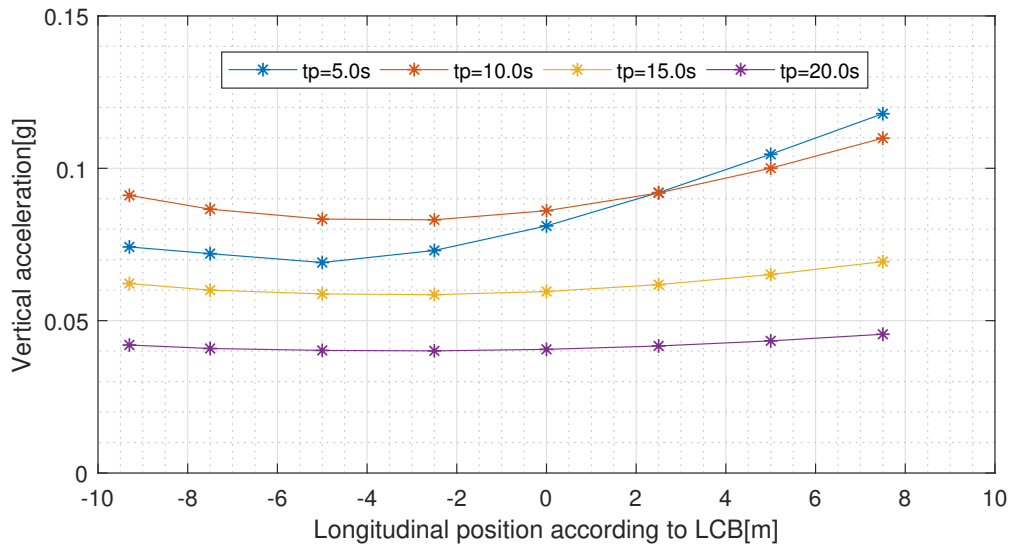


Figure 6.1: Longitudinal position comparisons at different peak periods ($H_s = 3.5 m$)

Figure 4.1 is the same figure as presented in the moonpool position results. The ideal position of the moonpool looks to be around 5.0 m aft of LCB for the MT1114 hull, based on the presented results. It was expected that the ideal position of the moonpool with respect to vertical acceleration was aft of the longitudinal center of buoyancy. The plots in Figure 6.1

show that the magnitude of the vertical acceleration is at its lowest for the moonpool position 5.0 m aft of LCB. This observation is more clear for the sea states with the lowest peak periods.

The results from the moonpool position study are, however somewhat questionable, as there are reasons to believe that the results do not represent the real world response of the vessel. The moonpool was expected to have a significant effect on the ship motion due to its configuration with the small pipe leading to a large basin, as presented in Figure 4.10. This effect is neglected by the software, due to the fact that it does not take the dynamic effects of the moonpool into account.

2D strip theory does also have its limitation, especially for a small ship with much curvature like the longline vessel investigated in this thesis. The length-breadth ration is within the limit($L/B > 3$), but there are still reasons to believe that there are some important three-dimensional effects on the hull which is not captured in the analysis. This is also argued for in the user manual for VERES(Fathi 2018). Although the results are somewhat unclear, they can be used as a guideline for more extensive testing outlined in future work.

6.1.2 Moonpool shape study

Full domain simulation

To limit the computational domain for the moonpool shape assessment, a double body simulation was carried out to verify that the velocity field at the bottom of the vessel is uniformly distributed. The flow field was visualized with the use of streamlines, and the streamlines illustrate the velocity and flow path of the fluid flow is evenly distributed. The simulation shows that the velocity field underneath the vessel has an acceptable uniformity and that the velocity of the fluid flow is lower in the boundary layer. The interpreting of this result is that it is possible to do a limited domain simulation, due to the low vessel speed and that calm water is assumed.

On the other hand, it could have been of interest to do a full domain simulation with moonpool to see if the overall flow pattern changes, but was argued to be to computational demanding as mentioned in section 5.2.

Limited domain simulation

The three different moonpool pipe shapes were simulated in the limited domain for a duration of 120.0 s, but the passive scalar transport is only valid for the early phase(40.0 s) of the simulation because the water starts to diffuse into in the air. This is due to the properties of passive scalar transport and how it is defined. There was no easy solution to this problem, and the developers of Star-CCM+ claimed that passive scalar transport would not be able to satisfy the law of conservation if the model distinguished between two different fluid phases in a multi-phase flow(Star-CCM+ 2018).

The results for the early phase of the simulation could nevertheless give an idea of which of the different shapes would contribute to more circulation of the dirty water. The graphical

presentation of the passive scalar field in the midplane of the limited domain illustrates the mixture between the clean and dirty fluid.

The elliptical shape looks to have cleaned out most water after 40.0 s, even though it looks dirty at the pipe cross section illustration. This is due to a stream of dirty water flowing down the pipe, at the location of the cross section. The elliptical shape looks to have generated a swirl in the moonpool pipe which has led clean fluid into the moonpool basin.

The rectangular shape does, however, look to have a more dense mixture of clean water in the pipe section, but the clean fluid have not dispersed into the moonpool basin as much as the other shapes. The rectangular shape looks to push the clean water up the back side of the moonpool pipe by looking at the passive scalar flow in the rectangular moonpool presented in Appendix G, rather than generating a swirl like the elliptical and circular shape.

The circular shape looks to have generated a swirl the same way as the elliptical shape, but the magnitude of this swirl seems to be weaker in comparison with the elliptical. It does also look like the circular shape does not lead as much clean water into the moonpool as the elliptical.

A method of filtering the passive scalar at the inlet and outlet boundaries was developed to not only base the results on colorful plots. The result presented by the filtering the clean and dirty passive scalar illustrated Figure 5.13 suggests that the rectangular and elliptical shaped moonpool pipes would contribute to less accumulation of dirty water inside the moonpool, with a mean volume flow of dirty passive scalar at 65.2 l/s and 63.7 l/s, respectively. The cross-sectional area can, on the other hand, be one of the reasons why there is a significant deviation of approximately 25% between the circular shape and the other shapes. The rectangular and elliptical shaped cross sections are significantly larger than the circular shape, due to the breath of the moonpool is kept constant for practical reasons.

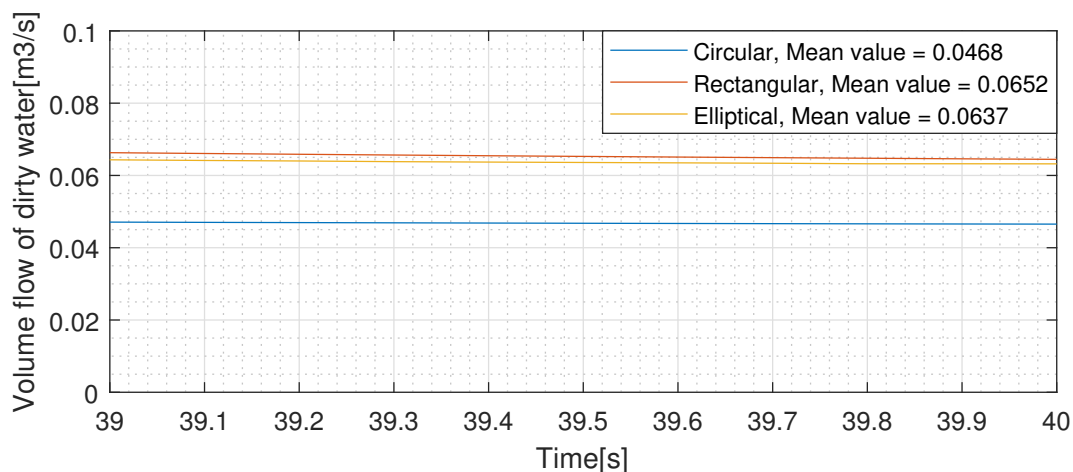


Figure 6.2: Volume flow of dirty water(30.0 – 40.0 s)

There could, however, be some sources of error in the obtained results. A source of error could be that the passive scalar is not able to distinguish between water and air and that the flow underneath the vessel is, therefore, able to clean out more water than the moonpool actually contains. Another source of error could be that there are still residues of dirty passive scalar in the domain, although it looks to be clean.

The amount of available computational power has been a limiting factor in the investigations. Approximately 2800 core hours have been used in the simulations of the end results, excluding testing, convergence studies, and development for the final setups. A more powerful computational setup could have contributed to a more rapid development of the final setup, and given time for more extensive tests.

There has been a steep learning curve and some lessons learned during the development of the simulations, as expected for a newcomer to CFD. Choosing the right time step is crucial for getting a converged solution within a reasonable amount of time. During the development of the final setup for the limited domain simulation, a lot of effort was put in to get a CFL number around 0.4 over the whole domain. It turned out that this criterion only has to be fulfilled at the free surface, and that the use of the implicit unsteady integration scheme made the simulations stable with a high time step for the limited domain simulations. This was discovered during the time step ramp-up phase of a simulation, as the simulation started to converge after the free surface in the moonpool had calmed down after the initiation of the simulation. This finding was important for the progress during the final simulations.

The development of a full domain simulation with the free surface was also carried out before the discovery of the double body simulation was sufficient in this case. The knowledge gained during the development of this simulation contributed to a more rapid development of the method for the limited domain simulations, since it was based on the same approach to the setup of the simulation.

6.2 Future Work

The limitations presented in the previous discussion forms the basis of the future work presented in this section.

The dynamic effects of the moonpool were not taken into account in the moonpool position study. These effects are of interest due to it could contribute to either dampening or amplification of the vessel response. This effect is probably highly dependant on the position and shape of the moonpool. As a result of these shortcomings, a new approach was attempted in another software made by DNV GL, called Wasim. Wasim utilizes the Rankine panel method, which could have been more suited for the purpose, but the setup was proven to be too time-consuming due to the extensive geometry and surface preparation needed, especially for a wide range of moonpool positions. It was at the same time not certain that the Rankin panel method would give better results since it utilizes much of the same theory.

It could, at the same time, have been interesting and useful to generalize the results for the position of the central hauling pool, to make it applicable to other vessel dimensions. While this would require extensive testing of several vessels to find the correlating factors, and is therefore mentioned as future work.

Another topic of interest, is to study how the same vessel reacts when it is exposed to a wave spectrum with peak periods of a wave length ($\lambda = g/(2\pi)T^2$) corresponding to the full, half and quarter length of the vessel.

The shape study did only cover some simple shapes, and it could at the same time have been intriguing to see how an asymmetric shape could have behaved, or how a wedge in front of the moonpool could have contributed to more disturbance and circulation. Alternatively, try to find some other ways to guide the water flow to the top of the moonpool could have been interesting. This could for example, have been done by applying an inlet and a pipe to guide clean water to the top of the moonpool.

The best case scenario could be to combined both the moonpool position and shape assessment into one study carried out by simulations or model testing.

Chapter 7

Conclusive Summary

The benefits of the central hauling pool for longline fishing have now proven its benefits during twenty years of operations. Better working conditions for the fishermen and less loss of fish during the hauling process, are key factors that contribute to a safer and more efficient fishery for longline vessels, provided by the moonpool.

The position of the rail-roll and moonpool is sensitive to vertical accelerations, especially in head seas. This position has to be carefully selected to minimize the vertical acceleration on the longline and the captured fish. By the use of numerical vessel response estimation, it can be seen that the ideal position for the rail-roll and moonpool is around 5.0 m aft of the longitudinal center of buoyancy for the MT1114 hull. The results can despite the limitations of the 2D strip theory applied in the vessel response calculations be used as reference values for further analyses.

The shape of the moonpool pipe had an elliptical shape originally when the central hauling pool was introduced in the 90s, but changed toward a circular shape after it was discovered that the maneuvering over the longline was easier than first anticipated, and to save space at the same time. Some wanted effects were however lost in the transition from the elliptical shaped moonpool pipe to the circular shaped moonpool pipe, which was the ability to clean out dirty water during hauling.

The second objective of this research was to investigate three particular shapes to determine which shape would lead to less accumulation of dirty water inside the moonpool, by means of CFD. A case with a full-scale vessel without moonpool was simulated to validate that the flow field underneath the vessel was uniform during hauling speed at 3 knots, which formed the basis for limiting the domain to only concerning the area around the central hauling pool underneath the vessel. Circular, elliptical and rectangular shaped moonpool pipes were investigated, and a method with the use of passive scalar transport was developed to be able to track the ability to replace the dirty water inside the moonpool.

It is hard to draw a definite conclusion for the available results, and more extensive testing of the different shapes is therefore recommended. However, the current results show that the elliptical and rectangular moonpool shapes provide a better behavior of cleaning out dirty water.

Bibliography

- Bjordal, A. & Lokkeborg, S. (1996), 'Longlining'.
- Dezecot, C. & Eik, K. J. (2015), Barents East blocks Metocean Design Basis, Technical report, Statoil.
- Enerhaug, B. (2018), Personal communication, phone.
- Enerhaug, B. & Løland, G. (1998), 'European patent - Central Hauling Pool'.
- Faltinsen, O. M. (1990), 'Sea loads on ships and offshore structures'.
- Faltinsen, O. M. (2009), 'Sloshing'.
- Fathi, D. E. (2018), *ShipX Vessel Response(VERES) User's Manual*, SINTEF Ocean AS.
- Fathi, D. E. & Hoff, J. R. (2017), *ShipX Vessel Respons(VERES) Theory Manual*, SINTEF Ocean AS.
- Fiskerstrand, P. A. (2019), Personal communication, phone.
- Geographic, N. (2018), 'Can the Ocean Feed a Growing World?', Accessed: 22.11.18'.
URL: <https://www.nationalgeographic.com/environment/2018/08/news-fisheries-aquaculture-food-security/>
- ITTC - Recommended Procedures and Guidelines (2011), Practical Guidelines for Ship CFD, Technical report, The International Towing Tank Conference.
- Journée, J. M. J. (1992), 'Quick strip theory calculations in ship design', *PRADS'92 Conference on Practical Design of Ships and Mobile Structures* **1**, 5–12.
- Journée, J. & Massie, W. (2002), 'Offshore Hydromechanics', *Electrochimica Acta* .
- Karlsen, L. (1997), 'Redskapslære og fangstteknologi'.
- Larsen, R. B. (2010), 'Development of new hauling systems'.
- Moukalled, F., Mangani, L. & Darwish, M. (2016), *The Finite Volume Method in Computational Fluid Dynamics - An Advanced Introduction with OpenFOAM and Matlab*, Vol. 113, Springer.
- Orimolade, A. & Gudmestad, O. (2016), 'Wave spectra for weather restricted marine operations with emphasis on operations in the Barents Sea', *Proceedings of the International Offshore and Polar Engineering Conference* **1**.

- Ponnappan, S. & Sankunny, S. (2018), 'CFD simulation of the moonpool on the total resistance of a drillship', (4), 164–169.
- Salvesen, N., Tuck, E. & Faltinsen, O. (1970), 'Ship motions and sea loads', *Trans. SNAME* **78**(8), 250–287.
- Sandvik, E. (2016), Design optimization of offshore construction vessels, Technical report, Norwegian University of Science and Technology.
- Sintef (2004), "'Dragerbrønnen"- En revolusjon av linefisket!, Accessed: 18.11.18'.
URL: <https://www.sintef.no/globalassets/upload/fiskerioghavbruk/faktaark/dragerbronnno.pdf>
- Star-CCM+ (2018), 'Star-CCM+ documentation'.
URL: <https://documentation.thesteveportal.plm.automation.siemens.com>
- Svoren, N. O. (2015), Investigation of Hydrodynamic Performance of a Twin-Screw Trawler Using CFD, Technical report, Norwegian Univeristy of Science and Technology.

Appendix A

Moonpool position study results

The following plots shows the vertical acceleration at the rail expressed as g-force. The plots shows the response for every wave heading and for a peak period varying from 5 s to 20 s. The the significant wave height is fixed to $H_s = 3.5 m$

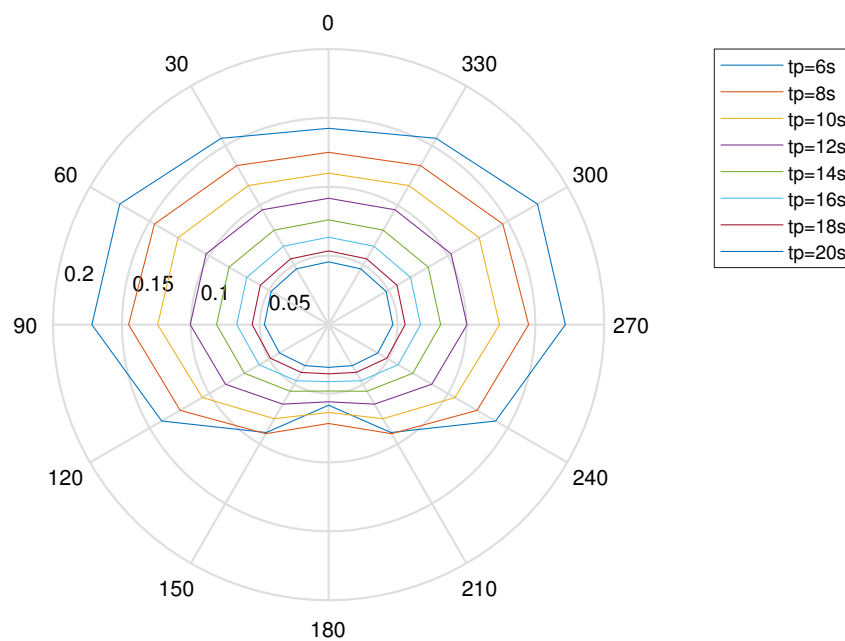


Figure A.1: Response at rail roll on vessel with moonpool placed 7.5 m forward of LCB[g]

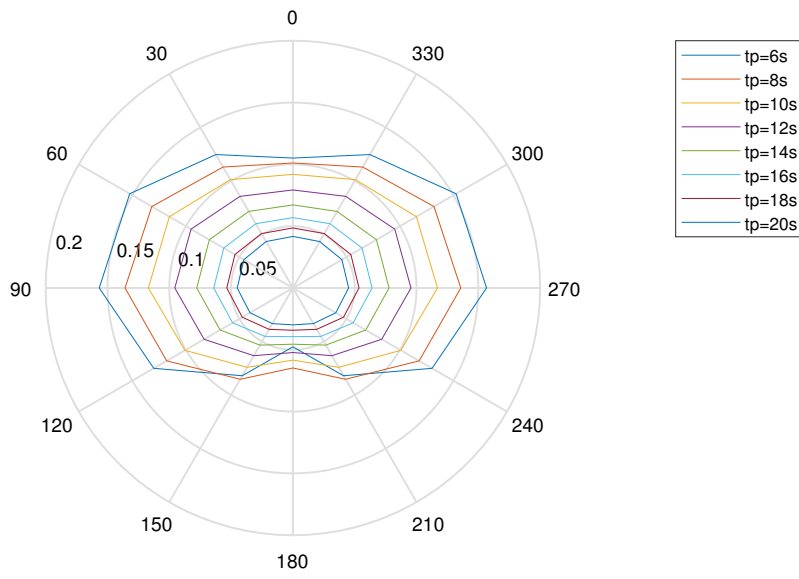


Figure A.2: Response at rail roll on vessel with moonpool placed 2.5 m forward of LCB [g]

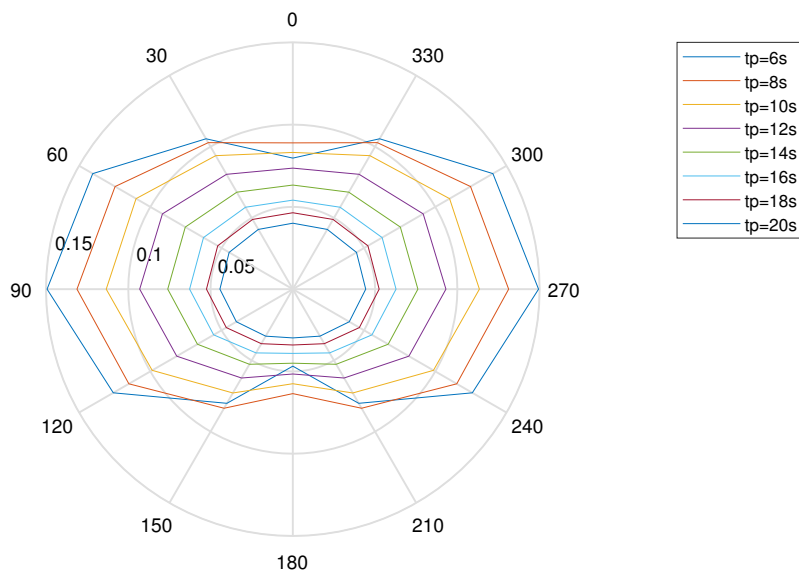


Figure A.3: Response at rail roll on vessel with moonpool placed 2.5 m aft of LCB [g]

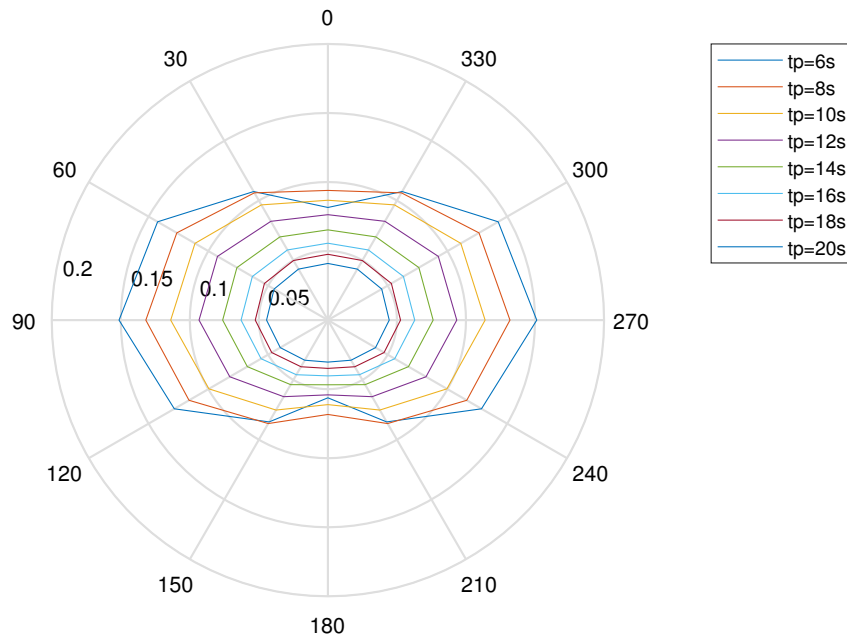


Figure A.4: Response at rail roll on vessel with moonpool placed 7.5 m aft of LCB[g]

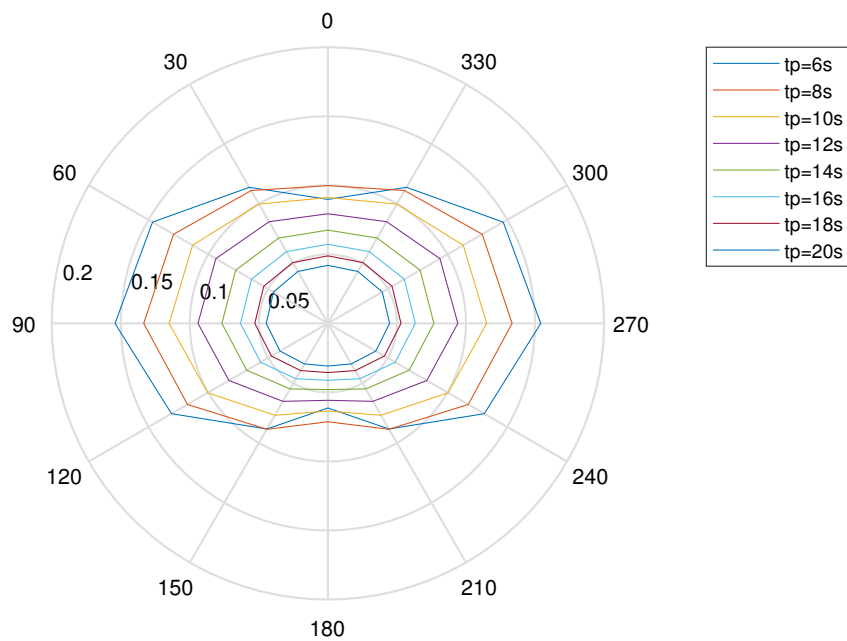


Figure A.5: Response at rail roll on vessel with moonpool placed at LCF, 9.23 m aft of LCB[g]

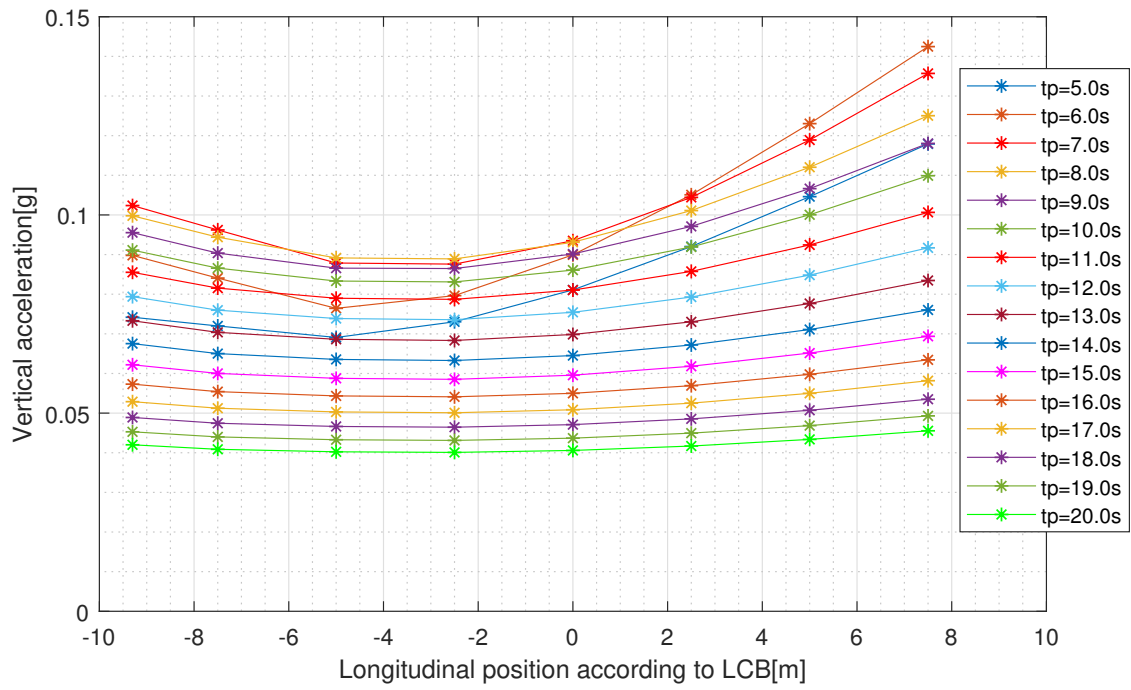


Figure A.6: Longitudinal position comparisons at different peak periods

Appendix B

Volumetric refinements - Full domain

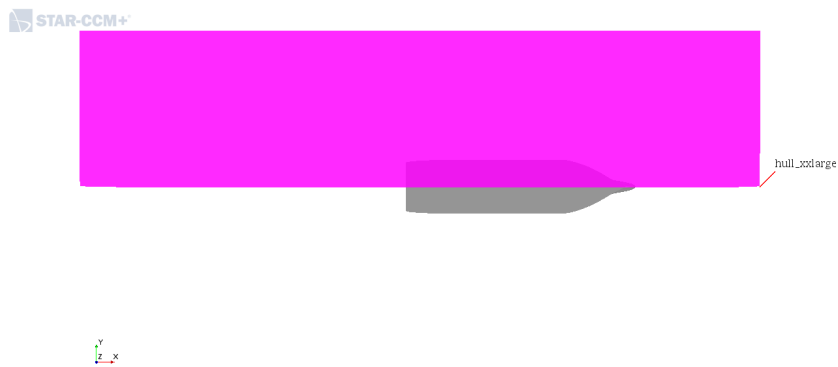


Figure B.1: Volumetric refinement - Hull XXL



Figure B.2: Volumetric refinement - Hull XL

STAR-CCM+



Figure B.3: Volumetric refinement - Hull L

STAR-CCM+



Figure B.4: Volumetric refinement - Hull M

STAR-CCM+



Figure B.5: Volumetric refinement - Hull S

STAR-CCM+



Figure B.6: Volumetric refinement - Hull XS

STAR-CCM+



Figure B.7: Volumetric refinement - Bow and Stern

Appendix C

Full domain results

The following figures are appendices related to the full domain simulation. Figure C.1 are a plot of the residuals for the full domain simulation with a base cell size of 1.25 m , and Figure C.3 are the resulting resistance curve for the same cell size.

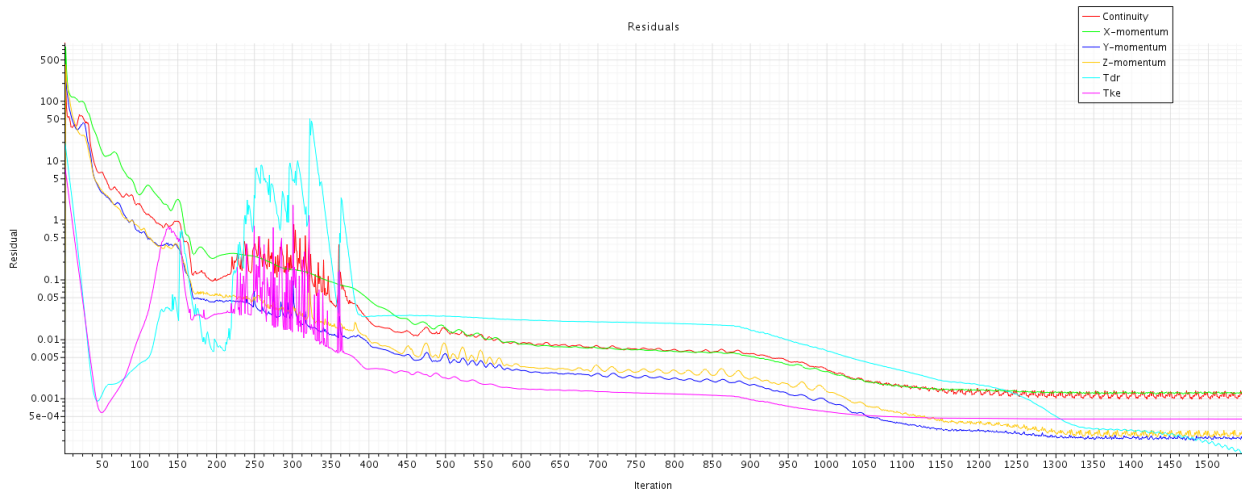


Figure C.1: Residuals, Base cell size: 1.25 m

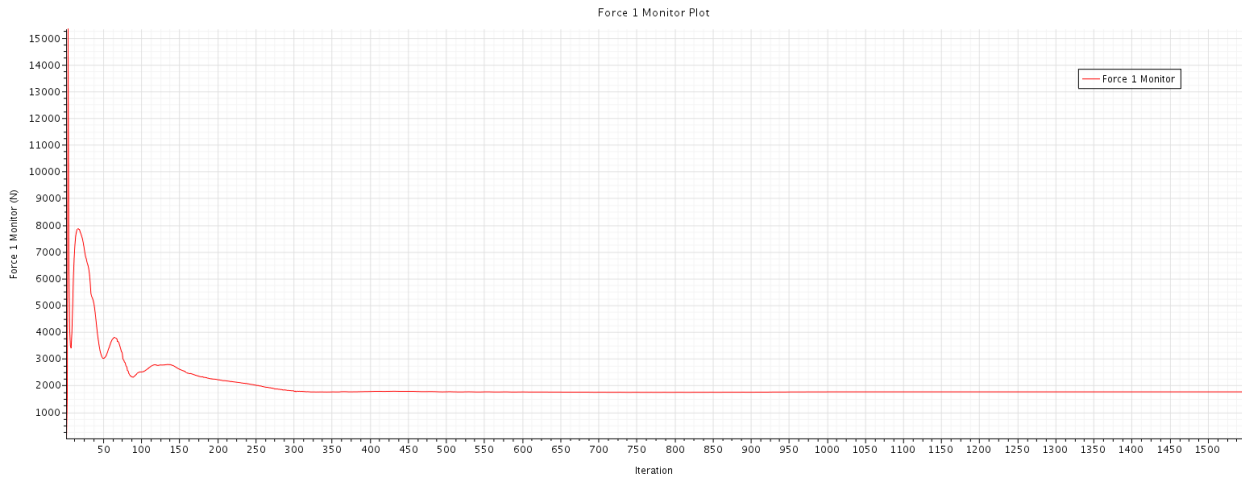


Figure C.2: Resistance, Base cell size: 1.25 m

The following plot shows the resulting boundary values for the dimensionless y^+ on the surface of the hull.

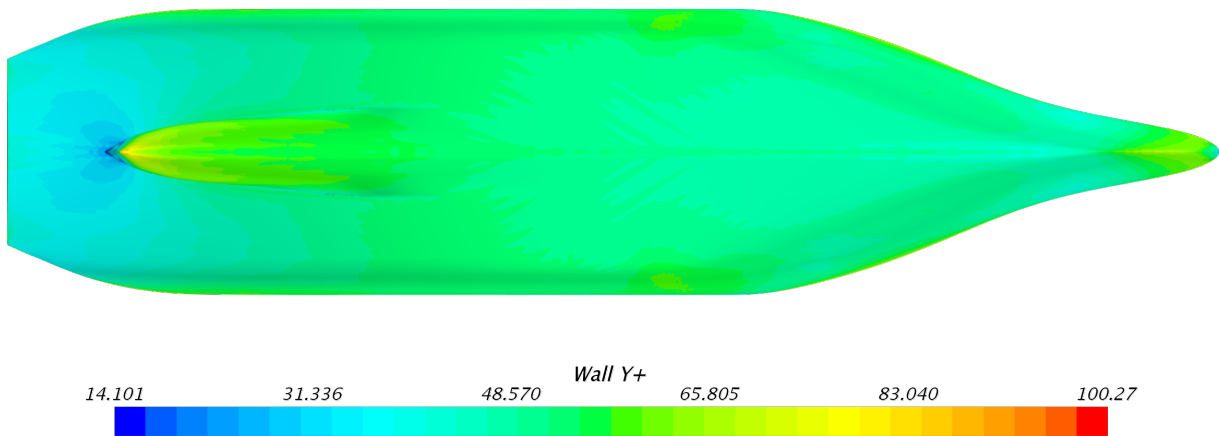


Figure C.3: y^+ values on hull surface

Appendix D

Volumetric refinements - Limited domain

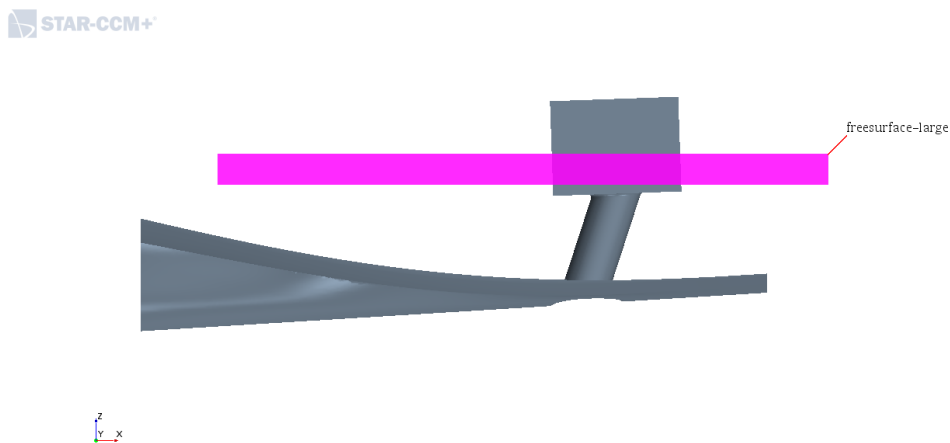


Figure D.1: Volumetric refinement - Free surface L

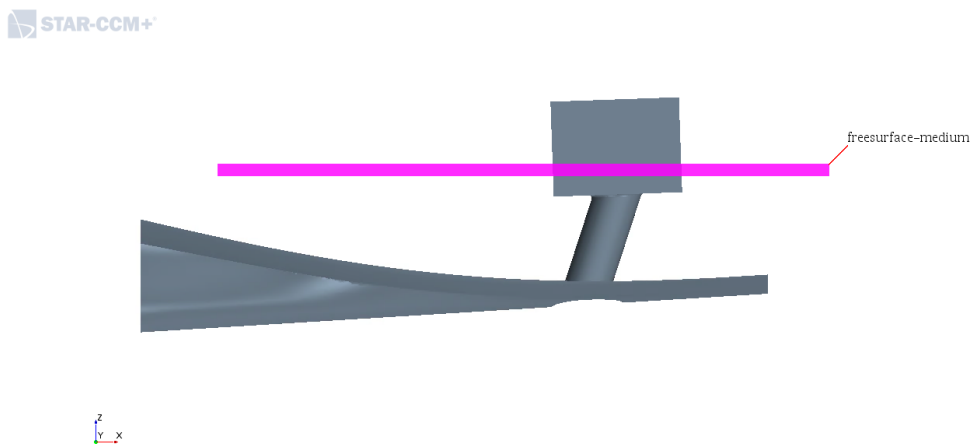


Figure D.2: Volumetric refinement - Free surface M

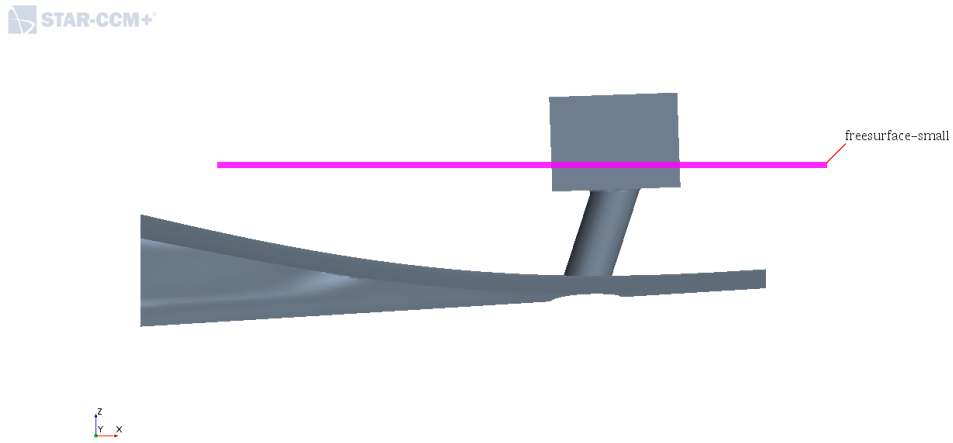


Figure D.3: Volumetric refinement - Free surface S

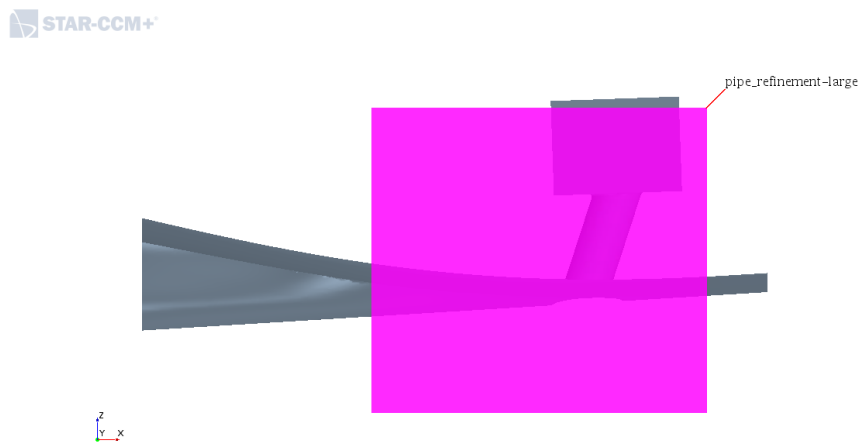


Figure D.4: Volumetric refinement - Free surface S

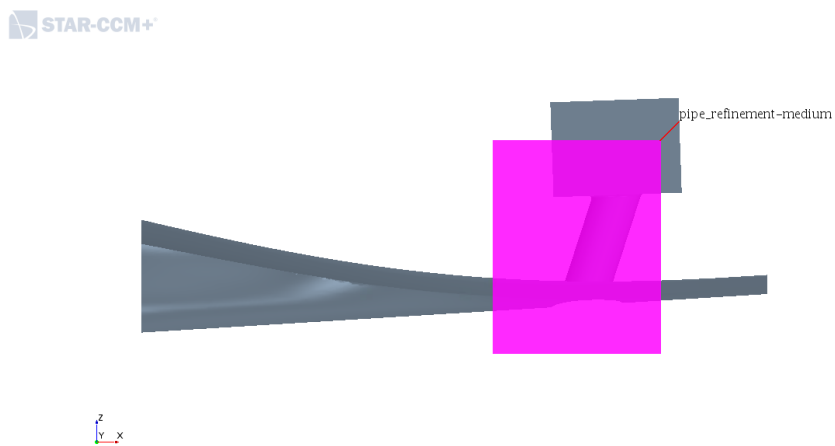


Figure D.5: Volumetric refinement - Pipe M

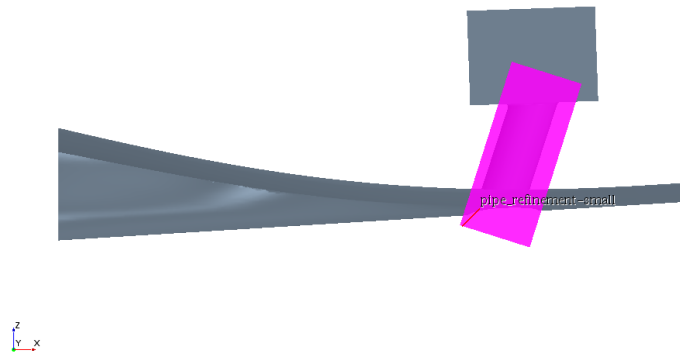


Figure D.6: Volumetric refinement - Pipe S

Appendix E

Limited domain results

Figure E.1, E.2, and E.3 illustrated the residuals for the final simulations of the three different shapes.

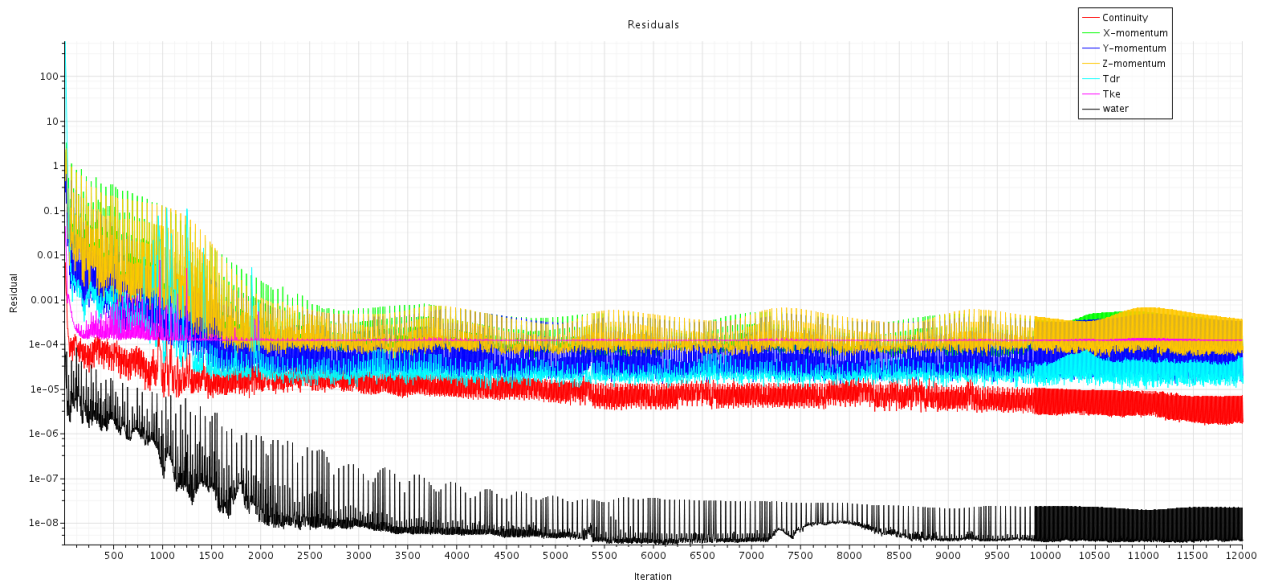


Figure E.1: Residuals for circular shape

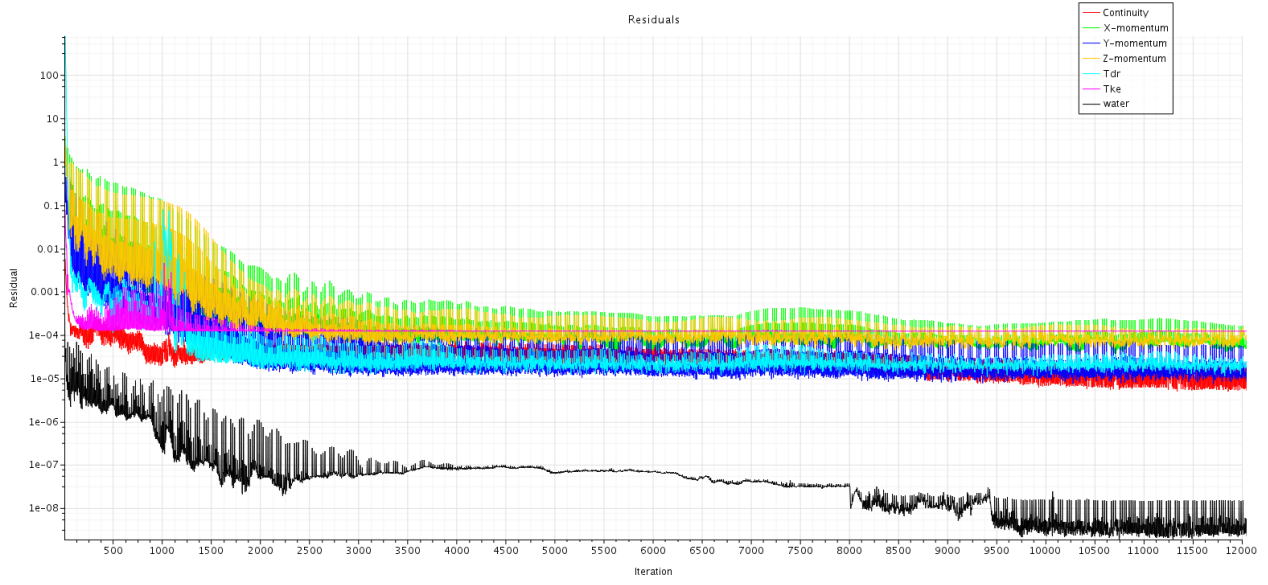


Figure E.2: Residuals for rectangular shape

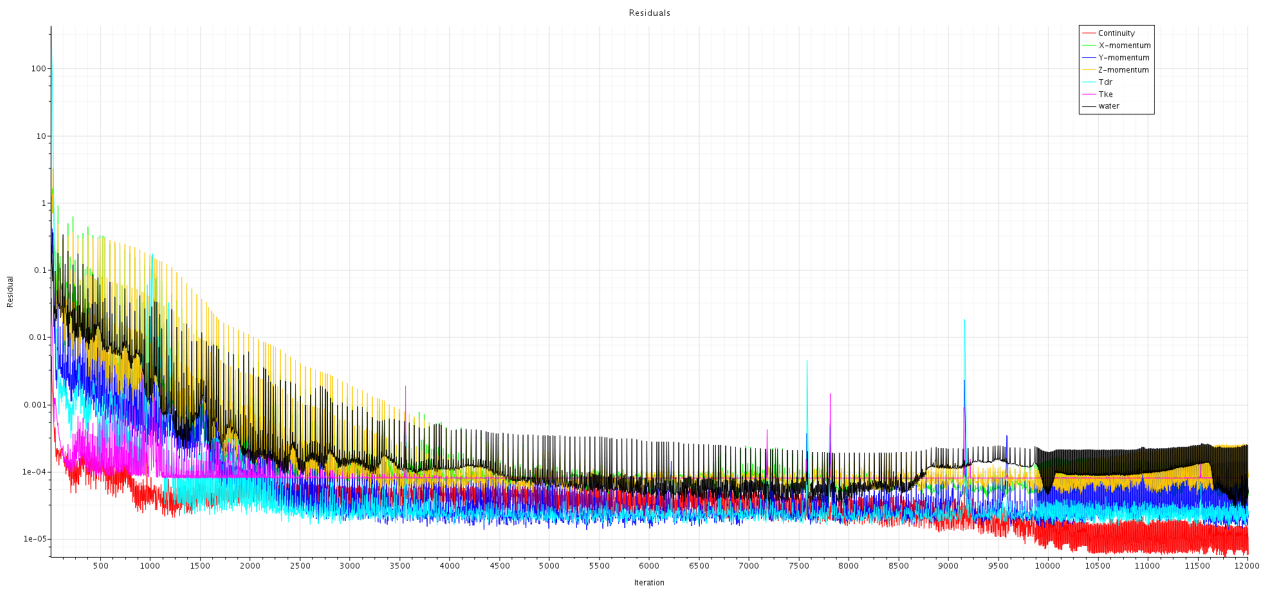


Figure E.3: Residuals for elliptical shape

Figure E.4 illustrates the resolved boundary layer for the limited domain for the circular moonpool. The at the bottom of the figure shows how the y_+ varies over the surface of the hull.

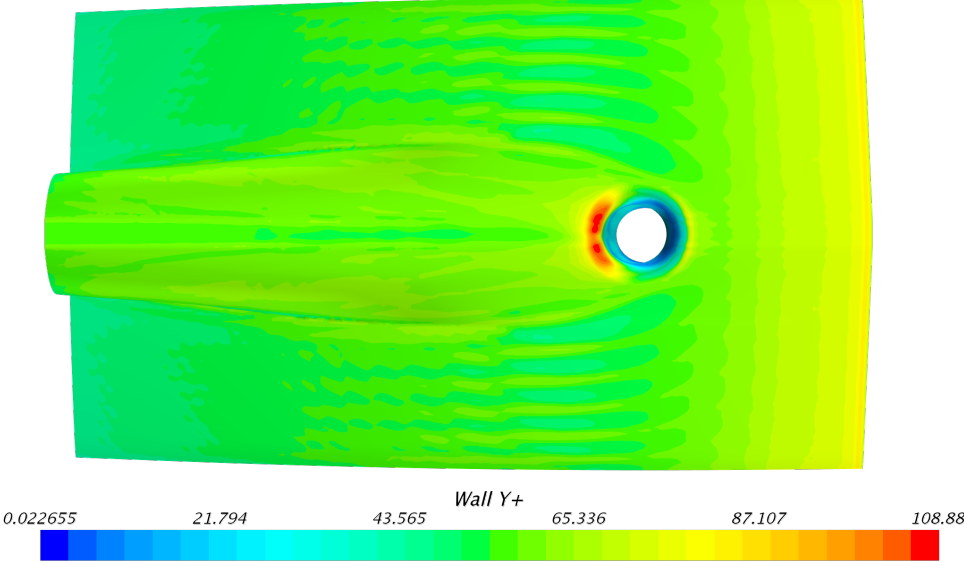


Figure E.4: y^+ boundary value for limited domain with circular moonpool

Appendix F

Passive scalar mass flux

The passive scalar mass flux was tracked with the use of a custom function, since this is not initially implemented in Star-CCM+. A user defined field function was created called "Passive_Scalar_Flow_Rate", with the following definition: $abs(\$PassiveScalarBoundaryFlux * mag(\$Area))$.

Two sum reports and monitors was then created to track the mass flux for the inlets and outlet. One report handled the mass flux into the through the inlet and bottom. The other sum report handled the passive scalar mass flux leaving the domain at the pressure outlet. These was called inlet and outlet, respectively.

A expression report and monitor was den created to calculate the percentage of "dirty" passive scalar leaving the domain, by taking the outlet value and dividing it with the inlet value. This was done with the following expression: $\$outletReport / \$inletReport * 100$.

Appendix G

Moonpool shape study - Passive scalar results

The following figures illustrates the passive scalar blend from time step 2.0 s to 42.0 s

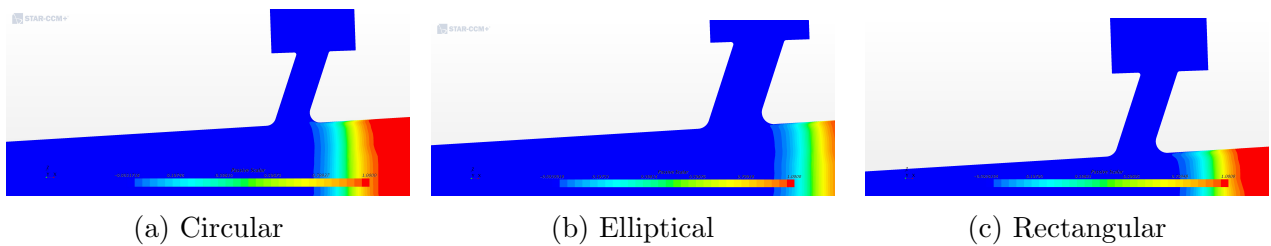


Figure G.1: Time step : 2.0 s

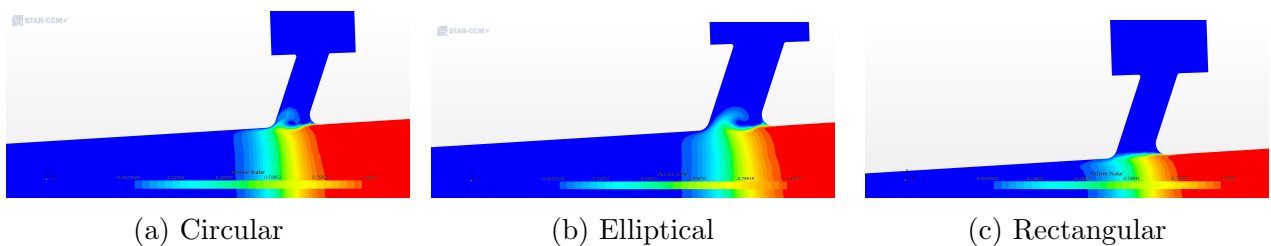


Figure G.2: Time step : 4.0 s

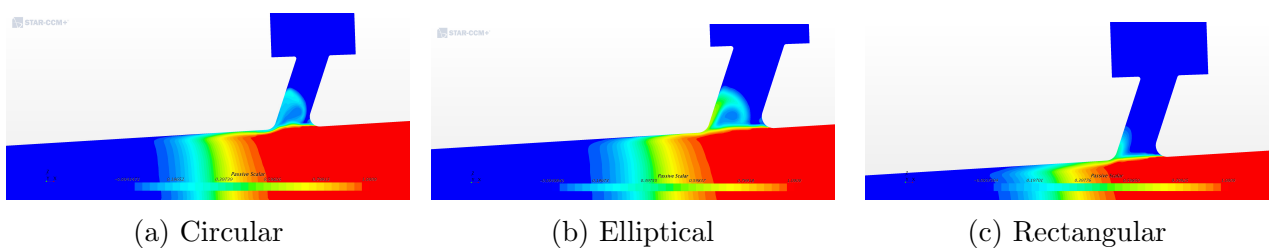
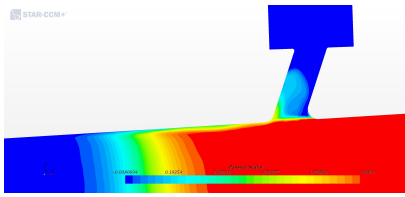
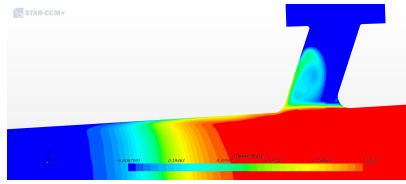


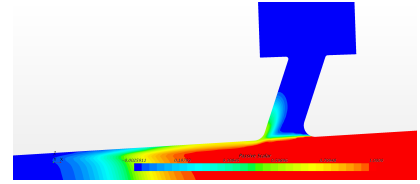
Figure G.3: Time step : 6.0 s



(a) Circular

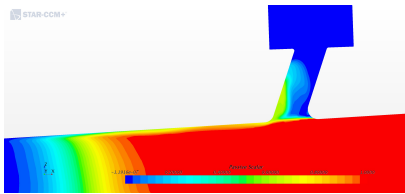


(b) Elliptical

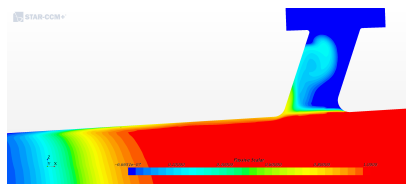


(c) Rectangular

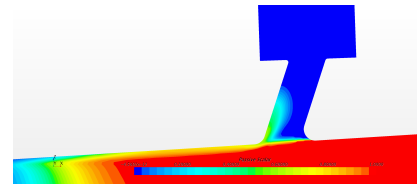
Figure G.4: Time step : 8.0 s



(a) Circular

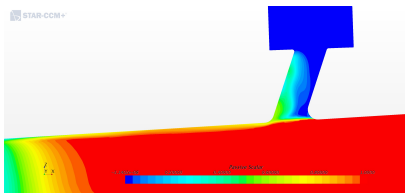


(b) Elliptical

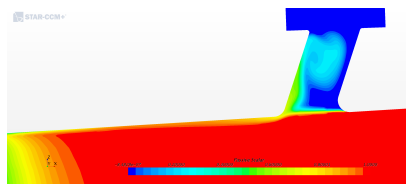


(c) Rectangular

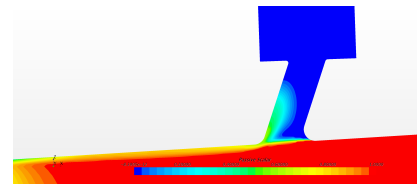
Figure G.5: Time step : 10.0 s



(a) Circular

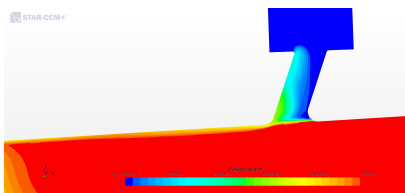


(b) Elliptical

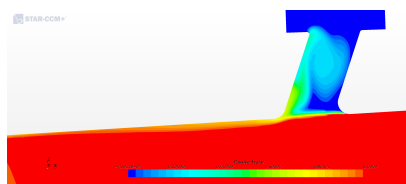


(c) Rectangular

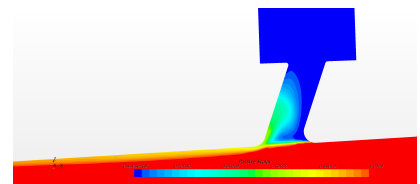
Figure G.6: Time step : 12.0 s



(a) Circular

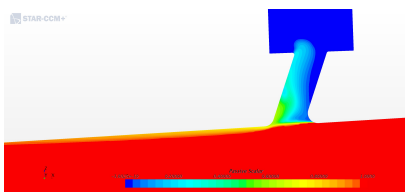


(b) Elliptical

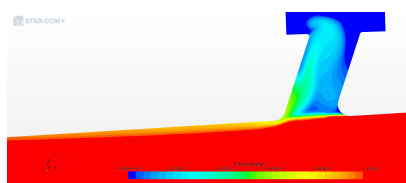


(c) Rectangular

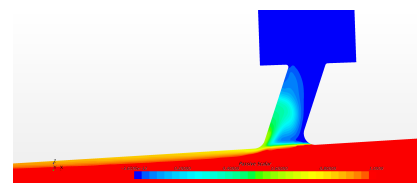
Figure G.7: Time step : 14.0 s



(a) Circular

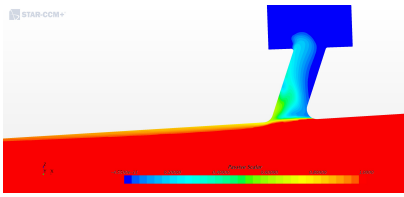


(b) Elliptical

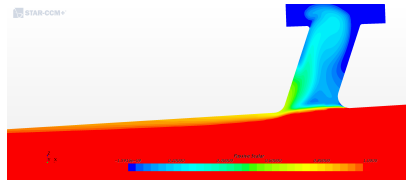


(c) Rectangular

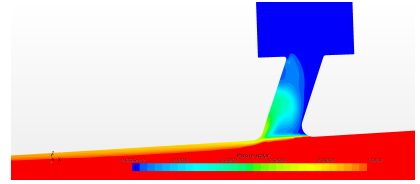
Figure G.8: Time step : 16.0 s



(a) Circular

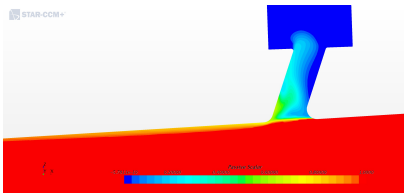


(b) Elliptical

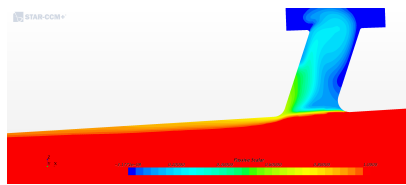


(c) Rectangular

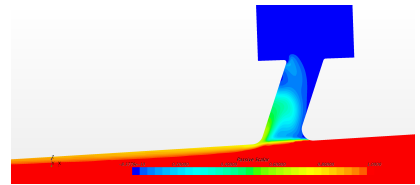
Figure G.9: Time step : 18.0 s



(a) Circular

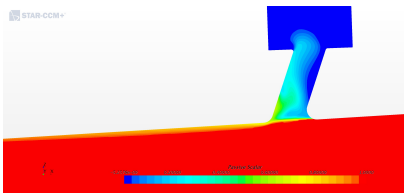


(b) Elliptical

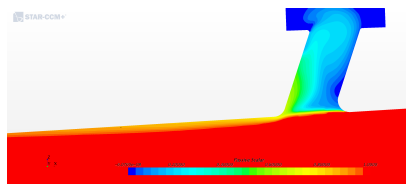


(c) Rectangular

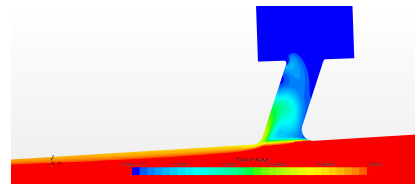
Figure G.10: Time step : 20.0 s



(a) Circular

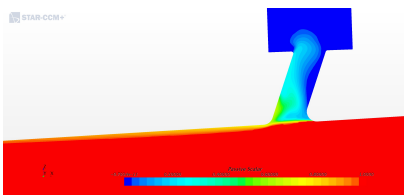


(b) Elliptical

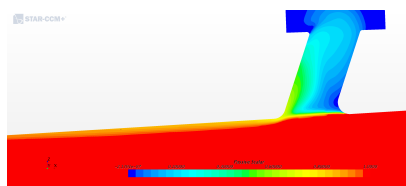


(c) Rectangular

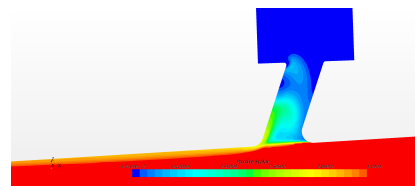
Figure G.11: Time step : 22.0 s



(a) Circular

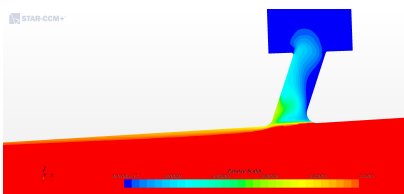


(b) Elliptical

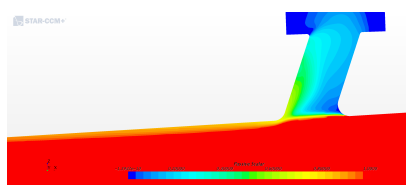


(c) Rectangular

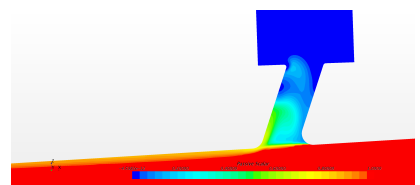
Figure G.12: Time step : 24.0 s



(a) Circular

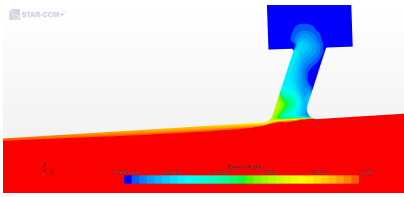


(b) Elliptical

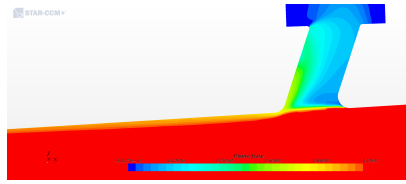


(c) Rectangular

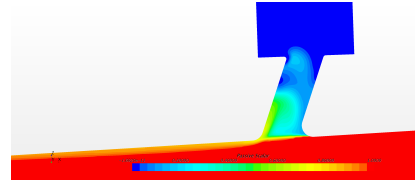
Figure G.13: Time step : 26.0 s



(a) Circular

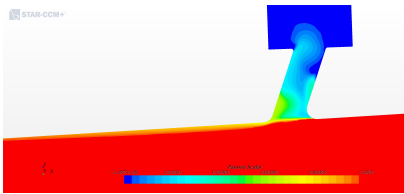


(b) Elliptical

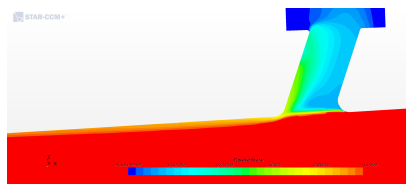


(c) Rectangular

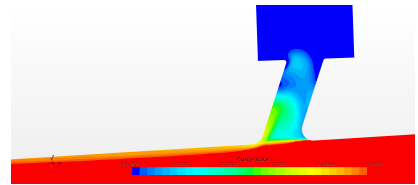
Figure G.14: Time step : 28.0 s



(a) Circular

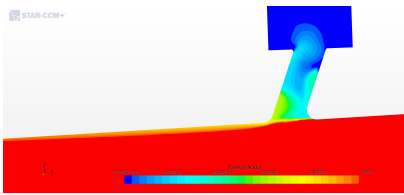


(b) Elliptical

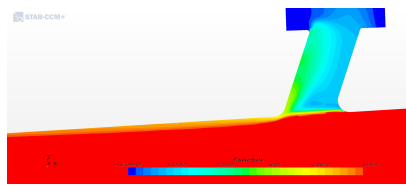


(c) Rectangular

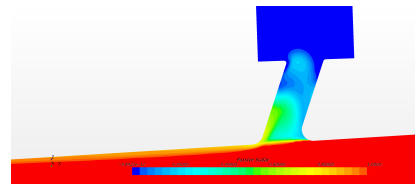
Figure G.15: Time step : 30.0 s



(a) Circular

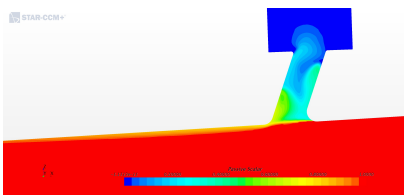


(b) Elliptical

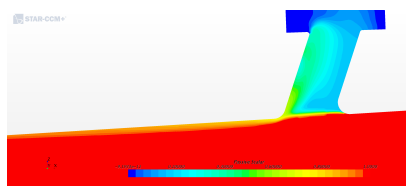


(c) Rectangular

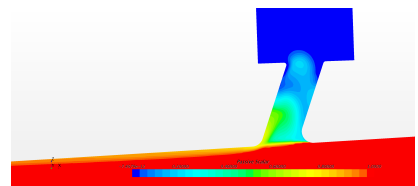
Figure G.16: Time step : 32.0 s



(a) Circular

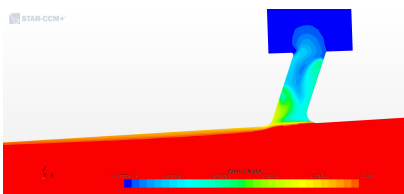


(b) Elliptical

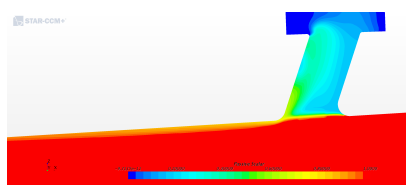


(c) Rectangular

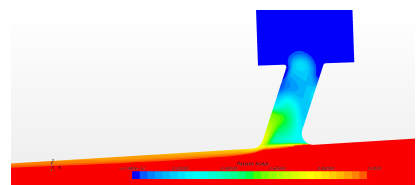
Figure G.17: Time step : 34.0 s



(a) Circular

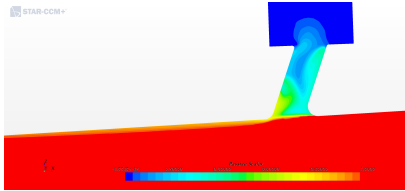


(b) Elliptical

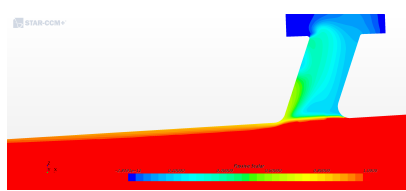


(c) Rectangular

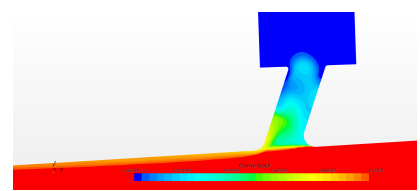
Figure G.18: Time step : 36.0 s



(a) Circular

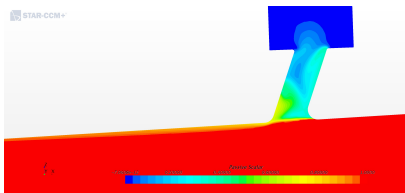


(b) Elliptical

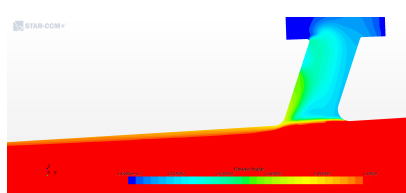


(c) Rectangular

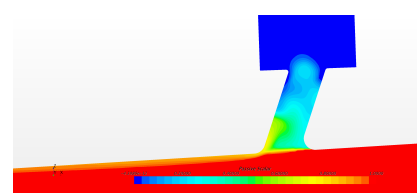
Figure G.19: Time step : 38.0 s



(a) Circular

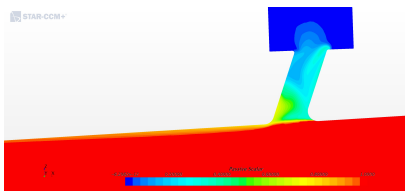


(b) Elliptical

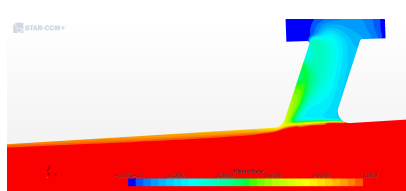


(c) Rectangular

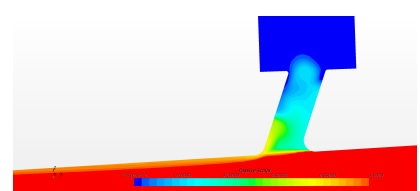
Figure G.20: Time step : 40.0 s



(a) Circular



(b) Elliptical



(c) Rectangular

Figure G.21: Time step : 42.0 s

Appendix H

Moonpool shape study - Velocity vector field results

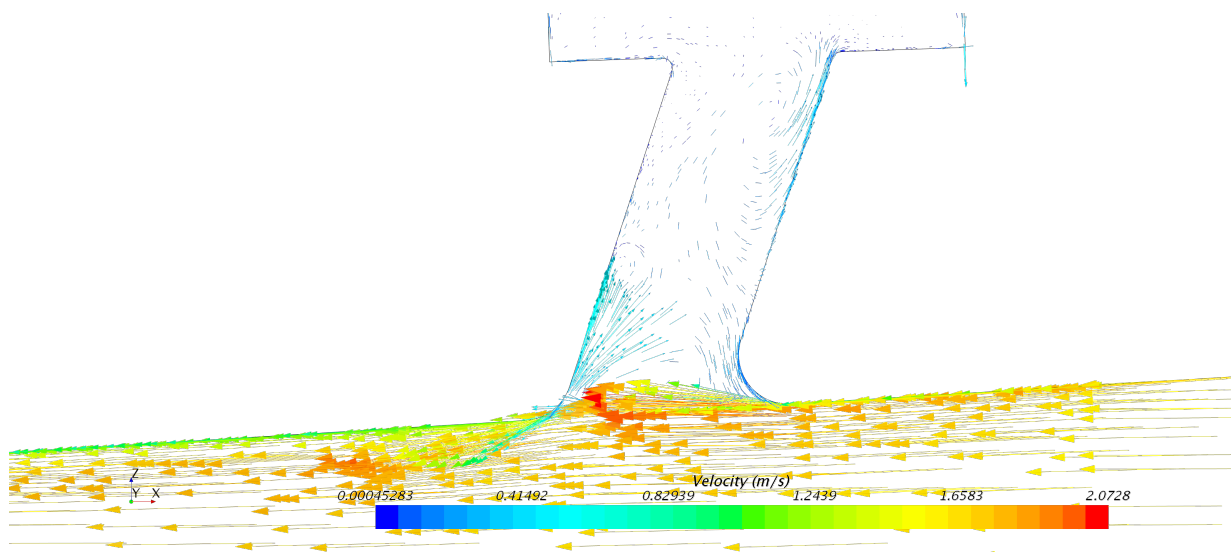


Figure H.1: Passive scalar field for circular shaped moonpool pipe, at time step 40.0 s

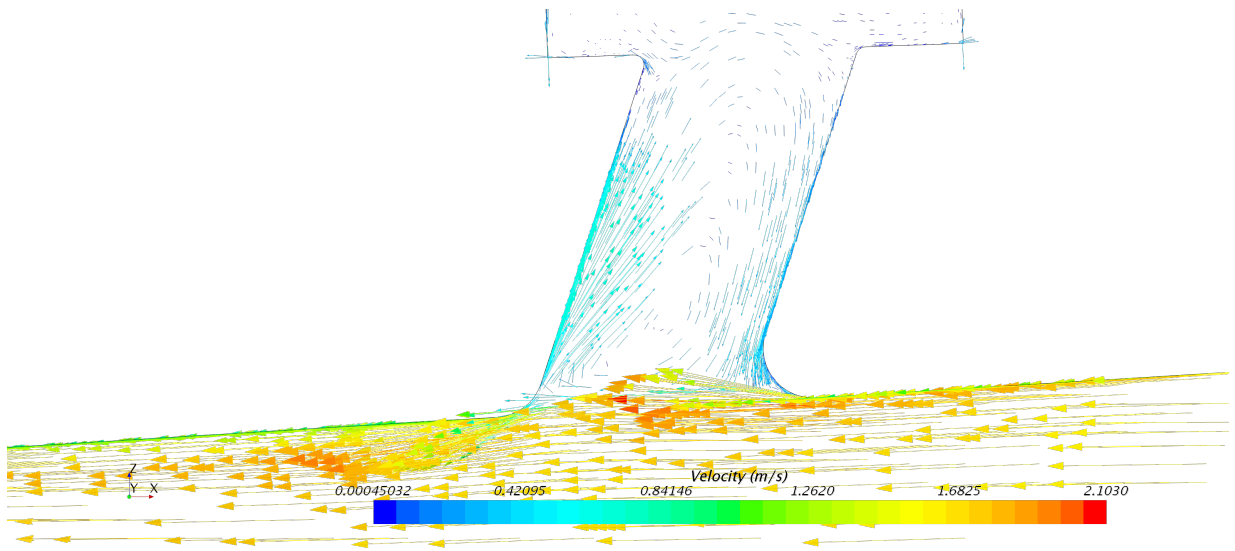


Figure H.2: Passive scalar field for elliptical shaped moonpool pipe, at time step 40.0 s)

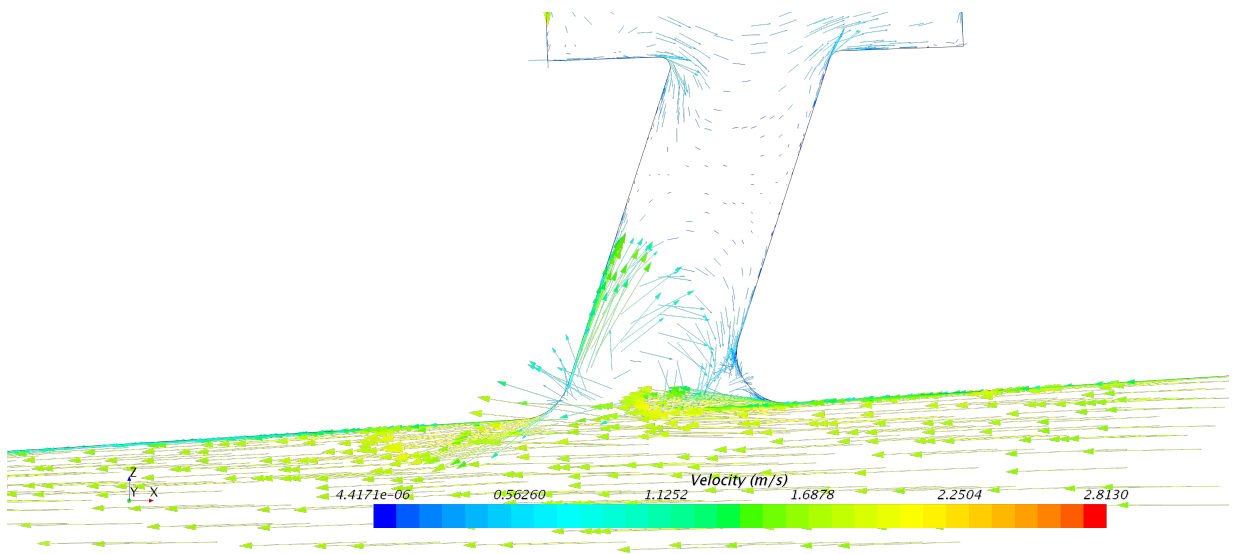


Figure H.3: Passive scalar field for rectangular shaped moonpool pipe, at time step 40.0 s

